

THE TENSILE FRACTURE OF MILD STEEL

Thesis by
Don Paul Clausing

In Partial Fulfillment of the Requirements
For the Degree of
Doctor of Philosophy

California Institute of Technology
Pasadena, California

1966

ACKNOWLEDGMENTS

Acknowledgment is made to the Pacific Scientific Company and the National Science Foundation for fellowships awarded to the author. Acknowledgment is also made of support received from funds contributed by the Kaiser Aluminum and Chemical Corporation.

Appreciation is expressed to Professor D. S. Wood of the California Institute of Technology for his guidance and many informative discussions. Appreciation is also expressed to Professor D. S. Clark of the California Institute of Technology for his guidance in performing many of the tasks that were necessary for the completion of this research and thesis.

ABSTRACT

The fibrous and cleavage tensile fracture of an annealed mild steel was investigated. Round tensile specimens of two geometries, one straight and one with a circumferential notch, were pulled at temperatures between room temperature and liquid nitrogen temperature. Tensile fractures occurred at average strains from 0.02 to 0.87. The mechanism of fibrous fracture at room temperature was investigated metallographically. The stress-strain values at which fibrous and cleavage fractures are initiated were determined.

Many fine microcracks, which are associated with pearlite colonies and inclusion stringers, develop prior to fibrous fracture. The macrofracture, which leads to final separation of the tensile specimen, is initiated by the propagation of a microcrack beyond the microstructural feature with which it is associated. Thus, the fibrous fracture of mild steel does not develop by the gradual growth and coalescence of voids that are large enough to be visible in the optical microscope. When the microcracks begin to open and propagate, final fracture quickly follows. Axial cracks are a prominent feature of the macrofracture that forms in the interior of the specimen immediately before final fracture.

The Bridgman distribution of stresses is not valid in a notched tensile specimen. Fibrous and cleavage fractures occur at approximately the same value of maximum tensile stress. When the maximum tensile stress that is necessary for cleavage fracture is plotted against the corresponding maximum tensile strain, the result is an unique locus.

TABLE OF CONTENTS

<u>Part</u>	<u>Title</u>	<u>Page</u>
	ACKNOWLEDGMENTS	
	ABSTRACT	
	TABLE OF CONTENTS	
	LIST OF FIGURES	
	LIST OF TABLES	
I.	INTRODUCTION	1
	A. <u>Subject of This Thesis</u>	2
	B. <u>Scope</u>	3
	1. Tensile Fracture Criteria	3
	(a) Fracture Parameters	4
	(b) Distribution of Stress and Strain Within Tensile Specimens	9
	2. Mechanisms of Tensile Fracture	17
	C. <u>Purpose</u>	18
	D. <u>Method of Attack</u>	19
	E. <u>Summary</u>	22
II.	EXPERIMENTATION	
	A. <u>Tensile Tests</u>	23
	1. Material Tested	23
	2. Equipment	23
	3. Experimental Procedures	28
	4. Experimental Results	32
	(a) Stress-Average Strain	32
	(b) Effect of Temperature on Flow Stress	32

<u>Part</u>	<u>Title</u>	<u>Page</u>
	(c) Effect of Strain upon Specimen Geometry	36
	(d) Fracture Data	37
B.	<u>Metallographic Studies</u>	37
1.	Displacements and Strains	37
(a)	Radial Displacement	37
(b)	Axial Strain	42
(c)	Plastic Region in Notched Specimen	44
2.	Mechanism of Fibrous Fractures	48
(a)	Microcracks	48
(b)	Macrofractures	53
III.	DISCUSSION	60
A.	<u>Deformation and Stress in Notched Tensile Specimen</u>	60
1.	Deformation	60
2.	Stresses	61
B.	<u>Mechanism of Fibrous Fracture at Room Temperature</u>	66
1.	Microcracks	66
2.	Macrofractures	74
C.	<u>Stresses and Strains at Fracture</u>	94
1.	Cleavage Fracture	99
2.	Fibrous Fracture	106
IV.	CONCLUSIONS	109
	APPENDIX I.	112

<u>Part</u>	<u>Title</u>	<u>Page</u>
	APPENDIX II.	116
	APPENDIX III.	123
	REFERENCES	129

LIST OF FIGURES

<u>Number</u>	<u>Title</u>	<u>Page</u>
1	Tensile Fracture Locus of the Form Proposed by Ludwik.	6
2	Neck Geometry.	11
3	Axial Stress Distribution on Minimum Cross Section of Necked Tensile Specimen. After Bridgman. $a/R = 0.4$.	13
4	Bridgman Correction.	14
5	Tensile Specimens.	20
6	Tensile Test Apparatus.	24
7	Stiffness of Tensile Test System.	26
8	Cold Bath Container.	27
9	Stiff Loading Device.	29
10	Strain vs. Elongation in Tensile Specimens.	31
11	Room Temperature Stress-Strain Curves.	33
12	Three Groups of Room Temperature Stress-Strain Curves for Unnotched Specimens.	34
13	The Effect of Strain upon the Temperature Dependence of Flow Stress.	35
14	Section Radius Divided by Profile Radius vs. Strain.	38
15	Deformation of Banding in Notched Specimen.	39
16	Radial Displacement vs. Initial (Unstrained) Radius for a Notched Specimen.	43
17	Grain Boundary Angle vs. Average Strain.	45
18	Plastic Zone in Notched Specimen.	47
19	Top, Careful Polish; Bottom, Normal Polish.	49
20	Holes Caused by the Enlargement of Microcracks and/or the Removal of Particles Bounded by Microcracks.	50

<u>Number</u>	<u>Title</u>	<u>Page</u>
21	Total Microcrack Length/Unit Area vs. Average Strain for Four Unnotched Specimens and One Notched Specimen.	54
22	Macrocrack in Notched Specimen.	55
23	Fine Cracks in Macrofracture of Notched Specimen.	56
24	Procedure for Filling Macrocrack with Epoxy Resin.	57
25	Theoretical Axial Strain Distribution.	62
26	Average Stress vs. Average Strain for Notched Specimen at Room Temperature	64
27	Comparison of Theoretical Stress Distributions for Two Radial Displacement Functions. Average Strain: 0.55.	65
28	Intrapearlitic Microcracks.	67
29	Interpearlitic Microcrack.	69
30	"Ox-Tail" Microcrack.	70
31	Complex Microcrack in Unnotched Specimen Containing Macrocrack.	71
32	Macrofracture Filled with Resin in Unnotched Specimen, Surface 0.022 In. from Axis.	75
33	Macrofracture Filled with Resin in Unnotched Specimen, Surface 0.014 In. from Axis.	76
34	Macrofracture Filled with Resin in Unnotched Specimen, Surface 0.012 In. from Axis.	77
35	Macrofracture Filled with Resin in Unnotched Specimen, Surface 0.008 In. from Axis.	78
36	Macrofracture Filled with Resin in Unnotched Specimen, Surface 0.005 In. from Axis.	79
37	Macrofracture Filled with Resin in Unnotched Specimen, Surface 0.003 In. from Axis.	80

<u>Number</u>	<u>Title</u>	<u>Page</u>
38	Macrofracture Filled with Resin in Unnotched Specimen, Surface on Axis.	81
39	Macrofracture Filled with Resin in Unnotched Specimen, Surface 0.003 In. Beyond Axis.	82
40	Macrofracture Filled with Resin in Unnotched Specimen, Surface 0.005 In. Beyond Axis.	83
41	Macrofracture Filled with Resin in Unnotched Specimen, Surface 0.007 In. Beyond Axis.	84
42	Macrofracture Filled with Resin in Unnotched Specimen, Surface on Axis (Surface Mechanically Polished After Figure 38).	85
43	Macrofracture Filled with Resin in Unnotched Specimen, Surface 0.003 In. Beyond Axis (Same Surface as Figure 39).	86
44	Macrofracture Filled with Resin in Unnotched Specimen, Surface 0.005 In. Beyond Axis (Same Surface as Figure 40).	87
45	Macrofracture Filled with Resin in Unnotched Specimen, Surface 0.007 In. Beyond Axis (Same Surface as Figure 41).	88
46	Macrofracture Filled with Resin in Unnotched Specimen, Axial Macrocrack Lying in Grain Boundary.	90
47	Fine Cracks in Macrofracture of Notched Specimen (Same as Figure 23).	91
48	Macrofracture in Notched Specimen.	92
49	Intermittent Macrofracture, Macrofracture Filled with Resin in Unnotched Specimen.	95
50	Microcrack Starting to Spread, Unnotched Specimen Containing Macrocrack.	96
51	Possible Mechanism of Macrofracture Initiation.	97
52	Stress and Strain at Fracture.	98
53	Two Types of Paths for Approaching the Stress-Strain Value at Which Cleavage Fracture Occurs.	101

<u>Number</u>	<u>Title</u>	<u>Page</u>
54	Hypothetical Stress-Strain Loci for Cleavage Fracture.	102
55	Three of the Nonisothermal Stress-Strain Paths that Resulted in Cleavage Fracture.	104
56	Grain Boundary Coordinates.	112

LIST OF TABLES

<u>Table</u>	<u>Title</u>	<u>Page</u>
I.	Average Strain at Fracture for Unnotched Specimens at Room Temperature	36
II.	Flow and Fracture Data for Unnotched Specimens Fractured in Tensile Testing Machine	40
III.	Fracture Data for Notched Specimens Fractured in Tensile Testing Machine	41
IV.	Ratio of Generalized Strain Increment to Increment of Maximum Principal Strain	125

I. INTRODUCTION

Although mild steel is the most commonly used engineering material, the conditions which cause it to fracture and the mechanism by which the fracture develops are not well understood. The properties usually measured in the ordinary tensile test of mild steel at room temperature -- upper yield stress, lower yield stress, and ultimate tensile strength -- are properties whose values are completely determined by plastic flow, not fracture. Of the mechanical properties commonly reported, only reduction of area is pertinent to fracture. The reliance upon reduction of area as the engineering criterion for fracture reflects the lesson of early experience that if the ductility is sufficient, as represented by large reduction of area, fracture will not be a problem in engineering practice.

However, it is now recognized that adequate ductility in the ordinary tensile test does not guarantee freedom from fracture in engineering service. Many catastrophic fractures have occurred in ships, bridges, pressure vessels, and pipe lines (1)*, even though the reduction of area in tensile tests met specifications. These failures vividly demonstrated the inadequacy of the previously held concept that the reduction of area was a sufficient parameter for the consideration of fracture. Also, fracture at high strains is a significant problem in fabrication processes. Therefore, there has been increased interest in the causes and mechanisms of fracture (2, 3, 4, 5, 6, 7).

* Figures appearing in parentheses refer to references listed at the end of this thesis.

A. Subject of This Thesis

This thesis is concerned with the tensile fracture of mild steel. More specifically, it presents information about the fracture of mild steel during one application of tensile load at temperatures between room temperature and liquid nitrogen temperature.

In this thesis, all tensile fractures are divided into the following three types:

1. final fracture,
2. macrofracture (macrocrack),
3. microfracture (microcrack).

Final fracture is the final parting of the tensile specimen to form two completely separate pieces. Macrofracture is the parting of the tensile specimen over a region which is large compared to the dimensions of the microstructure, but which does not yet cover the entire cross section. Microfracture is parting of the steel over a region comparable in size to typical microstructural features in the steel. Thus, it is very possible that microfractures may be associated with some particular microstructural features in the steel. There may be many microfractures in one tensile specimen.

Final fracture may be further classified into groups based upon the appearance of the fracture surface (8). These two groups are:

1. cleavage,
2. fibrous.

Cleavage fracture is characterized by the bright, shiny, crystalline appearance of the fracture surface. Under a microscope each grain

in the steel appears to have separated along a plane, and the fracture planes for different grains appear to be randomly oriented with respect to the specimen axis. Fibrous fracture is characterized by the rough, dull, grey appearance of the fracture surface. Under the microscope the surface appears badly torn, stringy, and almost foamy. It is possible for both cleavage and fibrous fracture surfaces to occur on the same tensile specimen.

A second method of classifying final fracture, which is commonly employed, is to describe it as being ductile or brittle. Unfortunately, these words are used with various meanings. Therefore, the terms ductile and brittle will not be used in this thesis to describe fractures.

B. Scope

Satisfactory understanding of the tensile fracture of mild steel requires the following two types of knowledge:

1. tensile fracture criteria which quantitatively state the conditions that will cause tensile fracture of mild steel to occur,
2. the mechanism by which the tensile fracture of mild steel develops.

1. Tensile Fracture Criteria

Proper specification of tensile fracture conditions requires knowledge of the values of the pertinent parameters, such as stress, strain, and temperature, at which the tensile fracture of mild steel occurs. A statement of all the combinations of the values of the pertinent parameters at which tensile fracture occurs is a tensile frac-

ture criterion. The type of fracture for which the tensile fracture criterion is stated in practice is the initiation of macrofracture, because the initiation of macrofracture is the critical event leading to final fracture.

(a) Fracture Parameters. For a given material, the occurrence of tensile fracture must be governed by a number of parameters that describe the loading and environment. It is assumed here that environment can be described by the temperature. The loading is described by the maximum tensile stress, hydrostatic tension, ratio between two principal stresses, maximum tensile strain, and ratio between two principal strains, all measured at the point in the specimen at which macrofracture is initiated. One can imagine many other parameters necessary for the complete description of environment and loading, but it is assumed here that these are all held constant. Also, it is assumed that history effects are not important. Therefore, the view adopted in this thesis is that environment and loading are described by the instantaneous values of the six parameters listed above.

If the values of the six parameters above at the initiation of macrofracturing were plotted in a six-dimensional coordinate system, the resulting surface would completely define the tensile fracture criterion. Unfortunately, it would be very difficult to conduct the necessary experiments and plot the resulting six-dimensional figure. Therefore, in practice one hopes that only two of the six parameters will prove to be significant.

Ludwik (9) proposed in 1923 that an unique tensile fracture

locus (tensile fracture criterion) would be obtained if the values that were measured at fracture were plotted in the two-dimensional coordinate system defined by maximum tensile stress and strain, as shown in Figure 1. Maximum tensile stress and strain means the maximum of the principal stresses and strains at the point at which macrofracture is initiated. The stress or strain may be greater at some other position within the specimen. The forms of the tensile fracture locus and the stress and strain distributions within the specimen may be such that the point in the specimen that reaches the fracture locus first will have less stress or strain than some other points in the specimen.

In this thesis, the view is adopted that plotting the values of maximum tensile stress and strain at fracture is simple and informative. Therefore, tensile fracture data will be presented in this form.

The determination of the maximum tensile stress-strain locus for the tensile fracture of mild steel requires that different paths such as 1, 2, and 3 in Figure 1 be traversed. If only unnotched tensile specimens are pulled at room temperature, then Path 1 will always be traversed, and only one data point, such as Point a, can be obtained. The most common experimental methods of traversing different stress-strain paths in mild steel, such as Paths 2 and 3 in Figure 1, are to increase the hydrostatic tension by the use of notched specimens, and to lower the temperature. (In mild steel, lowering the temperature and raising the strain rate have the same effect over a wide range of values. For brevity in this thesis, this effect will be referred to in terms of temperature only.) A larger maximum tensile

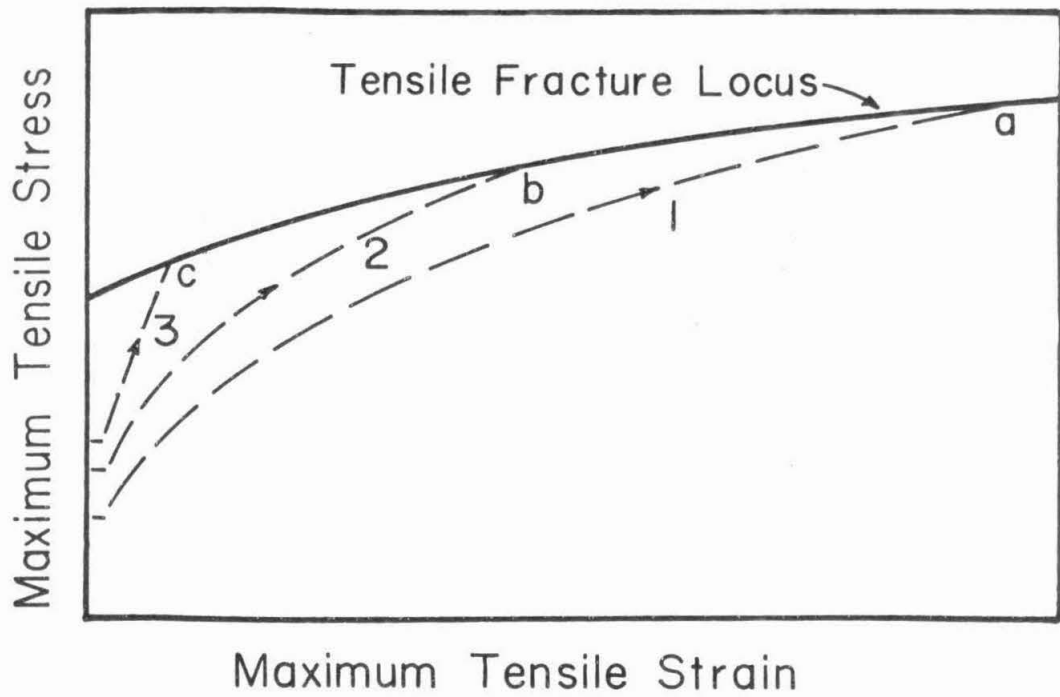


Figure 1. Tensile Fracture Locus of the Form Proposed by Ludwik.

stress at a given strain occurs in mild steel with both increased hydrostatic tension and lower temperature. Therefore, different temperatures and different amounts of hydrostatic tension cause different stress-strain paths, such as 1, 2, and 3 in Figure 1, to be traversed.

One must realize the different roles played in Ludwik's hypothesis by the maximum tensile stress and strain on the one hand, and hydrostatic tension, temperature, and other parameters on the other hand. Parameters such as hydrostatic tension and temperature serve a secondary role. They determine the different stress-strain paths, such as 1, 2, and 3 in Figure 1, by which the fracture curve may be reached. Of course, Ludwik may have been wrong, and the values of maximum tensile stress and strain at fracture will not lie on an unique locus. A third parameter, such as hydrostatic tension (or temperature), may have to be added to maximum tensile stress and strain to form a three-dimensional coordinate system before an unique fracture locus can be obtained. In this case, hydrostatic tension (or temperature) would be a fundamental fracture parameter on a par with maximum tensile stress and strain. If Ludwik's hypothesis is correct, the tensile fracture criterion can be completely expressed in terms of maximum tensile stress and strain, without mentioning hydrostatic tension or temperature. There is an important distinction between the role of a fundamental tensile fracture parameter that must be included in the tensile fracture criterion, and the role of a secondary tensile fracture parameter that does not have to be included in a statement of the tensile fracture criterion. Unfortunately, discussions in the literature are often confusing on this

point.

In the forty-three years since Ludwik advanced his hypothesis, much work has been done in an attempt to find the unique tensile fracture stress-strain locus, or to prove that such an unique locus does not exist when maximum tensile stress and strain are used as the only coordinates. Most of the past work suffered from two critical difficulties:

1. the stress and strain distribution within necked and notched tensile specimens was not known;
2. the location of tensile fracture initiation was not known with certainty.

Most investigators assumed that fracture was initiated on the specimen axis. This will be discussed further in Section I. B. 2.

When maximum tensile stress and strain are used as the coordinates, one must be able to determine the maximum tensile stress and strain at the point at which fracture is initiated. In a round tensile specimen, the maximum tensile stress and strain are in the axial direction, and occur on the minimum cross section. However, in most investigations, the variation of stress and strain with radial position has not been known. Faced with this difficulty, most investigators have simply used the average axial stress and the average axial strain, defined as follows:

$$\text{Average Stress: } \sigma = F/A \quad [1]$$

$$\text{Average Strain: } \epsilon = \ln(A_0/A) \quad [2]$$

where F is the axial force, A_0 is the initial minimum cross-sectional area of the specimen, and A is the instantaneous minimum cross-

sectional area during pulling.

These investigators then made qualitative arguments about the nature of the stress and strain distribution within the tensile specimen. Based upon these qualitative arguments, conclusions were stated concerning the nature of the tensile fracture stress-strain locus. The author finds this procedure unsatisfactory. Some of the critical qualitative arguments concerning the nature of the stress and strain distribution within necked and notched tensile specimens have utilized dubious assumptions. The author believes that for experimentally determined tensile fracture stress-strain values to be meaningful, they should be calculated by some rational procedure. The author completely agrees with Lubahn (10), who, in a review article on notch tensile testing, stated:

"The most needed information regarding the notch tensile test is also that which is most difficult to obtain, namely the distribution of the principal stresses and principal strains over the notched section."

(b) Distribution of Stress and Strain Within Tensile Specimens.

The primary qualitative effect of a natural neck or a machined notch upon the stress distribution across the minimum cross section of a round tensile specimen has long been well understood. As straining proceeds, the minimum cross section contracts more rapidly than the larger cross sections above and below it. This creates a radial tension on the minimum cross section. This tension must be zero on the surface, and increases within the interior of the specimen.

Several attempts (11, 12, 13) have been made to analyze the stress distribution on the minimum cross section of a necked tensile

specimen. The analysis made by Bridgman is the most accepted one, and in the author's opinion, is the best analysis. Bridgman's analysis is an approximate solution for the stresses on the minimum cross section of a necked round tensile specimen.

Symmetry imposes the condition that on the minimum cross section the three principal stresses are the axial, radial, and circumferential stresses, which depend only on the radius. Bridgman attacked the problem of determining the stress distribution in the following way. (1) He assumed that the radial displacement on the minimum cross section is a linear function of radius; i. e., that the strains are uniform over the cross section. (2) He satisfied the von Mises yield criterion, and the Lévy-Mises plastic flow rules exactly to obtain the deviatoric components of the axial, radial, and circumferential stresses on the minimum cross section. (3) He determined the hydrostatic tension on the minimum cross section as a function of radius by approximately satisfying the radial equilibrium equation.

The approximation made in order to satisfy the radial equilibrium equation is shown in Figure 2. Bridgman said that a line of principal stress, such as X-X in Figure 2, must be perpendicular to the specimen axis and the specimen surface. He then assumed that the principal stress line is simply an arc of a circle. With the principal stress direction thus specified, the radial equilibrium equation can be solved to determine the hydrostatic tension as a function of radius.

Adding the hydrostatic tension to the previously obtained deviatoric stresses gives the total axial, radial, and circumferential

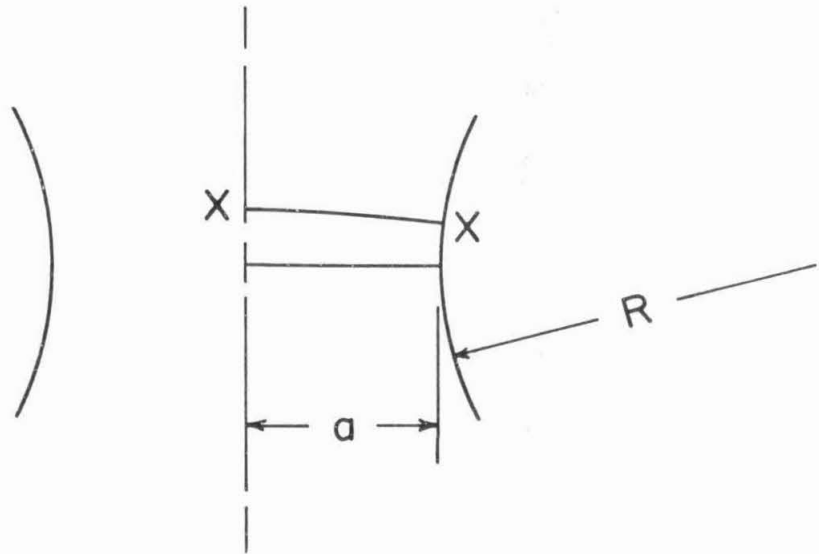


Figure 2. Neck Geometry.

stresses on the minimum cross section. The axial stress as a function of radius is shown in Figure 3. The stress on the surface is the flow stress for the material. If there were no neck, the axial stress would be equal to the flow stress everywhere on the minimum cross section. However, the presence of the neck causes the hydrostatic tension to increase toward the center of the specimen, thus increasing the maximum tensile stress above the flow stress. The curve in Figure 3 shows that the flow stress is less than the average stress, and the maximum tensile stress, at the specimen axis, is greater than the average stress.

The stress distribution depends upon the curvature of the principal stress line X-X in Figure 2. This curvature is completely determined by the ratio of the specimen radius, a , to the profile radius, R . Thus, the stress distribution depends on a/R . The ratio of maximum axial stress to average stress, and the ratio of flow stress to average stress, are shown in Figure 4 as a function of a/R .

Bridgman made experiments to check his assumption that the strain is uniform in a necked tensile specimen. He constructed round tensile specimens by brazing together concentric cylinders. The braze joint then served as a marker. By pulling until a neck was developed, and then sectioning, Bridgman determined that the radial displacement was in fact a linear function of radius, as assumed in Step 1. Bridgman did not experimentally check his assumption that the principal stress line is an arc of a circle. The author believes that it is very difficult, if not impossible, to check this experimentally.

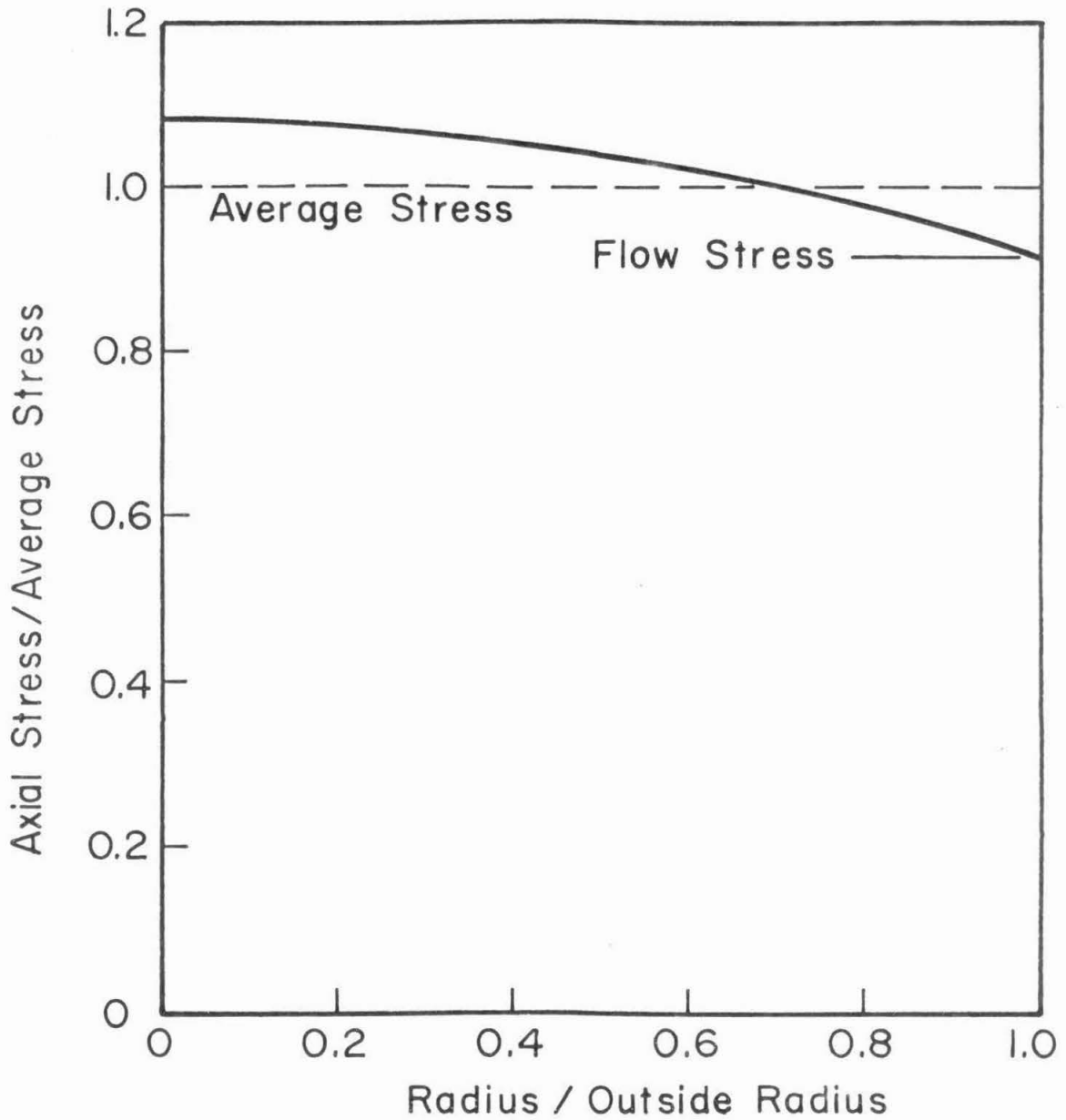


Figure 3. Axial Stress Distribution on Minimum Cross Section of Necked Tensile Specimen. After Bridgman. $a/R = 0.4$.

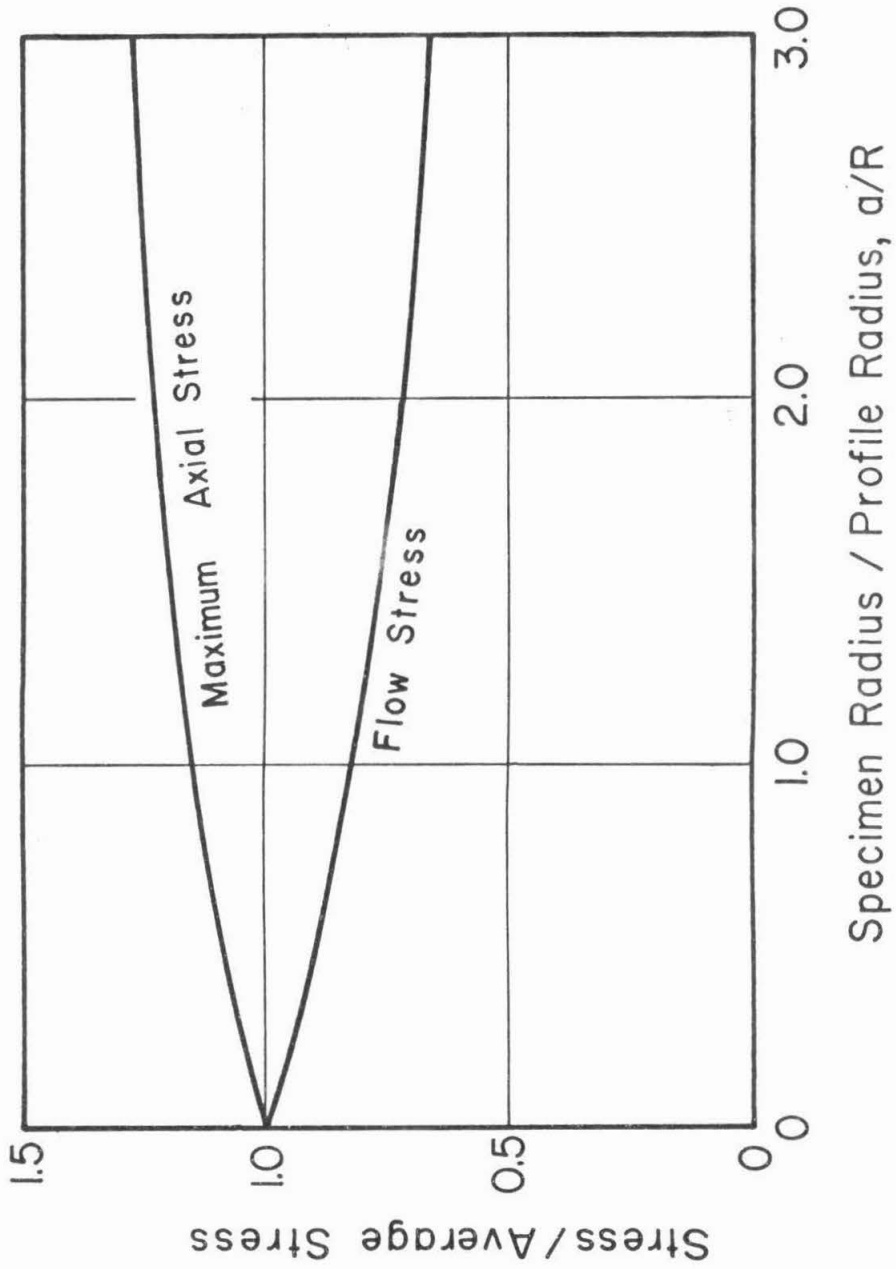


Figure 4. Bridgman Correction.

Parker, Davis, and Flanagan (8) attempted to determine the stress distribution in a round tensile specimen by using the Sachs boring-out technique. However, for valid results to be obtained with the Sachs boring-out technique, the stress distribution must be independent of axial position. This is far from the case in a necked tensile specimen. Therefore, the author does not believe that this procedure gave valid results.

Trozera (14) has shown that Bridgman's solution does give the correct ratio between average stress and flow stress for a necked tensile specimen. Trozera ran tensile and compressive tests on aluminum. He found that the flow stress in necked tensile specimens, as calculated by Bridgman's analysis, was exactly equal to the flow stress determined in compression, where, of course, no necking occurred.

Marshall and Shaw (15) verified by a different method that Bridgman's analysis predicts the average axial stress correctly. They pulled round tensile specimens of steel and copper until a certain amount of necking had occurred. Then they changed the profile radius, R , by machining, and pulled the specimens to a greater strain. They found that the change in average stress caused by changing R was accurately predicted by Bridgman's analysis.

The results of Trozera and Marshall and Shaw do not prove that Bridgman's stress distribution is correct for a necked tensile specimen. Their results only prove that Bridgman's analysis gives the correct ratio of average stress to flow stress. However, the author is of the opinion that the results of Bridgman's analysis are

probably a good approximation to the actual stress distribution in a necked tensile specimen. Bridgman's results will be used in this thesis to determine the stresses in necked (unnotched) tensile specimens.

Are Bridgman's results valid for tensile specimens with machined notches? Clearly, the initial straining of a notched specimen and the development of a neck produce different deformations. The profile radius in the notched specimen is initially produced by machining, while in a neck, the profile radius is completely generated by deformation. However, one might hope that Bridgman's results would be valid for notched specimens with large strains.

Bridgman's results can only be valid for mild notches with a fairly large profile radius. If the profile radius is too small, the stress distribution will also depend on the notch flank angle, and possibly the notch depth. Since neither of these notch parameters is included in Bridgman's analysis, it is obvious that his results cannot possibly be valid if the profile radius is too small. However, one might hope that Bridgman's results would apply to notched tensile specimens with a sufficiently large profile radius after sufficient strain has occurred.

Marshall and Shaw (15) pulled one notched specimen of SAE-4140 steel with an initial value of a/R equal to 0.36. They found that the average stress in the notched specimen was very accurately predicted by Bridgman's results. This does not prove that Bridgman's stress distribution is correct for notched specimens, however. There are an infinite number of different stress distributions that give the

same average stress. The stress distribution in notched tensile specimens is discussed further in this thesis.

2. Mechanisms of Tensile Fracture

The mechanism of cleavage fracture is reasonably well understood (16). Since the mechanism of cleavage fracture was not studied in the investigation reported here, it will not be discussed in this thesis.

The mechanism of fibrous fracture is not well understood. Ludwik (9) showed that fibrous macrofracture is initiated in the interior of a necked tensile specimen. It is usually assumed that fibrous macrofractures begin on the specimen axis, but the author is unaware of any proof of this assumption. Macrofractures in the center of sectioned specimens usually extend over at least 30 per cent of the specimen diameter. The macrofracture could begin anywhere in this region, and not necessarily at the center. In sharply notched specimens, the macrofracture may begin near the notch root, rather than near the specimen axis. (The uncertainty regarding the point at which macrofracture is initiated applies to cleavage as well as fibrous fracture.)

Recent work indicates that fibrous fractures develop by the growth of voids. In this view, microfractures in the form of voids grow and coalesce to form a macrofracture which then spreads to form a final fracture. The term 'void' is used here to denote a more or less equiaxed cavity in the material. This contrasts with a crack in which one dimension is very small compared to the other two.

Rogers (17) and Puttick (18) have shown voids in sectioned

tensile specimens of copper. Hahn, Owen, Cohen, and Averbach (19) sectioned half of a mild steel specimen that had suffered final fracture. Near the final fracture surface they found voids associated with pearlite colonies. It is the author's opinion that the voids shown by Hahn, et al. were created during polishing of the specimen, and not during the pulling of the specimen, as will be explained later in this thesis. Puttick (18) found some cracks associated with inclusions in mild steel tensile specimens.

The above brief description summarizes the little that is known about the mechanism of fibrous fracture as it can be observed under an optical microscope. Considerable effort has been devoted to studying fibrous fracture surfaces under the electron microscope (20), but this work is beyond the scope of interest in this thesis.

A study of the mechanism of fibrous tensile fracture in mild steel must determine whether the fracture develops by the growth of voids or the growth of cracks. Beyond deciding this question, one must obtain a complete description of the mechanism of fibrous tensile fracture in mild steel.

C. Purpose

The purpose of the investigation reported upon in this thesis was to experimentally study the following two aspects of the tensile fracture of a mild steel:

- (1) the local maximum tensile stress and strain, not average values, at which tensile fracture is initiated, over a wide range of conditions;

- (2) the mechanism of fibrous tensile fracture in mild steel.

D. Method of Attack

Round tensile specimens of the two designs shown in Figure 5 were pulled at different temperatures in the range from room temperature down to liquid nitrogen temperature. The two different geometries provided the means for traversing two different stress-strain paths at any given temperature. The notch geometry used was carefully chosen to produce the maximum notch effect, while still retaining the possibility of using Bridgman's results to determine the stress distribution. In order to maximize the notch effect, the notch should be made as sharp as possible (large a/R). However, if the notch were made too sharp, the stress distribution would no longer depend solely on a/R , and Bridgman's results could not be used to determine the stress distribution. These two conflicting requirements led to a choice of a/R equal to 1.5. Although the choice of this value was based on intuition, the experimental results indicate that it was a good choice.

Temperatures from room temperature down to liquid nitrogen temperature were used in this investigation so that different maximum tensile stress-strain paths would be traversed, and so that both cleavage and fibrous tensile fractures would be obtained. Tensile fractures were obtained at average strains from 0.02 to 0.87. The steel used in this investigation was the same as that used by Hendrickson, Wood, and Clark (21) in their study of cleavage fracture at essentially zero strain. Thus, fracture stresses could be compared over a very wide range of conditions.

The notch or neck profile radius, R , was measured during the

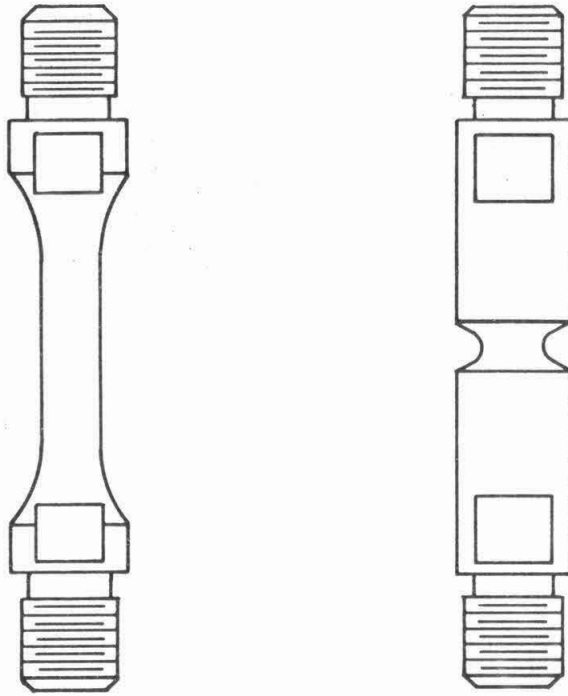


Figure 5. Tensile Specimens.

tensile tests in addition to the usual measurements of force and minimum cross-section diameter. The force and cross-section diameter were used to calculate average stress and average strain. The profile radius, R , was used to calculate the ratio a/R , which, with Bridgman's analysis, gives the stress distribution on the minimum cross section. Thus, the actual maximum tensile stress and strain at fracture were determined over a wide range of conditions.

Metallographic studies were made of sectioned tensile specimens pulled at room temperature short of final fracture in order to determine the mechanism of fibrous fracture.

Arrested macrofractures cannot be obtained when a standard tensile testing machine is employed. Thus, in order to obtain arrested macrofractures for metallographic study, a special Stiff Loading Device was designed and constructed. With this device, macrofractures could easily be retained for subsequent study.

Metallographic techniques which are satisfactory for unstrained mild steel were found to be unsatisfactory for mild steel pulled to strains greater than about 0.25. At strains above 0.25, normal metallographic techniques are increasingly unsatisfactory as the strain is increased. At high strains, apparent microstructural features that are caused by metallographic technique, not by the tensile pulling of the specimen, were frequently observed. Therefore, an important part of this thesis reports on the development of metallographic techniques for studying highly strained mild steel.

The metallographic study of highly strained tensile specimens showed the development of the microfractures and macrofractures

which lead to final fracture.

E. Summary

Tensile specimens of two geometries, one unnotched and one with a circumferential notch, were pulled at different temperatures ranging from 73^oF to -320^oF. Some of the specimens pulled at room temperature, and all of the specimens pulled at lower temperatures, were pulled to final fracture in order to determine the maximum tensile stress and strain at which macrofracture was initiated. Bridgman's results were applied to the necked tensile specimens, and a modification of Bridgman's analysis was applied to notched specimens to determine the actual maximum tensile stress and strain at fracture. Some specimens pulled short of final fracture at room temperature were metallographically studied to determine the mechanism of fibrous fracture.

II. EXPERIMENTATION

A. Tensile Tests

1. Material Tested

The material employed in this investigation was the same steel that was used in previous studies at the California Institute of Technology (21, 22, 23). This steel was obtained from the Columbia Steel Company, Torrance, California, works, where it had been hot rolled to 5/8 in. diameter from one billet of heat number 32882. The analysis as given by the mill is:

Carbon	0.17 %
Manganese	0.39 %
Phosphorous	0.017 %
Sulfur	0.040 %

The machined specimens were annealed in vacuum for one hour at 1650°F. After cooling at the rate of 3°F/min. down to 1050°F, the furnace power was turned off. The average ferrite grain diameter was 0.0008 in. as measured by the linear intercept method. The pearlite lamella had a mean spacing of 0.4 microns as estimated by the method of Pearsall (24). The steel was highly banded by axial columns of pearlite colonies and large axial inclusion stringers. However, the ferrite grains were equiaxed.

2. Equipment

The tensile tests were conducted in a 10,000-pound Instron tensile testing machine, Model TT-C-L. The specimens were threaded into grips between the Instron universal joint at the top, and a spherical seat at the bottom, as shown in Figure 6. The stiffness

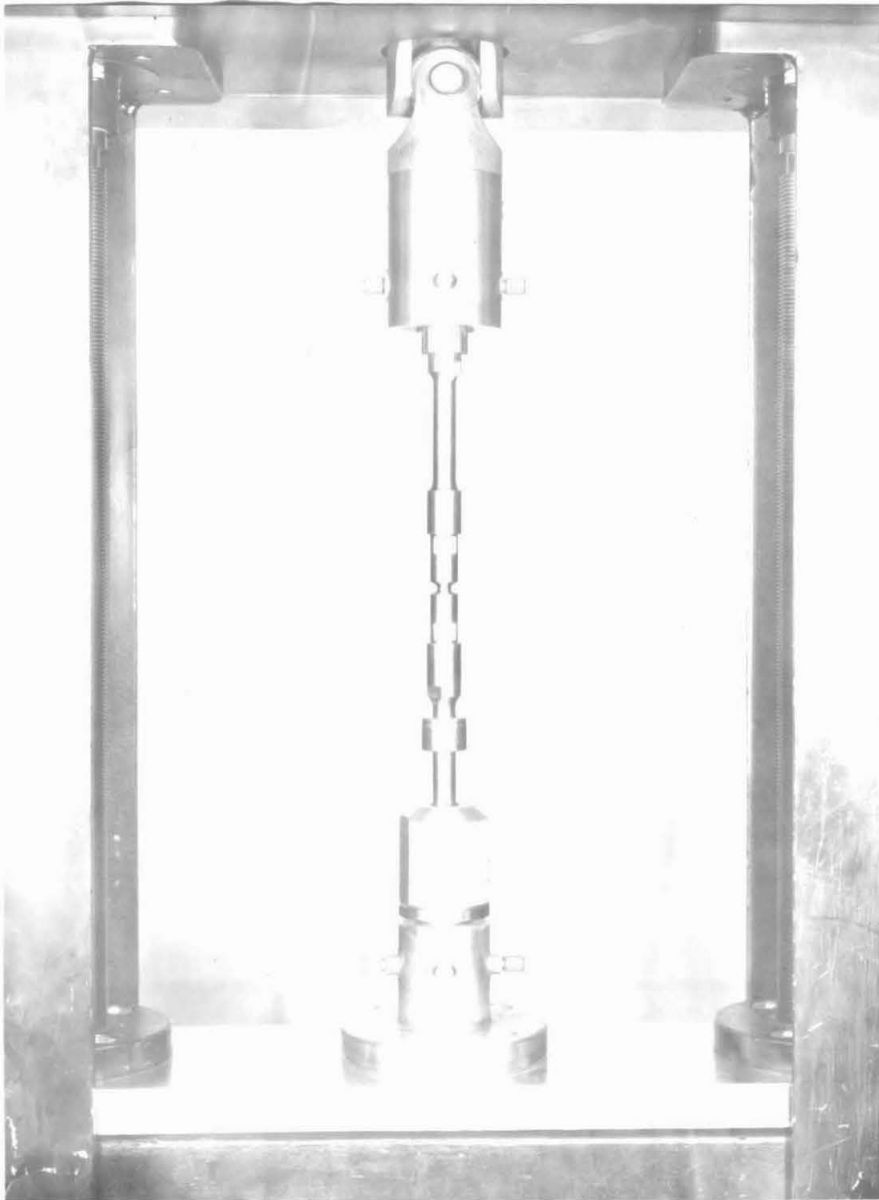


Figure 6. Tensile Test Apparatus.

of this system with a hardened specimen is shown in Figure 7. The low temperature tests required the use of a longer bottom grip which reduced the system stiffness by about 10 per cent.

Low temperatures were produced in a container with double concentric chambers that were separated by an electric heater, as shown in Figure 8. The temperature of -110°F was produced by a mixture of dry ice and Refrigerant 11. Lower temperatures were obtained by employing Refrigerant 12 as the inner bath, liquid nitrogen as the outer bath, and the heater to control the temperature. This system can produce temperatures down to -247°F , which is the freezing point of Refrigerant 12. Tests above -150°F are inconvenient because of the high boiling rate of the liquid nitrogen. Two tests were conducted at -320°F by employing liquid nitrogen in the inner bath.

For tests at temperatures below room temperature, copper-constantan thermocouples were taped to the specimen above and below the test section. The bottom thermocouple was connected to a recorder-controller (on-off), which controlled the heater when it was used. The upper thermocouple was connected to a second recorder. When the control switch was closed, the voltage from a variable transformer was applied directly to the heater. With the control switch open, the power to the heater was reduced by a series resistance. This system was marginal in its ability to hold the temperature constant for the time required in these tests. However, with considerable care, it was possible to hold the temperature constant to within $\pm 2^{\circ}\text{F}$.

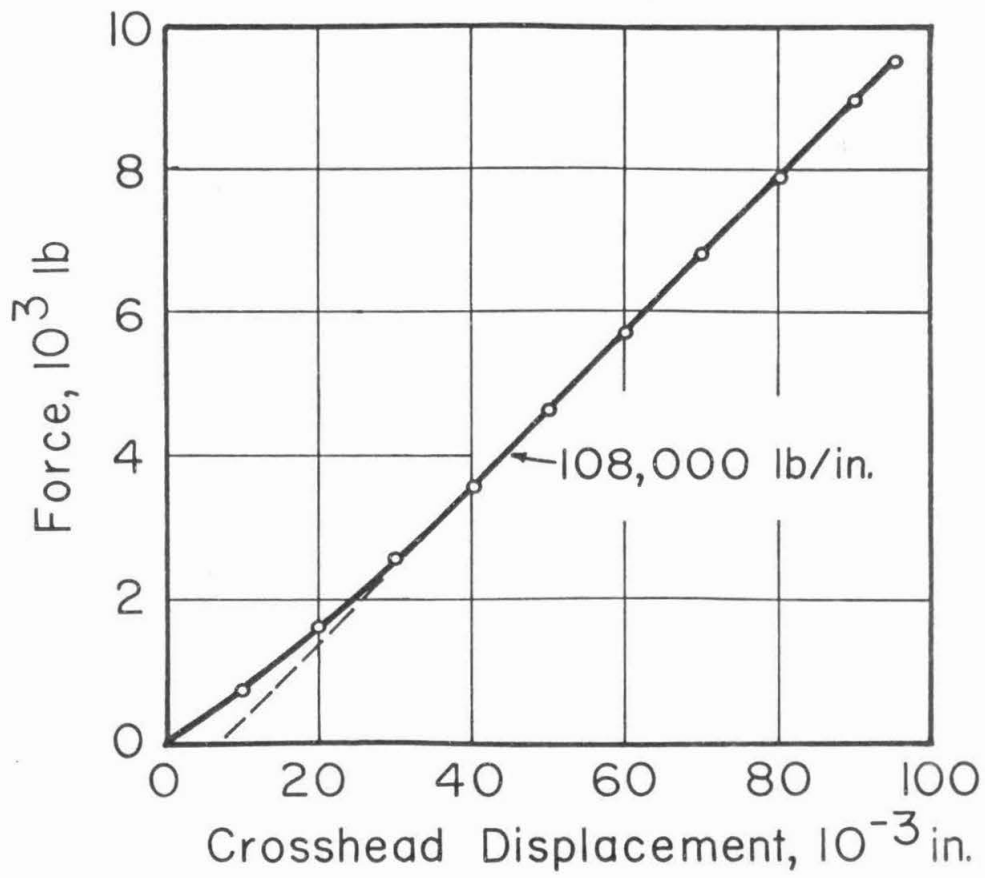


Figure 7. Stiffness of Tensile Test System.

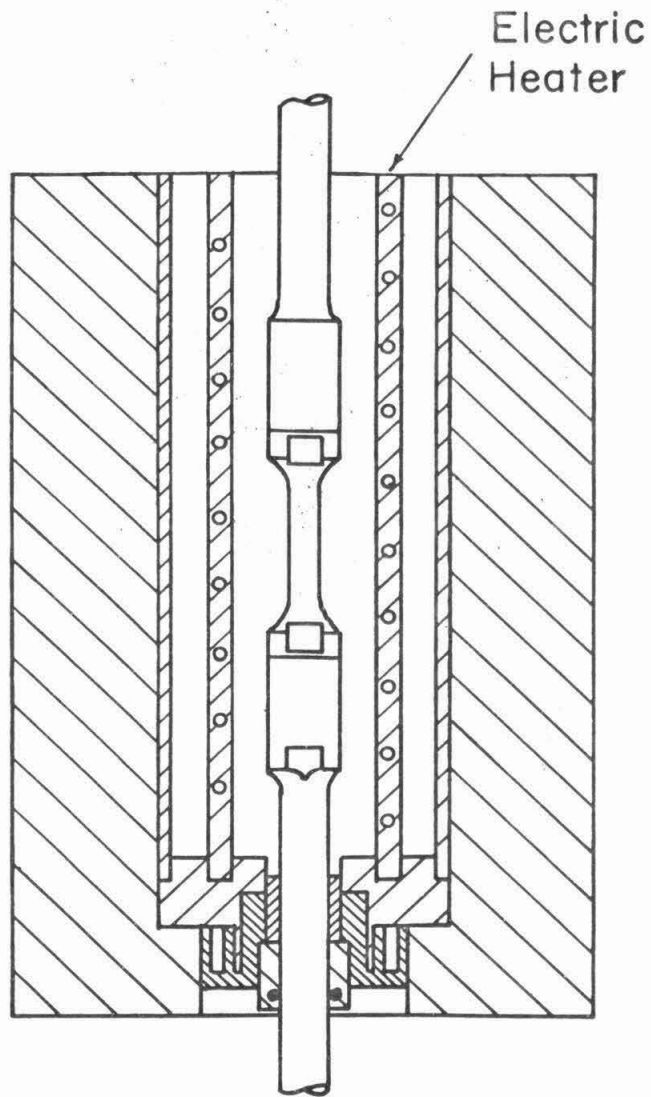


Figure 8. Cold Bath Container.

During the tensile tests in the tensile testing machine, the force was measured on the recorder of the tensile testing machine. The specimen diameter was measured with a pointed micrometer. The profile radius was measured with calibrated tapered rods.

After being strained a certain amount in the tensile testing machine, some specimens were pulled in the special Stiff Loading Device shown in Figure 9. This device was constructed so that macrofractures could be stopped short of final fracture. The stiffness of the Stiff Loading Device was calculated to be at least 20 times that of the Instron system.

3. Experimental Procedures

The crosshead speed was 0.02 in./min. for all tests in the tensile testing machine. The crosshead motion was stopped at intervals to measure the specimen diameter and profile radius. To avoid plastic relaxation at temperatures below room temperature, the crosshead motion was reversed before stopping so that the load was reduced. The average of two perpendicular measurements of the specimen diameter was used to calculate the area. The profile radius was measured by sliding the calibrated tapered rod along the root of the neck or notch until light could just be seen between the rod and the root. With care, such measurements were reproducible to within ± 0.01 in. The profile radius that was used in calculations was the average of two measurements made on opposite sides of the specimen.

The low temperature tensile tests were begun when the temperature readings from both thermocouples were within $\pm 2^{\circ}\text{F}$ of the desired temperature. When the crosshead was stopped to measure

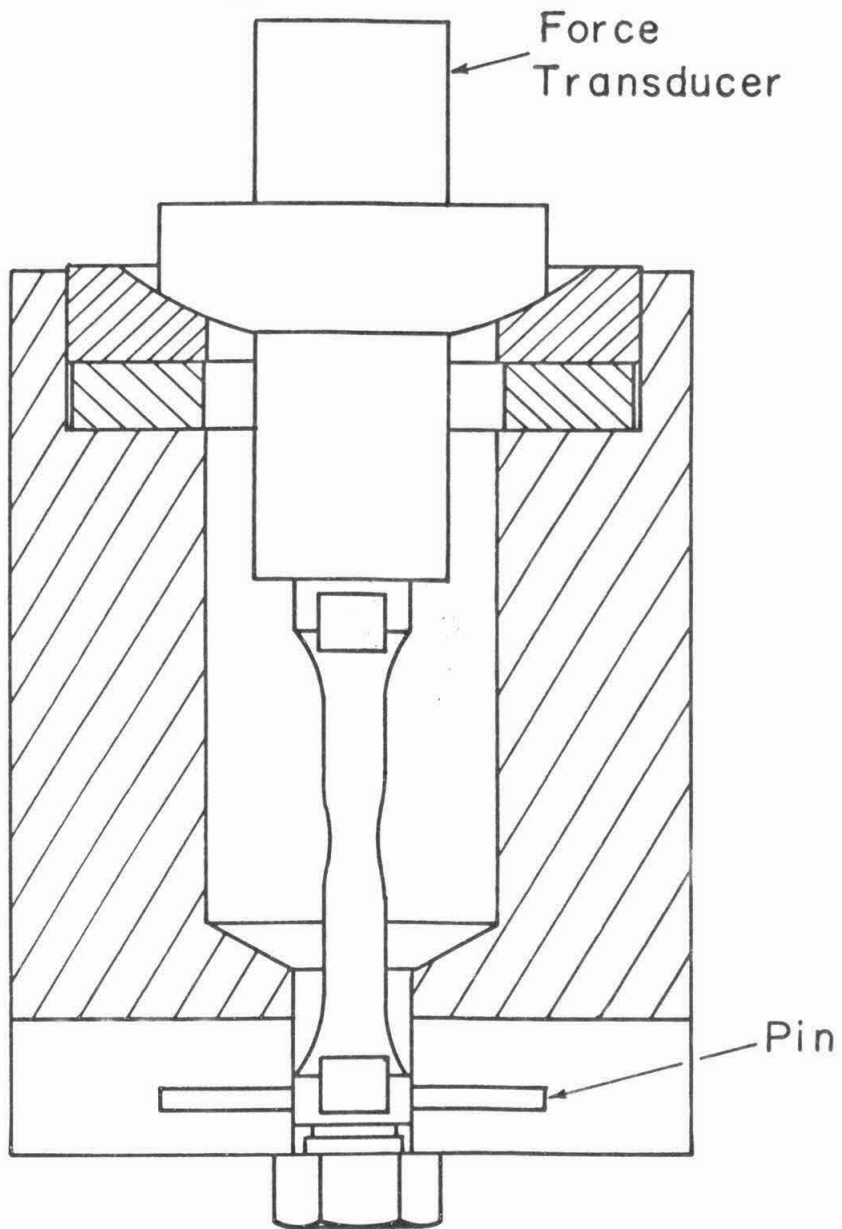


Figure 9. Stiff Loading Device.

the specimen diameter and profile radius, the cold bath was lowered away from the specimen, the measurements made, and the cold bath returned to its original position as quickly as possible. The tensile test was resumed when the readings from both thermocouples were again within $\pm 2^{\circ}\text{F}$ of the desired temperature. Although the temperature was usually held within $\pm 2^{\circ}\text{F}$ of the control temperature, temperature excursions as large as $\pm 5^{\circ}\text{F}$ occurred. Some of the low temperature tensile tests were nonisothermal tests. In a nonisothermal test, the specimen was initially pulled at a constant temperature to a certain strain. After the temperature was lowered, straining was continued at the lower temperature. During some tests the temperature was lowered more than once. Nonisothermal tensile tests will be discussed further in Part III.

The average strain, calculated from measurements of the specimen diameter, was plotted against specimen elongation, as shown in Figure 10. The specimen elongation was calculated from the crosshead displacement, the tensile force, and the stiffness of the Instron system (Figure 7). The strain at fracture was determined by extrapolating the strain versus elongation curve to the fracture elongation, as shown in Figure 10. Diameter measurements that were made after the two fractured pieces had been fitted together gave erroneous values of the strain for the completely fibrous fractures. The strain-elongation curves also allowed accurate determination of the strain with a minimum number of diameter measurements, as the strains at intermediate points could be determined from the curves.

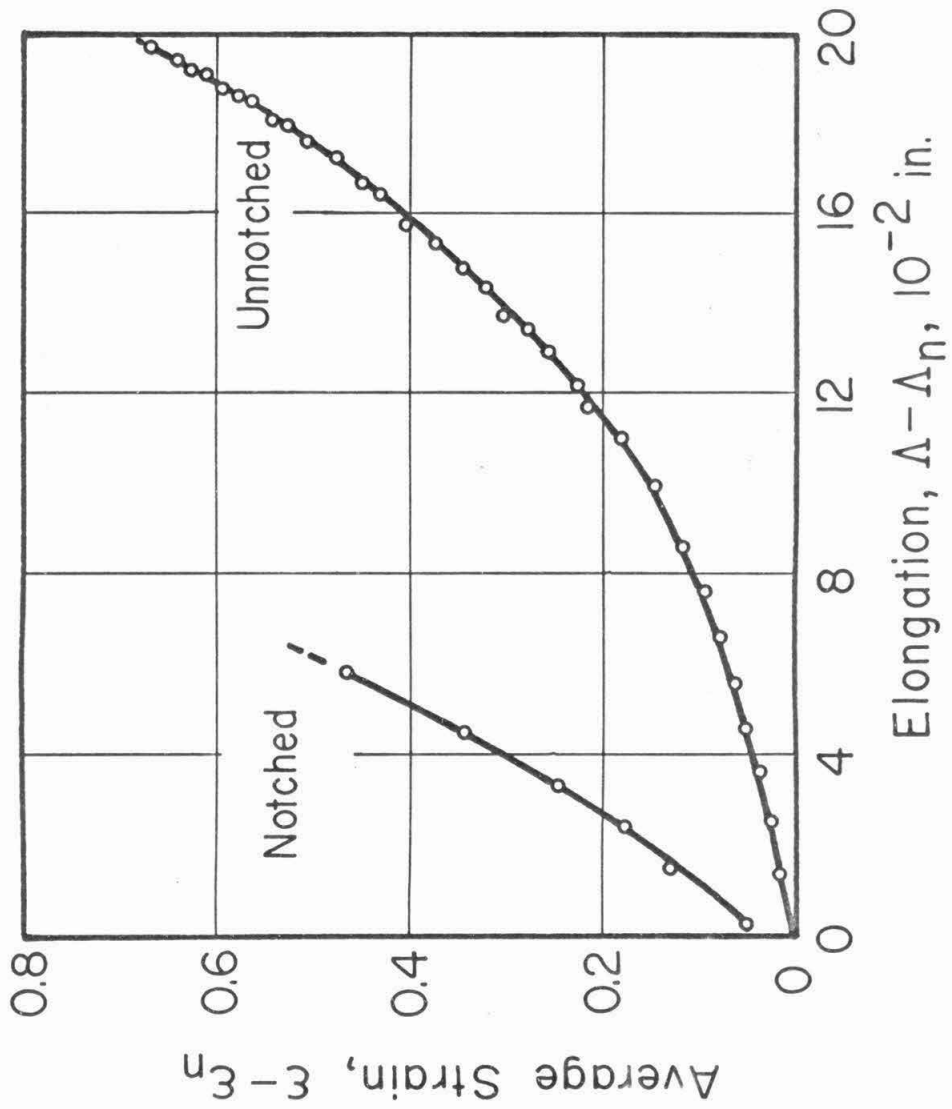


Figure 10. Strain vs. Elongation in Tensile Specimens.

The specimens were pulled in the Stiff Loading Device by turning the nut on the end of the specimen with a wrench. During the pulling of the specimen the strain was not measured. The voltage signal from the force transducer was used primarily to determine when the macrofracture had started. A noticeable increase in the rate at which the force was decreasing signaled the beginning of the macrofracture.

4. Experimental Results

(a) Stress-Average Strain. Typical curves of stress versus average strain at room temperature are shown in Figure 11. The stress shown for the notched specimen and Curve a of the unnotched specimen is the average stress. Curve b is the flow stress as determined from Bridgman's results (Figure 4).

The stress-strain curves were quite reproducible for all notched specimens. However, for the unnotched specimens, the stress-strain curves fell into three groups, as shown in Figure 12. The strains at fracture for Groups 1 and 3 were distinctly different, as shown in Table I. A reason is not known for the division of the unnotched specimens into three groups. Measurements on unstrained portions of specimens from Groups 1 and 3 showed the same hardness. The specimens were supposedly machined from the same stock, and they were annealed in the same manner; in fact, specimens from different groups were annealed together.

(b) Effect of Temperature on Flow Stress. The effect of temperature upon the flow stress as a function of strain is shown in Figure 13 for three typical specimens. The reference specimen, pulled

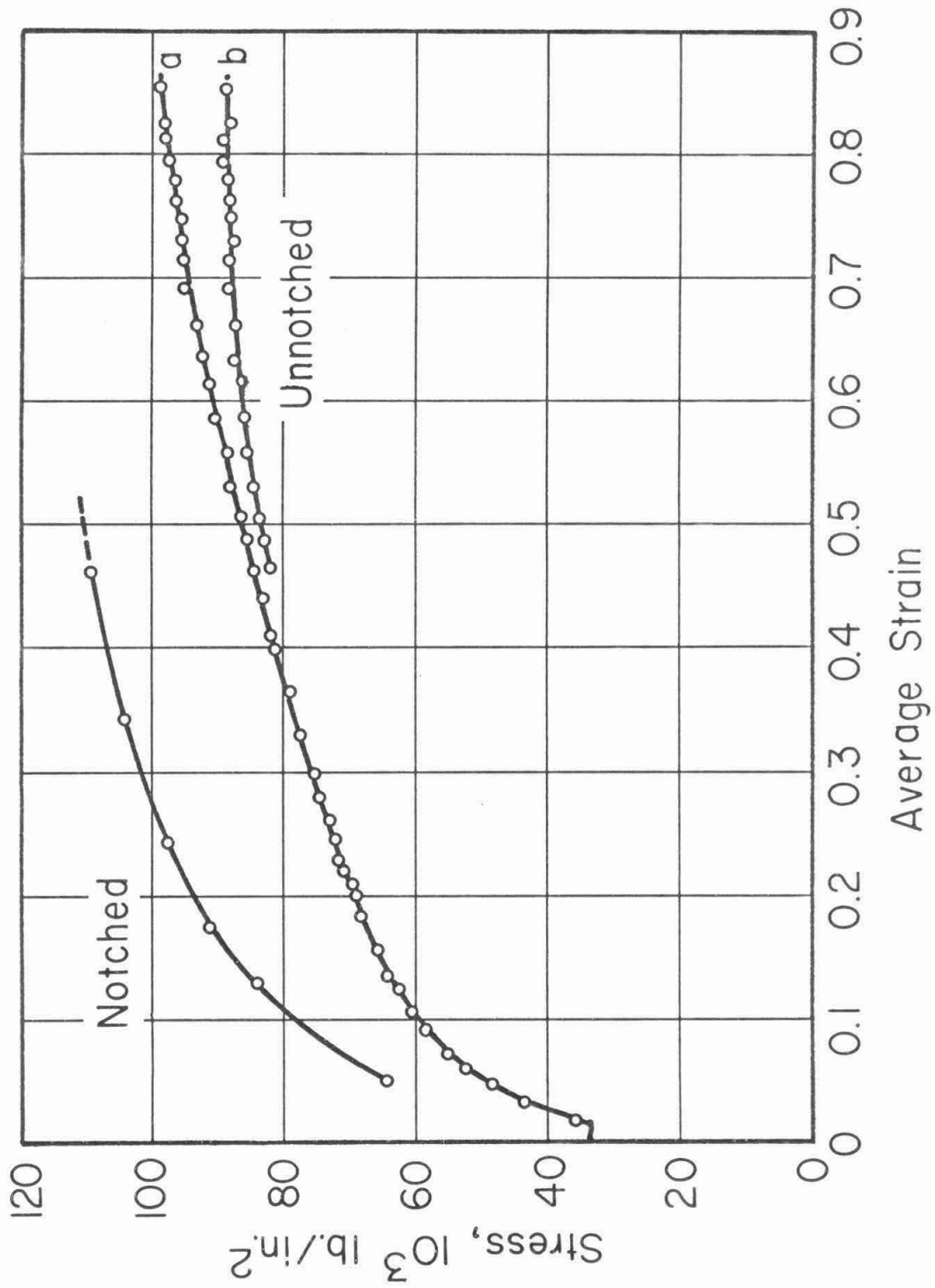


Figure 11. Room Temperature Stress-Strain Curves.

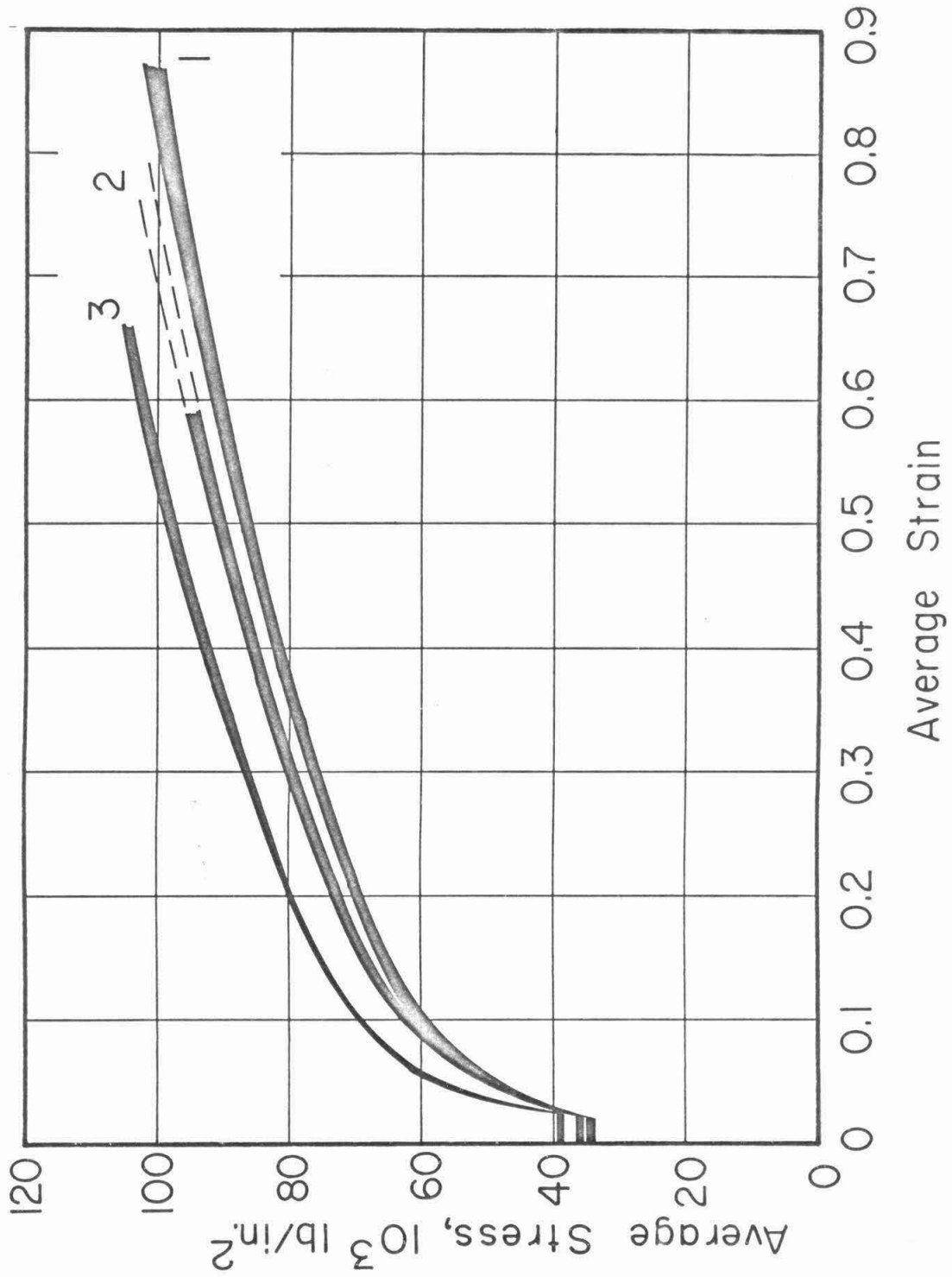


Figure 12. Three Groups of Room Temperature Stress-Strain Curves for Unnotched Specimens.

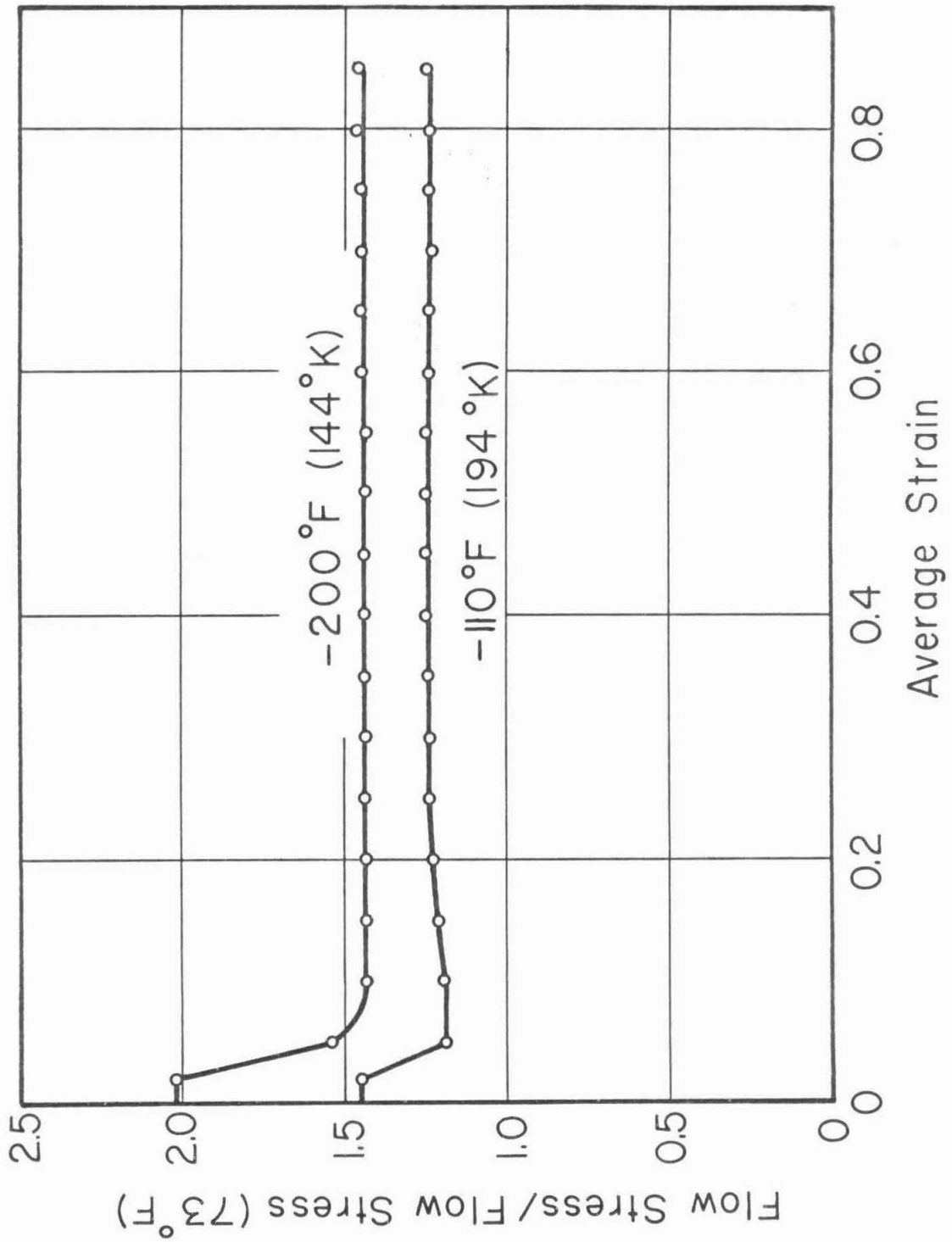


Figure 13. The Effect of Strain upon the Temperature Dependence of Flow Stress.

TABLE I

Average Strain at Fracture for Unnotched Specimens
at Room Temperature

<u>Group 1</u>	<u>Group 2</u>	<u>Group 3</u>
0.80 (1)	0.67 (1)	0.68 (1)
0.86 (1)	0.73 (2)	0.66 (1)
0.87 (1)	0.71 (3)	
0.84 (3)	0.88 (5)	
0.86 (3)	0.89 (5)	
0.84 (3)		
0.84 (3)		
0.85 (3)		
0.86 (4)		
0.85 (5)		

- (1) Pulled to final fracture in Instron
 - (2) Pulled in Stiff Loading Device; no macrofracture
 - (3) Pulled in Stiff Loading Device; macrofracture present
 - (4) Pulled in Instron; no final fracture
 - (5) Pulled to final fracture in Stiff Loading Device; strain determined on broken pieces
-

at room temperature, was from Group 1. Lowering the temperature did not change the average strain at which fibrous fracture occurred, but simply increased the stress by the factor shown in Figure 13.

(c) Effect of Strain upon Specimen Geometry. The geometry of a specimen is described by the ratio of cross section radius to

profile radius, a/R . The measured variation of a/R with strain is shown in Figure 14. The large percentage scatter for unnotched specimens is caused by two factors: (1) the plot contains points obtained at different temperatures; (2) the zero point, ϵ_n , is difficult to determine with sufficient sensitivity. Although in previous investigations (13, 15) the relationship between a/R and average strain was found to be linear, the curve in Figure 14 has positive curvature.

(d) Fracture Data. The values at fracture for the average stress, average strain, and a/R , and the appearance of the fracture surfaces are given in Table II for unnotched specimens and in Table III for notched specimens. Table II also gives the values of the upper yield stress, lower yield stress, and ultimate tensile strength. All of the data in Tables II and III are from specimens that were pulled to final fracture in the tensile testing machine. The tensile tests of specimens that were numbered 127, 9, 10, 11, 16, and 17 were non-isothermal tests.

B. Metallographic Studies

This investigation included metallographic studies of two different phenomena: (1) the displacements and strains in the tensile specimens were investigated; (2) the mechanism of fibrous fracture was studied.

1. Displacements and Strains

(a) Radial Displacement. On the etched surface of a sectioned notched specimen the amount of the radial displacement could be qualitatively determined from the deformation of the banding in the steel, as is shown in Figure 15. Therefore, the banding was used as

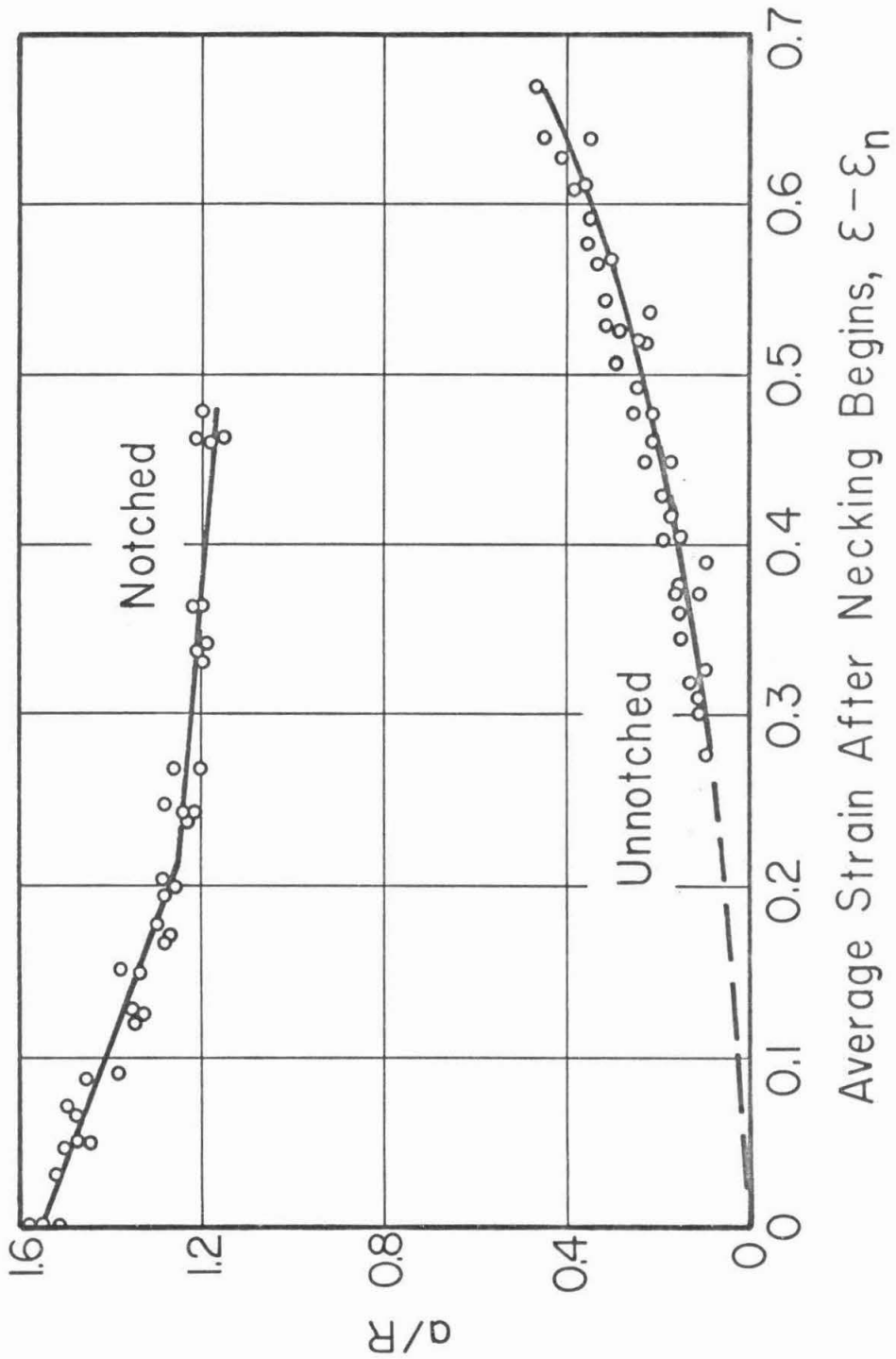


Figure 14. Section Radius Divided by Profile Radius vs. Strain.

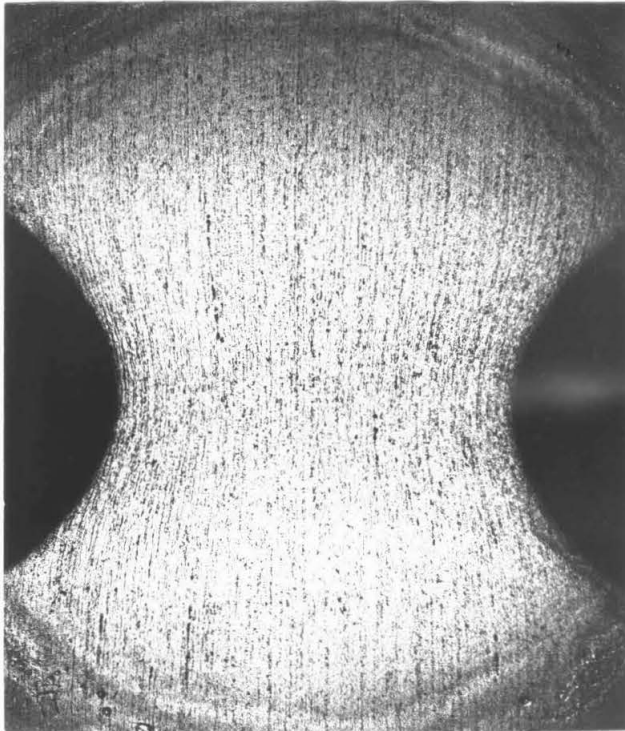


Figure 15. Deformation of Banding in Notched Specimen.

TABLE II

Flow and Fracture Data for Unnotched Specimens Fractured in Tensile Testing Machine

(All stresses, 10^3 lb. /in. 2)

Specimen Number	Temperature °F	Flow			Fracture			Appearance: F-Fibrous C-Cleavage
		Upper Yield Stress	Lower Yield Stress	Ultimate Tensile Strength	Average Stress	Average Strain	a/R	
96	73	51.9	38.6	65.1	104	0.68	0.30	F
97	73	48.1	34.4	57.6	97.2	0.80	0.38	F
98	73	50.5	33.8	56.5	99.3	0.86	0.48	F
99	73	46.4	34.3	57.5	103	0.87	0.49	F
100	73	50.0	38.5	65.5	105	0.66	0.30	F
103	-110	63.4	49.6	71.8	116	0.68	0.22	F
104	-110	61.9	49.2	70.0	122	0.84	0.36	F
105	-110	59.4	49.1	69.2	121	0.84	0.37	F
106	-110	62.0	49.5	71.5	128	0.88	0.44	F
109	-200	80.5	66.0	80.1	133	0.83	0.34	F-C
110	-200	81.9	66.8	88.9	139	0.62	0.19	F-C
111	-200	83.9	67.5	81.7	142	0.86	0.39	F-C
124	-240	95.5	75.5	-	138	0.76	-	F-C
125	-320	125	-	-	-	0.02	0	C
127	-320*	-	-	-	132	0.14	0	C

* Pulled to average strain of 0.07 at -240°F

TABLE III

Fracture Data for Notched Specimens Fractured inTensile Testing Machine

<u>Specimen Number</u>	<u>Temperature, °F</u>	<u>Average Stress 10³ lb./in.²</u>	<u>Average Strain</u>	<u>a/R</u>	<u>Appearance: F-Fibrous C-Cleavage</u>
1	73	114	0.53	1.16	F
2	73	111	0.52	1.16	F
3 (1)	73	111	0.56	1.24	F
4 (1)	73	112	0.57	1.24	F
5	-110	140	0.54	1.22	F-C
6	-110	138	0.50	1.20	F-C
7	-200	96.5	0.02	1.5	C
8 (2)	-200	99.0	0.02	1.5	C
9	-200 (3)	114	0.07	1.48	C
10	-200 (3)	138	0.25	1.22	C
11	-190 (3)	138	0.24	1.24	C
16	-170 (3)	130	0.23	1.30	C
17	-190 (3)	121	0.13	1.42	C
18	-150	127	0.26	1.28	C

(1) Notch had 120-degree flank angle.

(2) Notch root was hand polished.

(3) Specimen was initially strained at higher temperature.

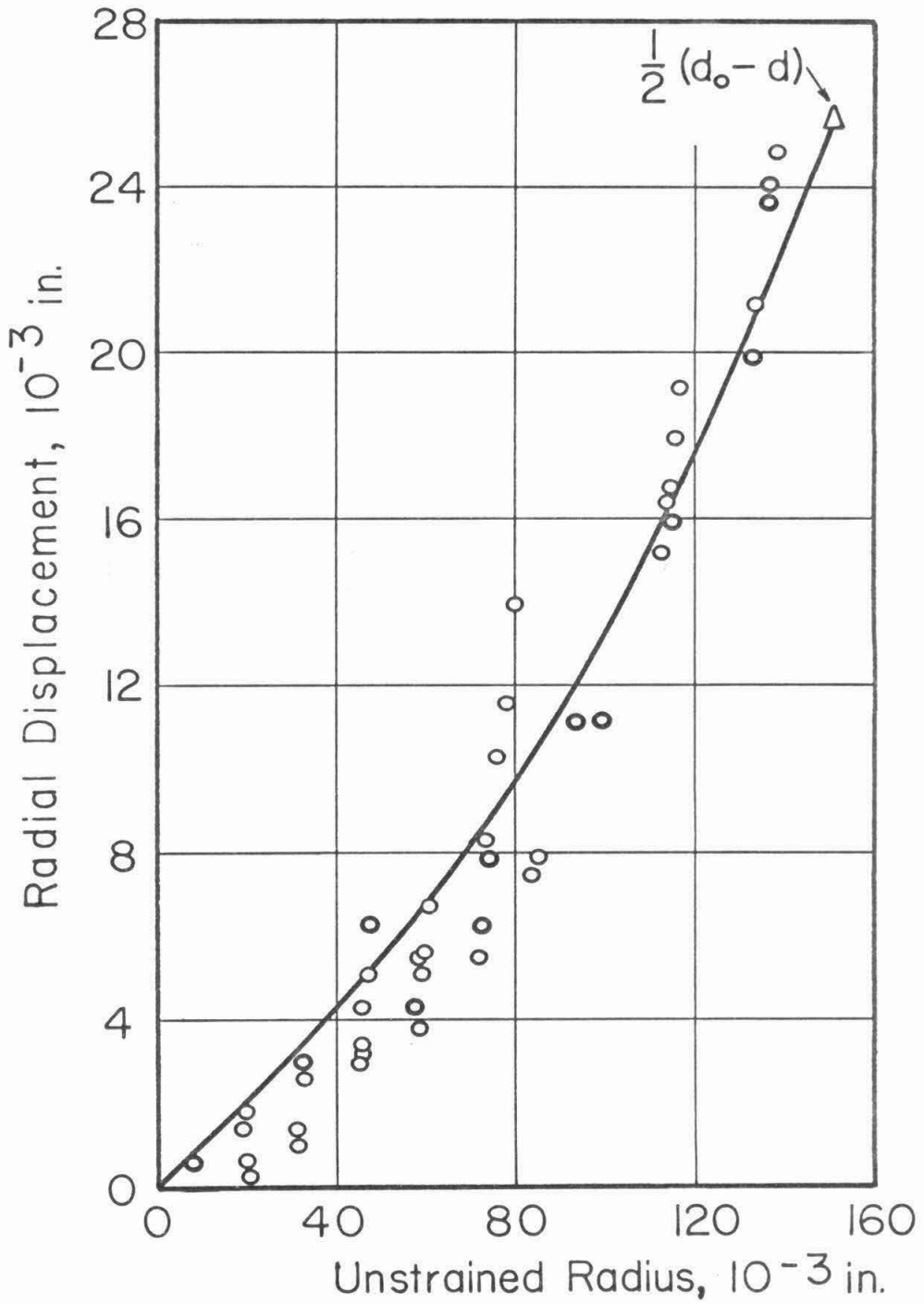
fiducial markers in quantitatively measuring the radial displacement on the minimum cross section of a notched specimen. Various photographic techniques were found to be unsatisfactory. The best results

were obtained by mounting the etched specimen on the traveling stage of a microscope, and following the banding under the microscope from the minimum section out to the undeformed region. First the specimen axis was aligned parallel to one axis of the stage. Then the two micrometer dials were turned to traverse the stage so that the specimen passed under the microscope while moving parallel to the local direction of the banding. Thus, the banding was followed from the minimum section out to the unstrained region. The radial displacement was the change in reading of the micrometer dial which was perpendicular to the specimen axis. The results of many such measurements on one notched specimen are shown in Figure 16. The darker circles represent two measurements.

The scatter shown in Figure 16 indicates the accuracy of the measured displacements. The micrometer measurements are accurate within 0.0001 inch, so this is an insignificant source of error. All of the banding may not have been exactly parallel to the specimen axis before straining. Also, in some indistinct regions, the banding was hard to follow.

The displacements at the axis and the surface are known with much more accuracy than at the intermediate positions. Since a straight line through these two points in Figure 16 does not agree with the other data points, Bridgman's assumption of uniform strain is not valid for this notched specimen. The curve drawn on Figure 16 represents an equation which will be discussed further in Part III.

(b) Axial Strain. Attempts to measure the axial strain were made with three different techniques: (1) grain boundary angles,



(2) linear intercepts with grain boundaries, (3) microhardness. All three methods had poor accuracy, but the results agreed that in a notched specimen the strain is greater near the notch root than on the specimen axis. Only the method based on grain boundary angles will be described here.

The most common type of grain boundary intersection is three grain boundaries intersecting at a point. At the intersection, the acute angle, θ , between a grain boundary and the specimen axis can be considered a random variable. In an unstrained specimen the mean value of θ should be 45 degrees. As straining progresses, the mean value of θ should decrease. A theoretical analysis of the relationship between the mean value of θ and strain is presented in Appendix I. If the strain is uniform over the cross section, the results are as shown in Figure 17. The limit curves are displaced from the mean curve by two standard deviations based on an assumed 90 measurements. Most of the experimental values shown are the mean of 90 measurements. The experimental values fall within the theoretical prediction except for the measurement made near the root of the notched specimen. This measurement shows greater strain than would be expected if the strain were uniform. Also, the spread between the strain on the axis and the strain near the surface is significantly greater for the notched specimen than for any of the unnotched specimens. Thus, the grain boundary angles indicate that in a notched specimen the strain near the notch root is greater than the strain on the specimen axis.

(c) Plastic Region in Notched Specimen. Fry's reagent, which

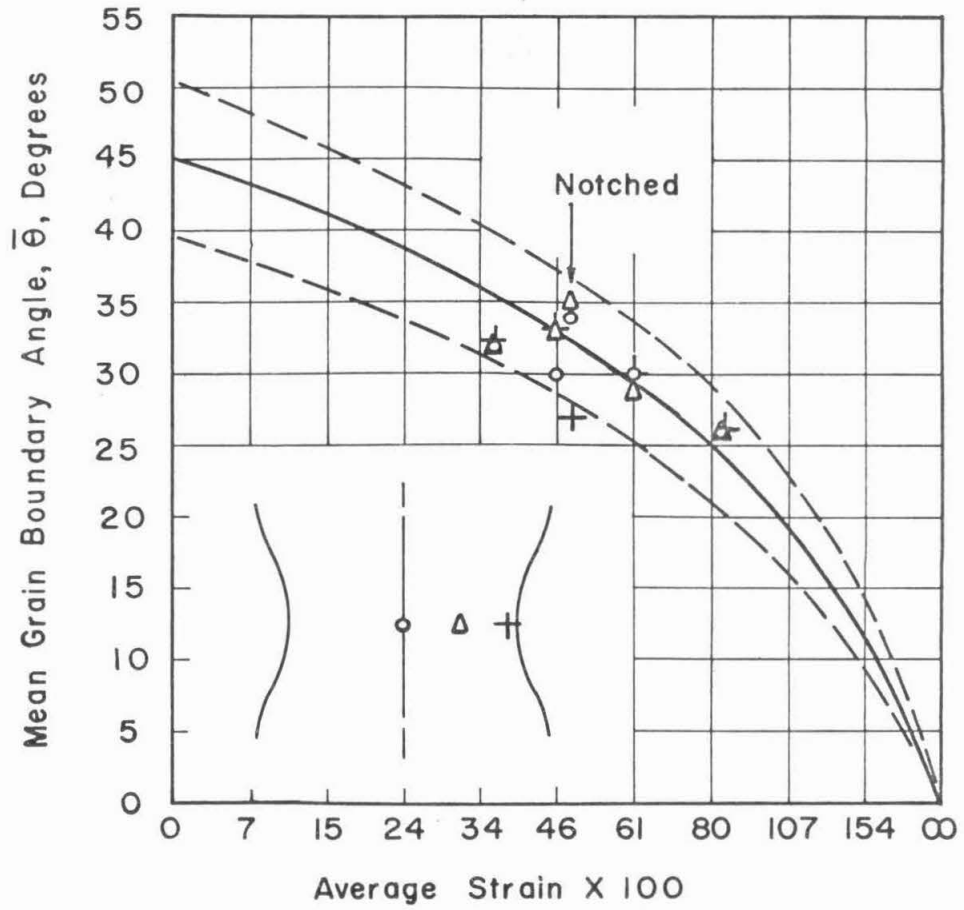


Figure 17. Grain Boundary Angle vs. Average Strain.

reveals the plastic zone in some steels (25), had negligible effect upon the steel used in this investigation. Considerable experimentation resulted in the discovery that the plastic zone is revealed by the following etching reagent:

30 cc methyl alcohol

0.1 cc hydrochloric acid

6 mg $\text{CuCl}_2 \cdot 2\text{H}_2\text{O}$

10 mg $\text{FeCl}_2 \cdot 4\text{H}_2\text{O}$

Figure 18 shows a specimen with average strain of 0.35 which was etched for 15 minutes at room temperature. The darkening on the corners and top and bottom edges in the photograph is due to rounding of the specimen, not etching. The plastic zone intersects the specimen surface near the point where the straight flank meets the round root of the notch. This verifies that the radius should be the only notch parameter affecting the stress distribution.

The etch makes the plastic zone copper colored, while the undeformed zone remains steel colored. The color difference made the contrast much sharper in direct observation than it appears on the photograph. Microscopic observation revealed that the copper coloring was roughly uniform, with no individual etch pits that might be associated with dislocations. The contrast produced by the etch was found to be erratic. The specimen shown in Figure 18 had been aged briefly at 350°F while it was being mounted in lucite. There was some evidence that this etching reagent should be freshly mixed shortly before use. Experiments on a tapered tensile specimen indicated that the etch was sensitive to strains approximately equal to

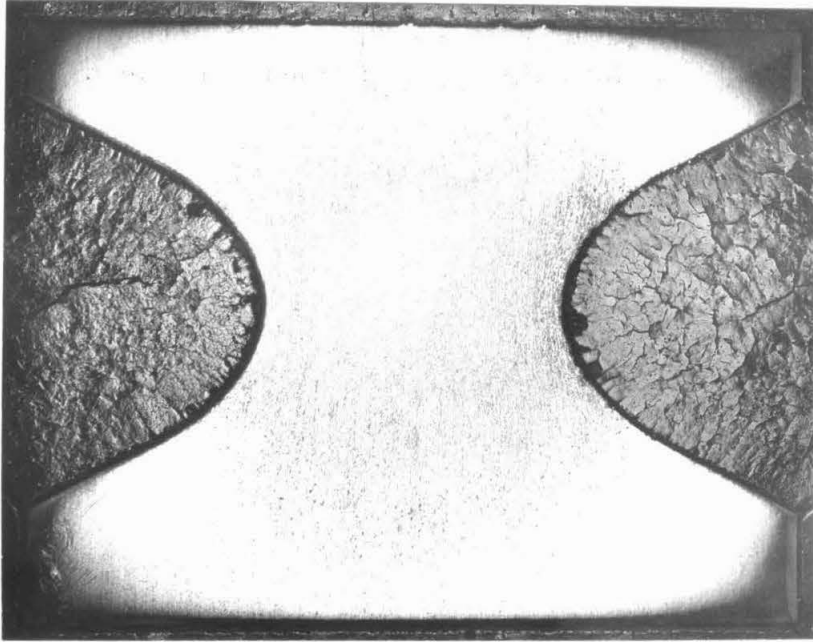


Figure 18. Plastic Zone in Notched Specimen.

Lüders strains.

2. Mechanism of Fibrous Fractures

(a) Microcracks. Many microcracks were found in specimens that had been pulled to various strains, sectioned, polished, and sometimes etched. Etching was not necessary in order to reveal the microcracks. When the specimens were rinsed and briefly dried in an air jet, liquid bled out of the microcracks. This is the clearest evidence that the microcracks were not some other type of microstructural feature. When the average strain exceeded approximately 0.25, the microcracks made proper metallographic polishing difficult. The top photomicrograph in Figure 19 shows a microcrack revealed by careful mechanical polishing. The bottom photomicrograph shows the same region after subsequent normal mechanical polishing. The torn-out steel particle is typical of the surface produced by normal polishing technique. The tearing out of many such particles gives the surface the appearance of Swiss cheese, as shown in Figure 20. Although few surfaces were this bad, special polishing techniques were required to avoid excessive removal of particles.

The sectioned specimens were mounted in lucite and hand ground on wet 240, 320, 400, and 600 silicon carbide papers. With minor exceptions, the grinding did not pull particles out of the surface of the specimens. Grinding was followed by mechanical or electrolytic polishing. The following four paragraphs describe the normal mechanical and electrolytic polishing techniques as well as the special mechanical and electrolytic polishing techniques which gave improved results on highly strained specimens. The techniques that are to be

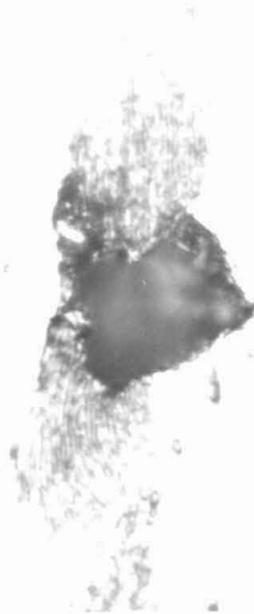


Figure 19. Top, Careful Polish; Bottom, Normal Polish, Etched in 5 Per Cent Nital, 2000X.



↔ Axis

Figure 20. Holes Caused by the Enlargement of Microcracks and/or the Removal of Particles Bounded by Microcracks (as in Figure 19). Electropolished, Average Strain: 0.86, 250X.

described are four different polishing techniques. The general practice was not to employ these techniques in combination with one another.

Normal mechanical polishing was done on a rotating wheel covered with AB Microcloth impregnated with 4-8 micron diamond paste and AB Metadi fluid. The hand-held specimen was rotated around the center of the wheel with fairly heavy pressure. This procedure was repeated with moderate pressure on a similar wheel with 0-2 micron diamond paste.

Specimens were electropolished on a Buehler electropolishing machine in which the electrolyte flowed against the surface of the specimen. The electrolyte was:

- 5 % perchloric acid (61 %)
- 95 % glacial acetic acid.

Very good surfaces were produced on unstrained specimens which were polished 40 seconds at 30 volts and finished at 80-90 volts for five seconds. Some experimentation was necessary to determine the optimum size for the orifice upon which the specimen rested.

Highly strained specimens were mechanically polished on silk cloth with 4-8 micron diamond paste and felt cloth with 0-2 micron diamond paste. The specimen was oscillated radially a short distance, but was not rotated. Light pressure was used on the felt cloth. Obtaining good results with this procedure required great care and considerable luck.

The best technique for electropolishing highly strained specimens consisted of polishing for five seconds at 70 volts. Some wavi-

ness, remnants of scratches from 600 paper, was visible at 100X, but was not apparent at 500X or greater magnification. At the end of this investigation, all highly strained specimens were being electropolished for five seconds at 70 volts, as this technique was faster and more reproducible than mechanical polishing.

Electropolishing for five seconds at 70 volts is far from an ideal technique. An ideal technique would produce a flat, smooth surface with all of the cracks exposed, but not enlarged. In practice, the first cracks to be exposed are enlarged and particles are pulled out before the last crack is exposed. The best result is a compromise which exposes as many cracks as possible without enlarging too many of them excessively. Since not all cracks can be exposed without enlarging many of them excessively, it is impossible to make an exhaustive survey of all of the cracks present on one surface. Instead, one finds and photographs all of the interesting microcracks which are exposed on a given surface. After this is repeated on enough surfaces, one obtains a complete catalog of the type of microcracks present. Photomicrographs of typical microcracks will be presented in Part III.

Measurements were made of the total length of the microcracks that were present per unit area at two different positions on the polished surfaces of sectioned specimens that had been pulled to different strains. The specimens were polished so that all of the microcracks were exposed, which enlarged most of the cracks, as is shown in Figure 20. A measurement was made of the total length of all of the microcracks in a photomicrograph such as Figure 20. The

author judged the length that the microcracks had had before they were enlarged. This judgment was based on the author's observations of the shape of the typical microcracks that were present in the specimens. The total length of the microcracks in a photograph was divided by the area that was shown in the photograph, to give the total microcrack length per unit area of the specimen. (The data are stated in terms of the unmagnified dimensions.) Such measurements were made on the minimum cross section of the specimen, both on the axis and near the outside surface. Figure 21 shows the total length of microcracks per unit area on the polished plane of four unnotched specimens and one notched specimen. Both data points that are plotted at a given strain are from the same specimen.

(b) Macrofractures. A specimen with a macrofracture is more difficult to properly polish than a specimen that contains only microcracks. The macrofracture in the notched specimen shown in Figure 22 appears to consist of holes with good material in between. However, the "good" regions are actually severely cracked, as shown in Figure 23. Figure 23 shows cracks that are surrounding pieces of metal which could easily be pulled out. How can such holes caused by polishing be distinguished from regions actually opened up during pulling? The author concluded that the macrofracture can be accurately observed only if it is filled with a binder before particles of metal have had an opportunity to come out.

A technique was developed for filling the macrofracture with epoxy resin. The neck of the tensile specimen was mounted in bakelite, as shown in Figure 24a. The back side of the bakelite was faced

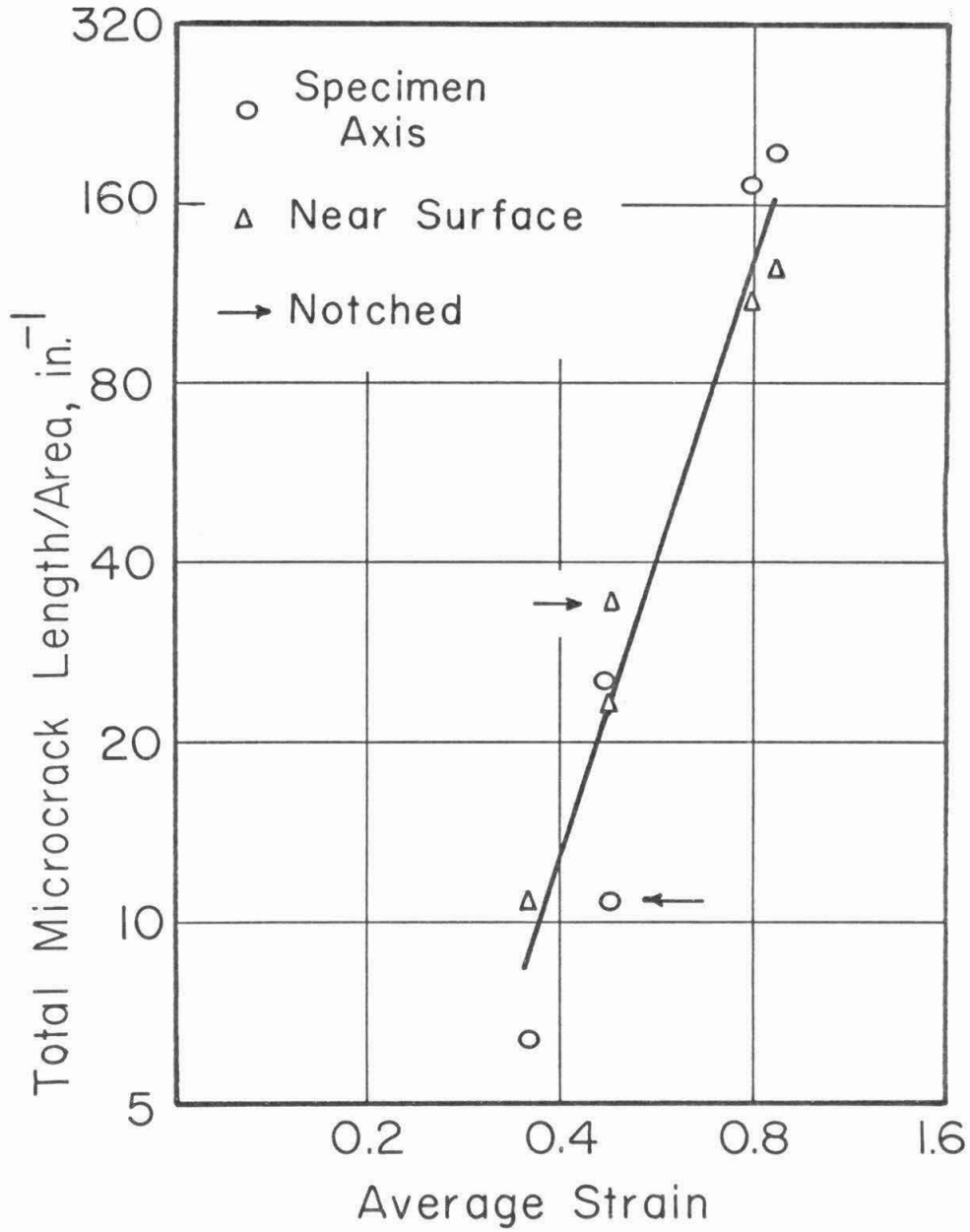


Figure 21. Total Microcrack Length/Unit Area vs. Average Strain for Four Unnotched Specimens and One Notched Specimen.

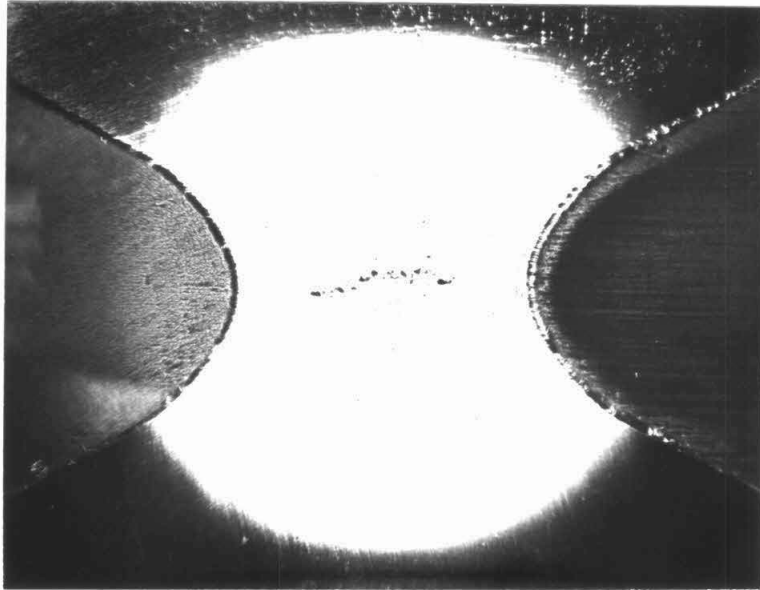
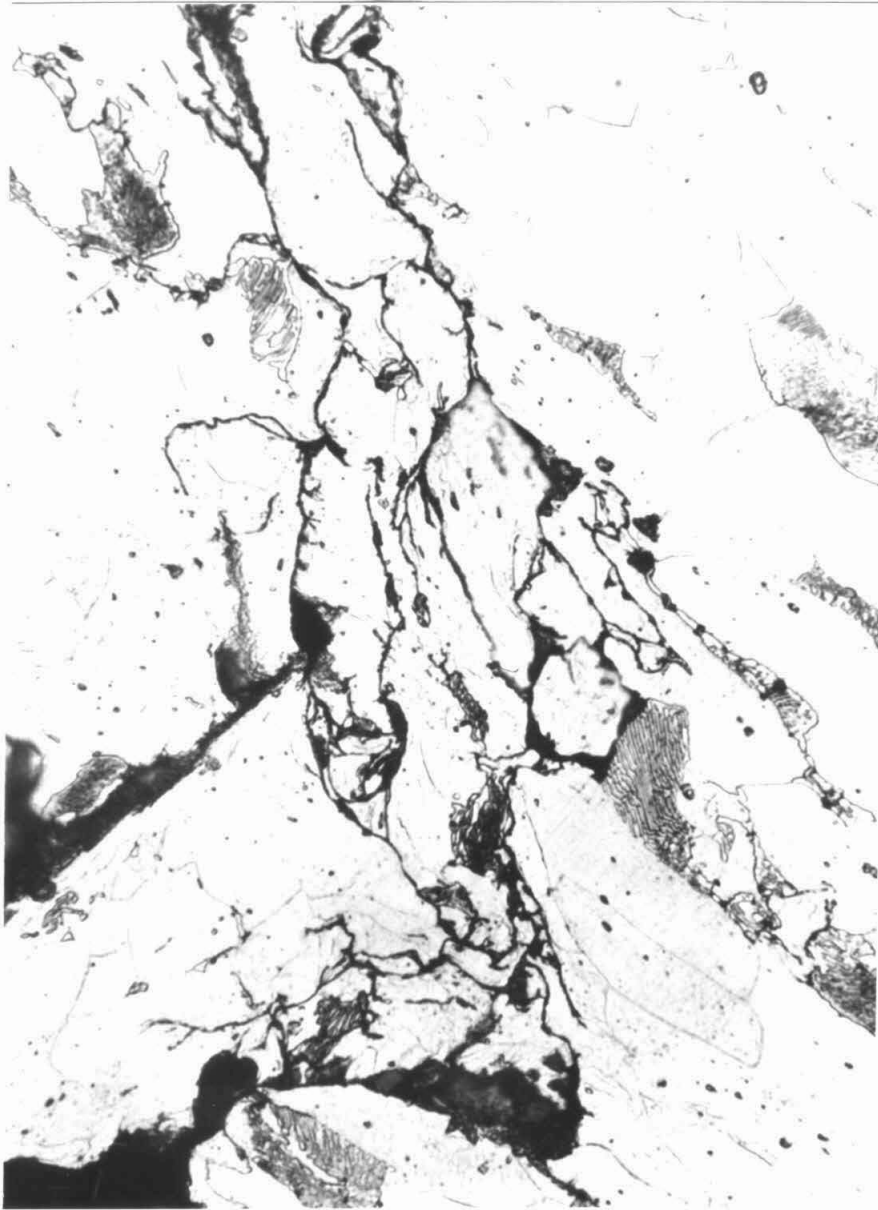


Figure 22. Macrocrack in Notched Specimen.

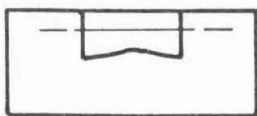


↕ Axis

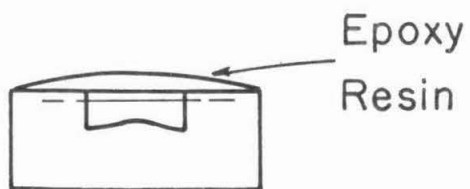
Figure 23. Fine Cracks in Macrofracture of Notched Specimen, 750X.



a.



b.



c.

Figure 24. Procedure for Filling Macrocrack with Epoxy Resin.

off on a lathe, and the front side was machined tangent to the neck (Figure 24b). About half of the radius of the specimen (0.050 in.) was machined off on a lathe, and the specimen was polished and etched. No macrofracture was visible. Another tenth of the radius (0.010 in.) was removed by light machine cuts and polishing, and the specimen was etched. The macrofracture was visible, relatively short in length, and consisted mostly of fine cracks. To thoroughly expose the cracks, the specimen was etched ten seconds in five per cent nital, and placed in methanol for 18 hours to remove the etching reagent. The methanol was driven off by heating the specimen to 250°F. After cooling in a desiccator, the specimen was placed in a bell jar together with a beaker of epoxy resin (Armstrong, three parts C-4, two parts activator W). After 15 minutes of evacuation, the bell jar pressure was below five microns. After the epoxy resin was poured over the surface of the specimen (Figure 24c), air was admitted to the bell jar until atmospheric pressure was reached. This procedure allowed the resin to flow into the macrofracture with air pressure assisting the flow rather than resisting it. The specimen was placed in an oven at 250°F for half an hour. The excess epoxy resin was removed by machining in a lathe.

The procedure described above worked very well. The specimen was ground and polished successively until the polished plane was 0.007 in. beyond the specimen axis. The epoxy resin was found in places that might otherwise have been mistaken for polishing holes. With one minor exception, voids that were not filled with resin were not found. Distinguishing between the resin and the large inclusion

stringers proved to be a problem. However, etching 10 minutes in a 20 per cent aqueous solution of hydrofluoric acid (48 per cent) dissolved the inclusions, but had no apparent effect upon the resin. Therefore, the entire macrocrack was positively identified by the presence of the epoxy resin. The resin-filled macrocrack will be shown in Part III in a series of photomicrographs taken at different distances from the specimen axis.

III. DISCUSSION

A. Deformation and Stress in Notched Tensile Specimens

1. Deformation

The radial displacement on the minimum cross section of the notched specimens that were used in this investigation was not a linear function of radius as was assumed in Bridgman's stress analysis (see Figure 16). Proper representation of the data requires that a nonlinear term be included in the radial displacement function;

$$u_r/a_o = [f(\frac{a}{a_o})]r_o/a_o + [g(\frac{a}{a_o})](r_o/a_o)^n \quad [3]$$

where

r_o is the initial distance from a point on the minimum cross section to the specimen axis,

a_o is the initial outside radius of the minimum cross section,

a is the instantaneous outside radius during pulling,

n is an integer.

The ratio a/a_o in Equation 3 is simply a convenient parameter which represents the progress of straining.

Round tensile specimens have both axial symmetry with respect to the specimen axis and reflection symmetry with respect to the plane of the minimum cross section. The axial and reflection symmetry of notched tensile specimens imposes restrictions upon the radial displacement function. The analysis in Appendix II shows that the symmetry imposes the restriction that the exponent n cannot be equal to two. Therefore, n was chosen to be three, because three is permitted by symmetry and gives good agreement with the data. The

equation chosen to represent the radial displacement is

$$u_r = (a-a_o)[0.6r_o/a_o + 0.4(r_o/a_o)^3] \quad [4]$$

which is plotted as the curve in Figure 16. The choice for the form of the coefficients was based solely upon simplicity. The numerical coefficient of the linear term was assigned the maximum value which was consistent with the data. The amount of the nonlinearity was minimized because the author wished to be conservative in determining the effect of the nonlinearity upon the resulting stress distribution. The nonlinearity in Equation 4 causes a large variation of strain, as is shown in Figure 25.

2. Stresses

The calculation of the stress distribution on the minimum cross section of the notched specimens which were tested in this investigation is presented in Appendix III. The stress calculation follows Bridgman's, except that the radial displacement is assumed to be given by Equation 4 instead of by the linear equation

$$u_r = (a-a_o)r_o/a_o \quad [5]$$

which was assumed by Bridgman. Bridgman was able to obtain closed form solutions which give the stress distribution for any values of flow stress and a/R , as is shown in Figure 4. The nonlinearity of Equation 4 made it impossible for the author to obtain a closed form solution for the stress distribution. Instead, the stress distribution was computed numerically for the particular case where the flow stress-strain curve is that given in Figure 11, and the curve of radius ratio versus average strain ($a/R-\epsilon$) is that given in Figure

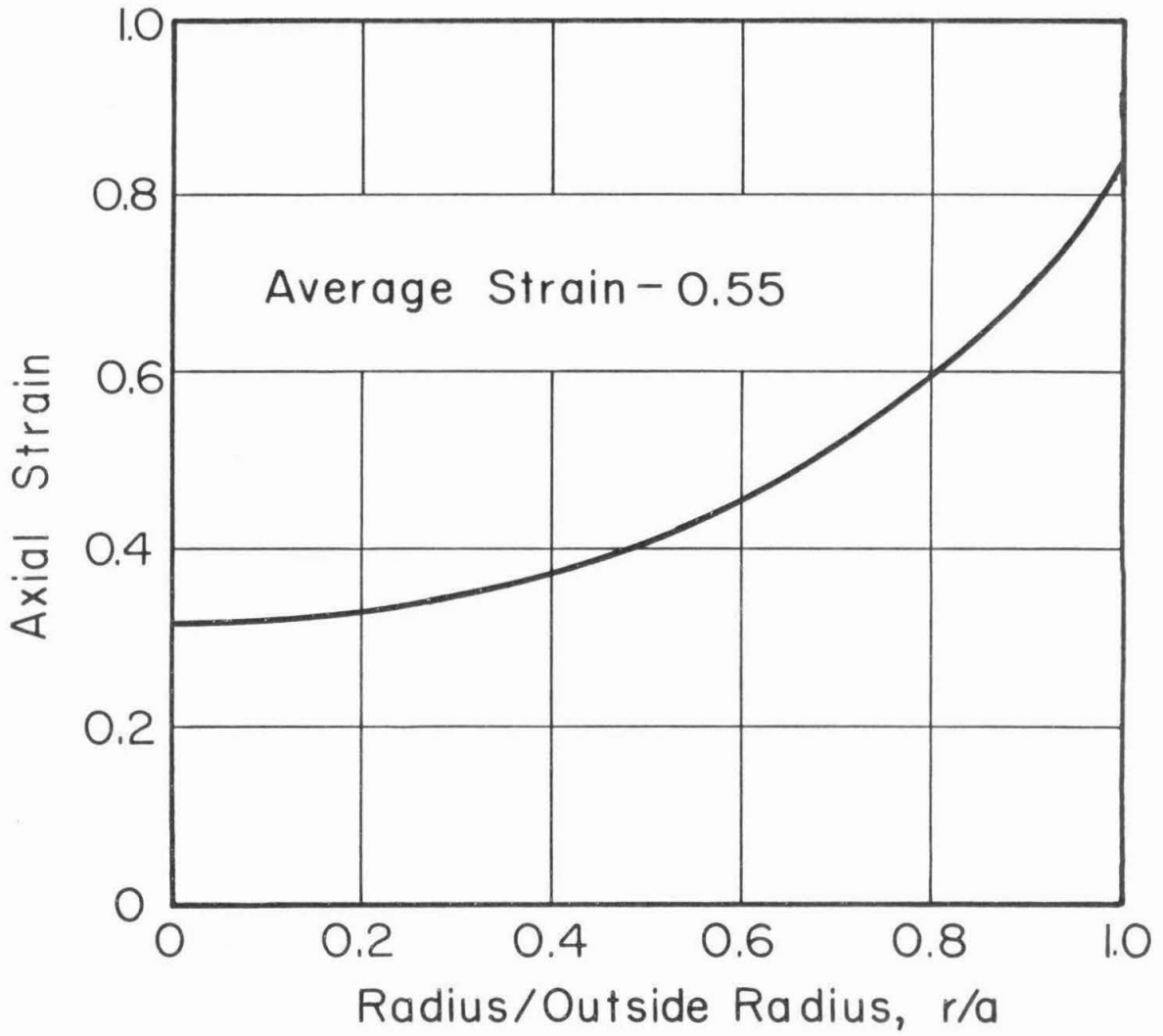


Figure 25. Theoretical Axial Strain Distribution.

14. The calculated average stress-average strain curves for both the nonlinear radial displacement (calculated in Appendix III) and the linear radial displacement (Bridgman's results) are shown in Figure 26, along with an experimentally determined curve. The calculated stresses are at the worst about six per cent smaller than the measured stresses. However, if the flow stress-strain curve that was employed in the calculations were from Group 3 rather than Group 1 (Figure 12), the calculated stresses would be about six per cent greater than the measured stresses. Thus, the agreement between the experimental and calculated average stresses is as good as the uncertainty in the flow stress will permit. The difference between the two calculated curves is insignificant.

The stress distribution as a function of radius is quite different for the two cases, however, as shown in Figure 27. Thus, two different cases which have quite different displacements, strains, and stress distributions have the same average stress-average strain curves. Therefore, agreement between the calculated and measured average stress-average strain curves does not prove that the calculation is correct. Since the nonlinear radial displacement function is based on measurement rather than assumption, the author has assumed that the stress distribution associated with the nonlinear radial displacement is the correct stress distribution. The nearly constant axial stress associated with the nonlinear radial displacement function is the result of two opposing tendencies. The hydrostatic tension is a maximum on the axis, but the flow stress is a maximum on the surface.

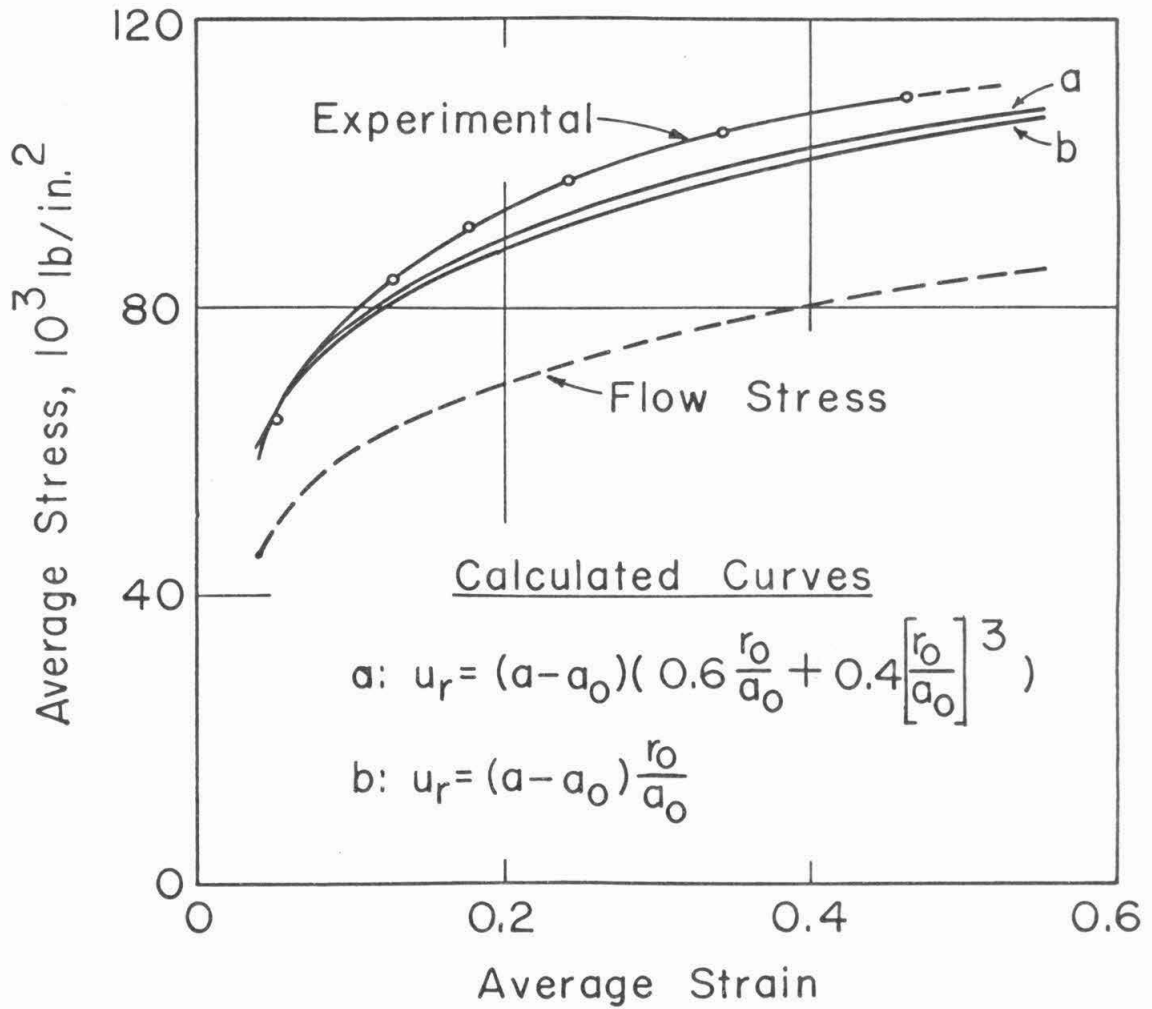


Figure 26. Average Stress vs. Average Strain for Notched Specimen at Room Temperature.

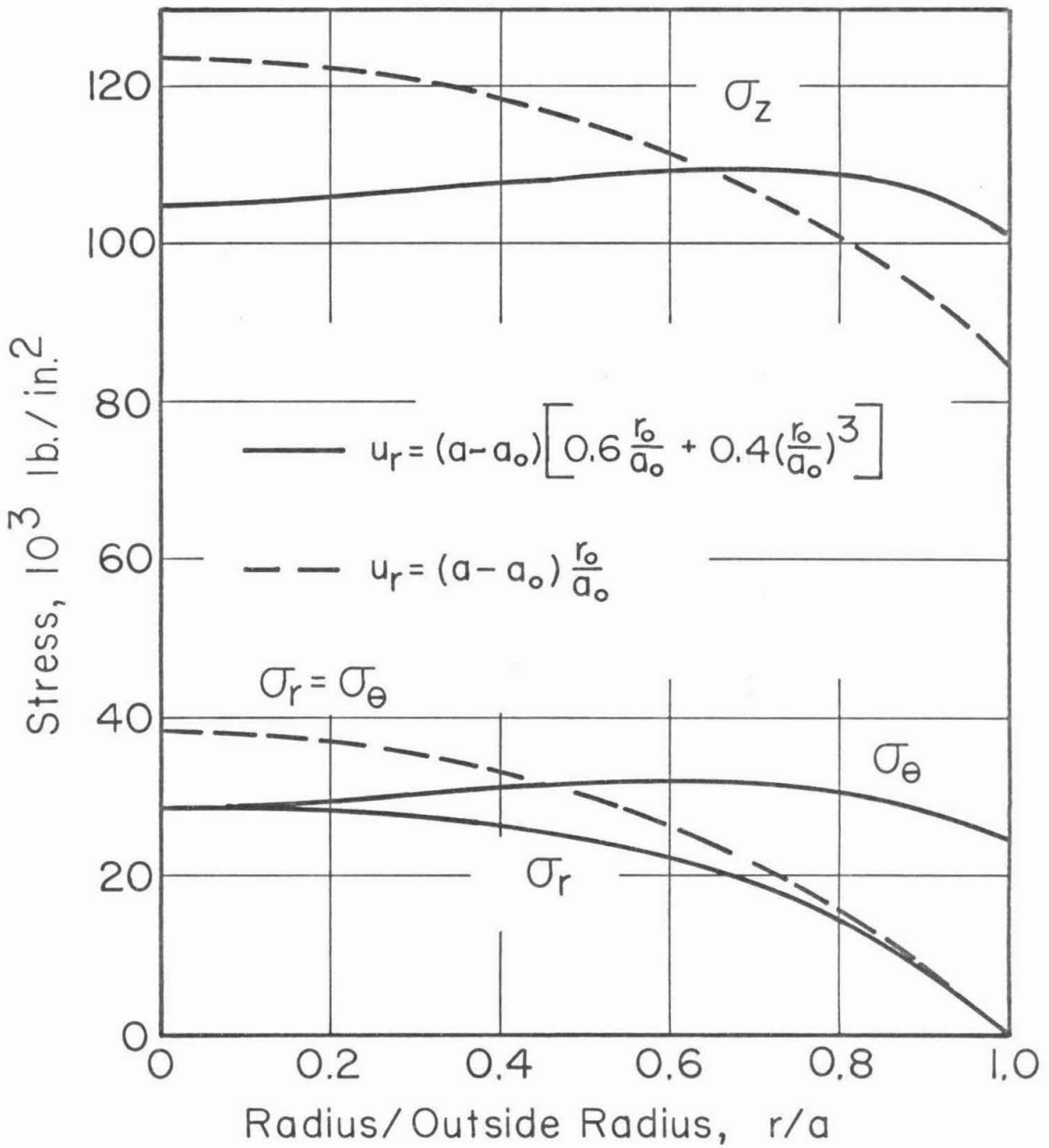


Figure 27. Comparison of Theoretical Stress Distributions for Two Radial Displacement Functions. Average Strain: 0.55.

The calculations of the maximum tensile stresses and strains at fracture were based on the assumption that the macrofracture was initiated on the specimen axis. The stress on the axis of the notched specimens was assumed to be the average stress, since Figure 27 shows that the axial stress is nearly constant. The strain on the specimen axis was assumed to be 60 per cent of the average strain, as shown in Figure 25. In summary, the maximum tensile stress and strain at which macrofracture began was calculated as follows:

Unnotched Specimens

Stress - calculated from Bridgman's results (Fig. 4)

Strain - average strain

Notched Specimens

Stress - average stress

Strain - 0.6 average strain

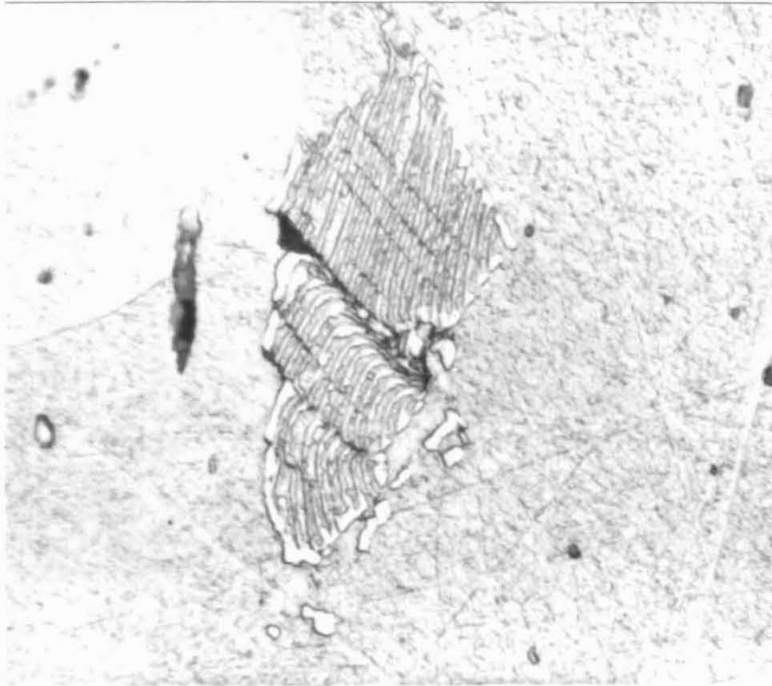
B. Mechanism of Fibrous Fracture at Room Temperature

1. Microcracks

The microcracks that were found in the specimens prior to the initiation of the macrofracture can be divided into three types:

(1) intrapearlitic, (2) interpearlitic, (3) "ox-tail".

Intrapearlitic microcracks extend across the pearlite colony, but not into the proeutectoid ferrite, as is shown in Figure 28. The intrapearlitic microcracks have three interesting characteristics: (1) the microcracks are oriented at approximately 45 degrees to the tensile axis; (2) the relative displacements across the microcracks are parallel to the microcracks; (3) there are at least six microcracks in the pearlite colony shown in Figure 28. These three characteris-



↑ Axis
↓

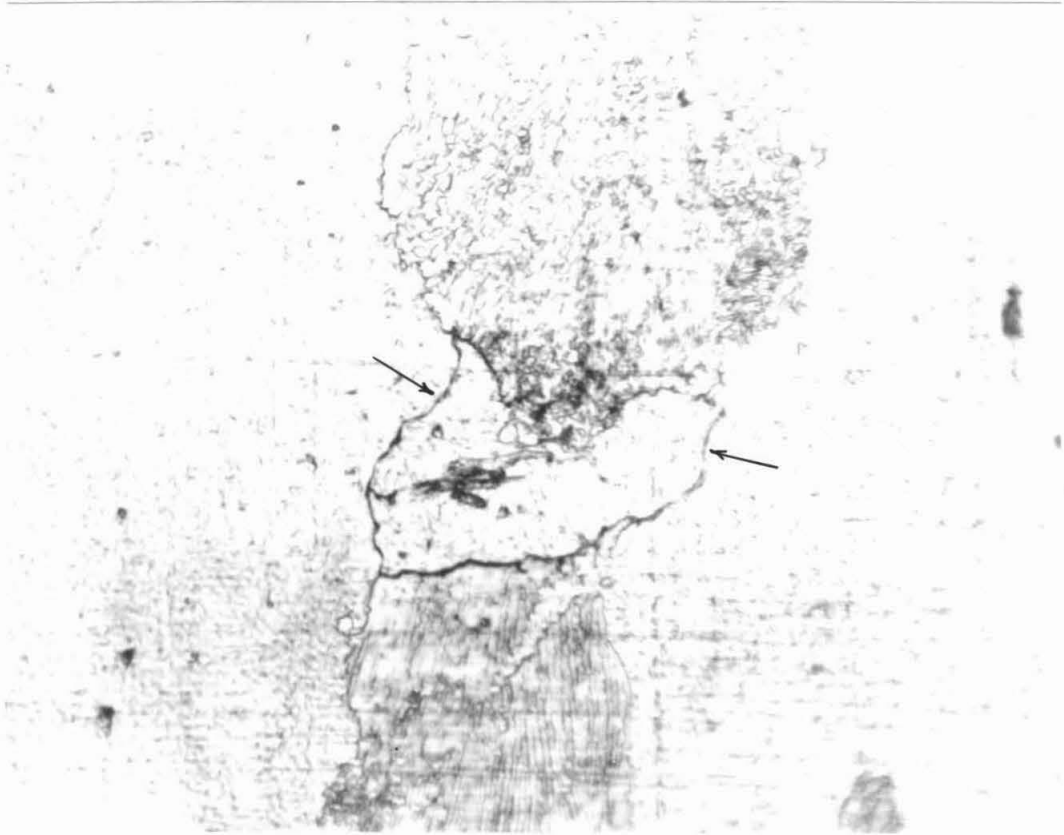
Figure 28. Intrapearlitic Microcracks, Unnotched Specimen, Average Strain 0.62, 2000X.

tics imply that the intrapearlitic microcracks are caused by shearing action, and not directly by the applied tension. Presumably slip bands in the proeutectoid ferrite are blocked by the stronger pearlite until the resulting stress concentration causes the pearlite to crack.

Interpearlitic microcracks lie in the region between two axially aligned pearlite colonies, as is shown in Figure 29. The interpearlitic microcracks apparently begin in the pearlite-proeutectoid ferrite interfaces, as the interface cracks were often seen without the accompanying axial cracks in the proeutectoid ferrite.

"Ox-tail" microcracks are associated with axial inclusion stringers. A typical "ox-tail" microcrack is shown in Figure 30. The thin, dark lines that join the inclusion particles in Figure 30 might be mistaken for the edge of one continuous inclusion that is partially covered by smeared ferrite. However, electropolishing removes the smeared layer, leaves the inclusion protruding above the polished surface, and definitely reveals the crack. The intrapearlitic and interpearlitic microcracks are much more numerous than the "ox-tail" microcracks because the steel contains many more pearlite colonies than inclusion stringers. The longest "ox-tail" cracks are several times longer than the pearlitic cracks, however.

Figure 31 shows a microcrack system which was located a short distance beyond the tip of the macrocrack in the specimen. This microcrack system is of interest because of its complexity. Some of the grain boundaries have been made extremely jagged by plastic flow. There are irregular lines that are etched similarly to grain boundaries. Presumably these lines are strong slip lines or sub boundaries. They



↑
↓ Axis

Figure 29. Interpearlitic Microcrack, Unnotched Specimen, Average Strain 0.73, 2000X.

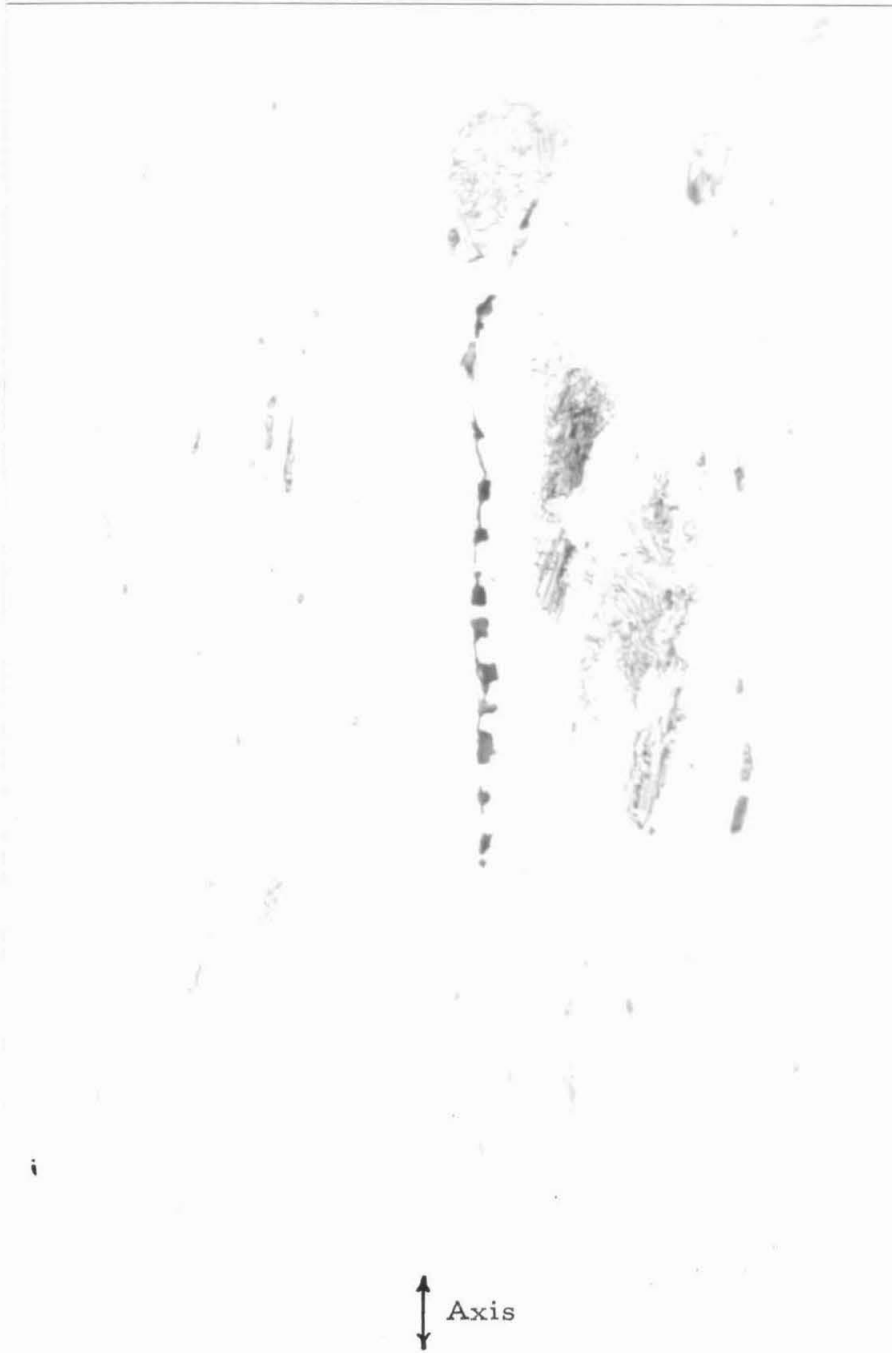
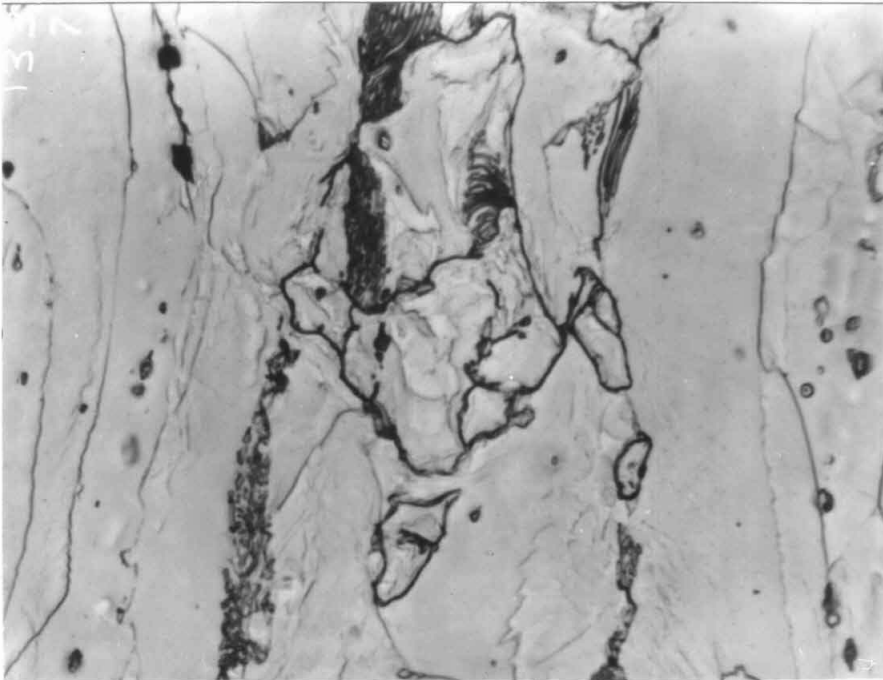


Figure 30. "Ox-Tail" Microcrack, Unnotched Specimen, Average Strain 0.73, 1500X.



↑
↓ Axis

Figure 31. Complex Microcrack in Unnotched Specimen Containing Macrocrack, 1500X.

are definitely caused by large plastic flow, as they are not present at small strains. In many places the microcracks appear to have been formed in these irregular lines. In other places the cracks are definitely in grain boundaries. The author saw such complex microcracks only in specimens that already contained a macrocrack.

Intrapearlitic microcracks were found in specimens with strains as small as 0.13. According to the data shown in Figure 21, the total length of all microcracks on the polished surface is

$$L = K\epsilon^{3.3} \quad [6]$$

where

L is the total length of microcrack per unit area of polished surface,

K is a constant,

ϵ is the average strain.

The microcrack length in the notched specimen falls on the curve for the unnotched specimens. Therefore, the increased hydrostatic tension in the notched specimen does not significantly affect the amount of microcracking. The amount of microcracking depends only upon the strain, as is shown in Equation 6. In the notched specimen, the length of microcracks is significantly greater near the surface than on the axis. This result agrees with the previously stated conclusion that in a notched specimen the strain is greater near the surface than on the axis.

Three of the unnotched specimens for which microcrack lengths are plotted in Figure 21 were Group 1 specimens (Figure 12), but the data that are plotted at the average strain of 0.80 is from a

Group 3 specimen. The strain of 0.80 is a corrected average strain that was obtained by multiplying the actual average strain by the ratio

$$C = \frac{\text{strain at final fracture for Group 1 specimens}}{\text{strain at final fracture for Group 3 specimens}} \cdot \quad [7]$$

The numerical value of C was calculated from the data given in Table I. Figure 21 shows that the correction of Equation 7 makes the microcrack lengths for Group 1 and Group 3 specimens fall on the same curve. Although the average strain at final fracture is less for Group 3 specimens, the total microcrack length at final fracture is the same for Group 1 and Group 3 specimens. This result suggests that there may be a critical total microcrack length at which final fracture occurs. The concept of a critical total microcrack length for final fracture breaks down completely when notched specimens are considered. The microcrack length at final fracture in the notched specimens is less than 10 per cent of that in unnotched specimens.

Prior to the initiation of the macrofracture, the number of microcracks increases with increased strain, but each microcrack remains confined to a small region associated with a microstructural feature, as shown in Figures 28, 29, and 30. The author is convinced that at the initiation of the macrofracture the specimens do not contain voids that are large enough to be visible in the optical microscope. All of the many microcracks are fine cracks, such as those shown in Figures 28, 29, 30, and 31. (The fine cracks may consist of sheets of very small voids that have been smeared out by straining (20), but this is on a much smaller scale than is considered in this thesis.) Thus, the fibrous fracture of mild steel does not develop

by the gradual growth of voids, as Rogers (17) and Puttick (18) observed in copper. Prior to the initiation of the macrofracture, all of the microcracks are fine cracks which are confined to a particular microstructural feature. Therefore, the critical event in the initiation of the macrofracture must be the spreading of a microcrack beyond the microstructural feature with which it is associated.

2. Macrofractures

The unnotched specimen in which the macrofracture was filled with epoxy resin by the procedure described in II. B. 2(b) is shown in Figures 32-45. The merit of filling the macrofracture with epoxy resin is clearly shown in Figure 33. The two separate, thin, dark regions oriented in the axial direction are both filled with resin, and, therefore, must be part of the macrofracture. If the resin were not present, the author would have concluded that these fissures were the remnants of axial inclusions that had been pulled out during polishing. (For convenience, the different parts of the macrofracture will be referred to as separate cracks where this seems reasonable, although they are all connected together.) The axial crack shown in Figure 33 has missing portions which appear in Figure 34. The crack is not straight enough to be completely exposed on one polished surface. By studying the series of photographs in Figures 32-45, one can obtain an approximate three-dimensional mental picture of the macrofracture.

The presence of axial cracks is the most interesting feature that appears in Figures 32-45. The axial crack that appears in Figures 43 and 44 is 0.08 in. long, which is 25 per cent greater than the

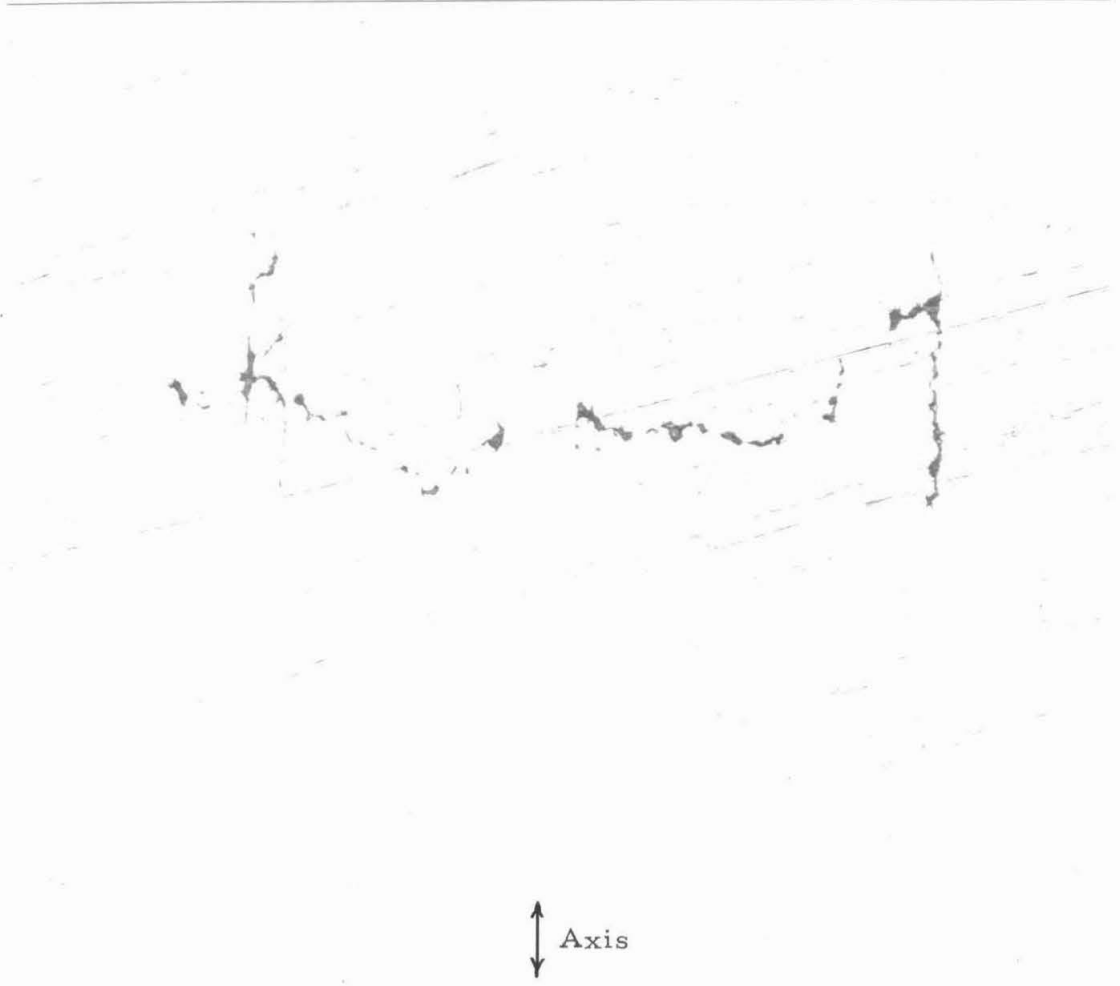


Figure 32. Macrofracture Filled with Resin in Unnotched Specimen, Surface 0.022 In. from Axis; Ground on 600 Paper, 100X.



↑ Axis
↓

Figure 33. Macrofracture Filled with Resin in Unnotched Specimen, Surface 0.014 In. from Axis, Ground on 600 Paper, 100X.



Figure 34. Macrofracture Filled with Resin in Unnotched Specimen, Surface 0.012 In. from Axis, Ground on 600 Paper, 100X.



←→ Axis

Figure 35. Macrofracture Filled with Resin in Unnotched Specimen, Surface 0.008 In. from Axis, Mechanically Polished, Etched in 5 Per Cent Nital, 100X.



↔ Axis

Figure 36. Macrofracture Filled with Resin in Unnotched Specimen, Surface 0.005 In. from Axis, Electropolished, 100X.



↔ Axis

Figure 37. Macrofracture Filled with Resin in Unnotched Specimen, Surface 0.003 In. from Axis, Electropolished, 100X.



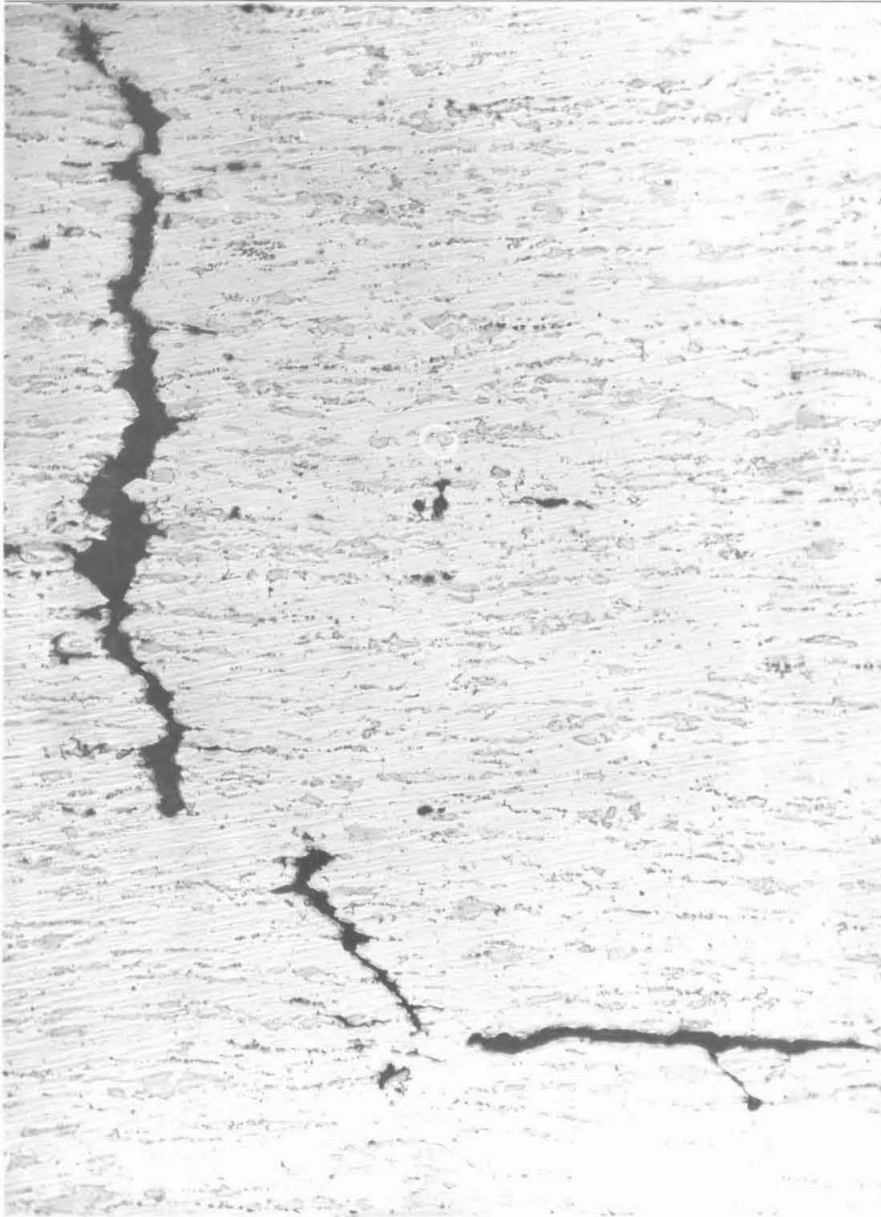
←→ Axis

Figure 38. Macrofracture Filled with Resin in Unnotched Specimen, Surface on Axis, Electropolished, 100X.



↔ Axis

Figure 39. Macrofracture Filled with Resin in Unnotched Specimen, Surface 0.003 In. Beyond Axis, Electropolished, 100X.



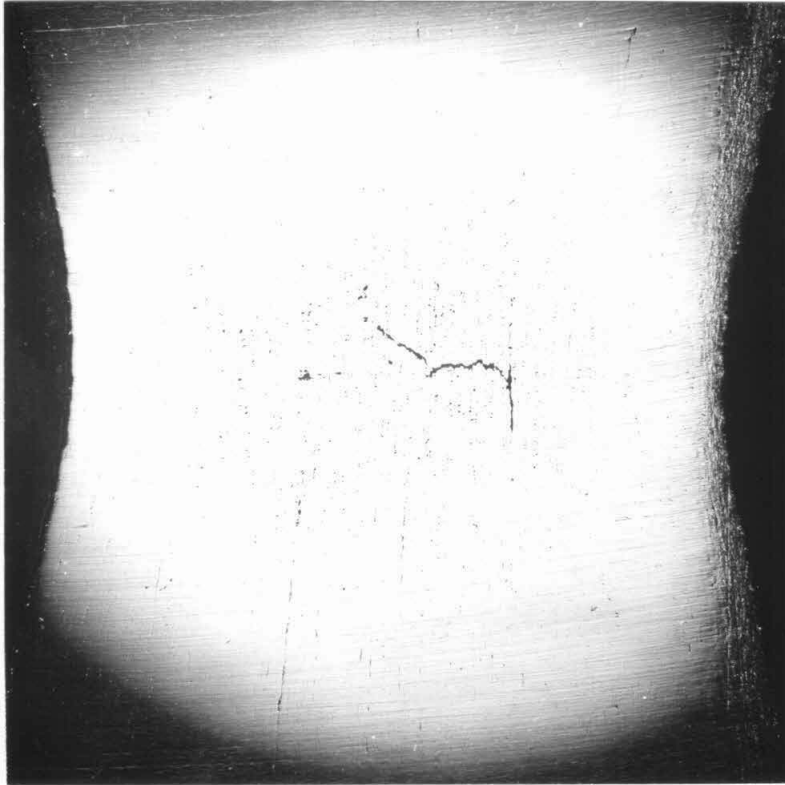
↔ Axis

Figure 40. Macrofracture Filled with Resin in Unnotched Specimen, Surface 0.005 In. Beyond Axis, Electropolished, 100X.



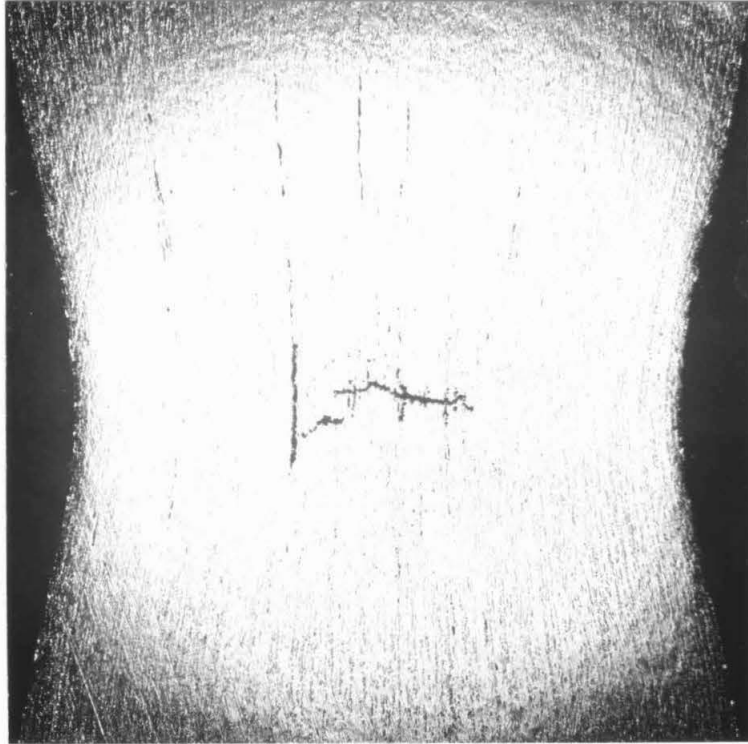
↔ Axis

Figure 41. Macrofracture Filled with Resin in Unnotched Specimen, Surface 0.007 In. Beyond Axis, Electropolished, 100X.



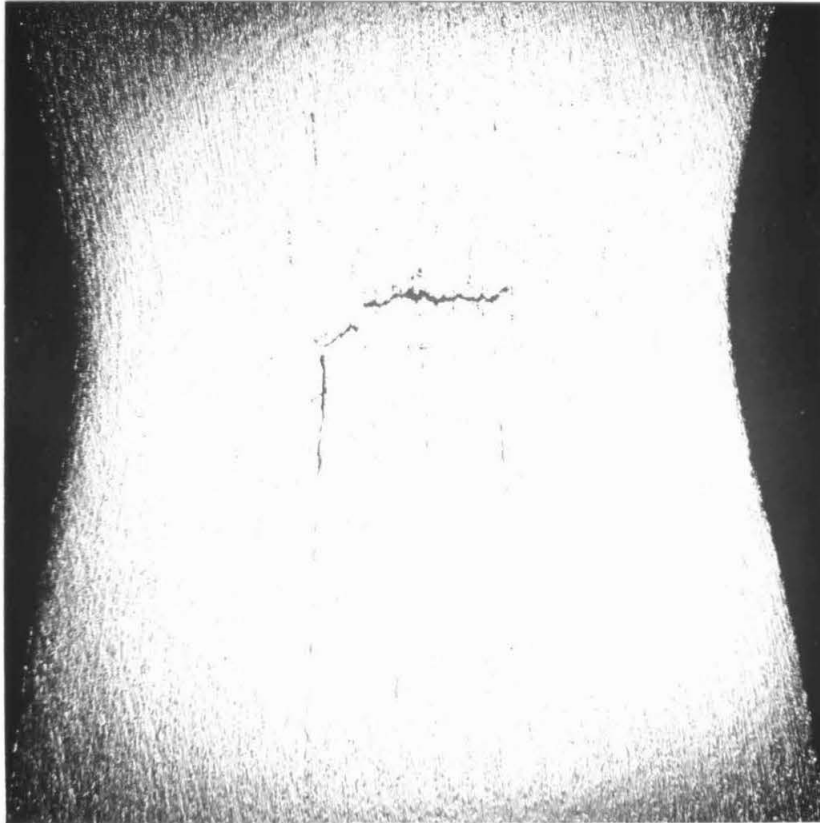
↑
↓
Axis

Figure 42. Macrofracture Filled with Resin in Unnotched Specimen, Surface on Axis (Surface Mechanically Polished After Figure 38), 15X.



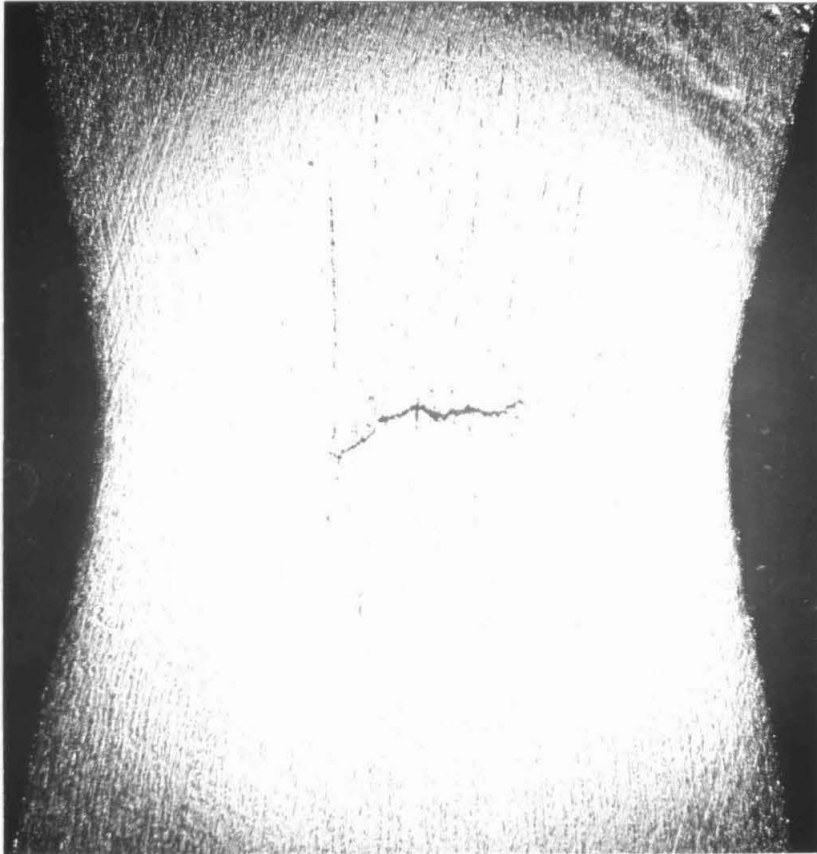
↑
↓ Axis

Figure 43. Macrofracture Filled with Resin in Unnotched Specimen, Surface 0.003 In. Beyond Axis (Same Surface as Figure 39), Electropolished, 15X.



↑
↓ Axis

Figure 44. Macrofracture Filled with Resin in Unnotched Specimen, Surface 0.005 In. Beyond Axis (Same Surface as Figure 40), Electropolished, 15X.

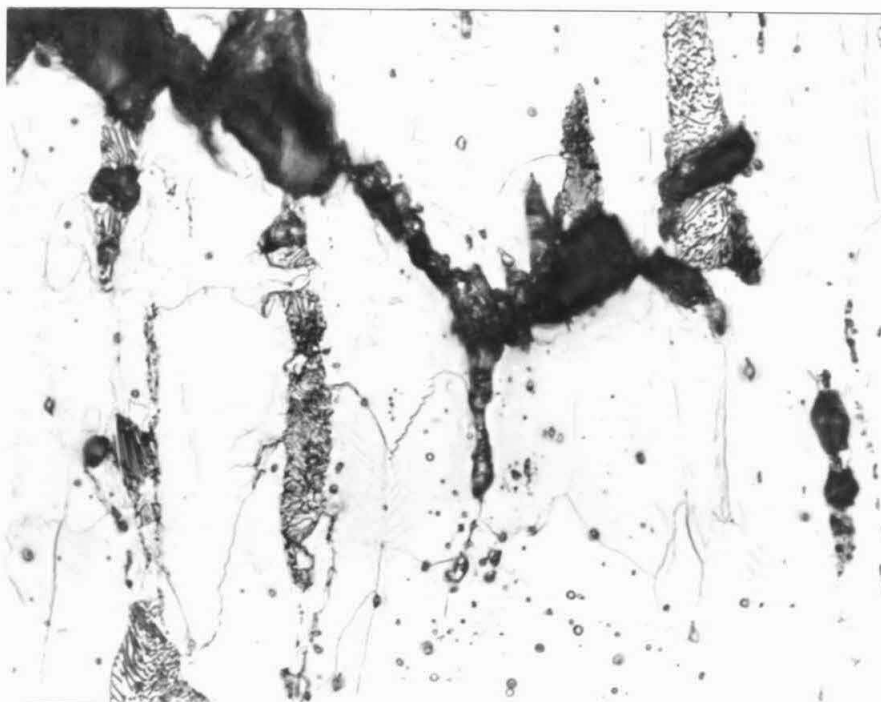


↑
↓ Axis

Figure 45. Macrofracture Filled with Resin in Unnotched Specimen, Surface 0.007 In. Beyond Axis (Same Surface as Figure 41), Electropolished, 15X.

maximum length of the transverse crack. The maximum length of the transverse crack is approximately 30 per cent of the specimen diameter. The axial crack in Figures 43 and 44 is associated with an axial inclusion stringer. The broad, dark, axial line in Figure 43 is epoxy resin, but the lighter line extending beyond the resin consists of inclusions with associated microcracks. Not all axial cracks are associated with inclusion stringers. The author observed several short, axial cracks lying in grain boundaries, such as the one that is shown in Figure 46.

The macrofracture in the unnotched specimen that is shown in Figures 32-45 is qualitatively quite different from the macrofracture in the notched specimen that is shown in Figure 47. In some regions the notched specimen has as many as eight fine cracks lying approximately parallel to each other. The unnotched specimen has only one transverse crack, and it is opened to a width of approximately 0.001 in. This result indicates that the macrofractures in notched and unnotched specimens may have characteristic differences in appearance. However, the notched specimen that is shown in Figure 48 has only one transverse crack, and it is opened to a width of approximately 0.010 in. The cracks that extend at 45 degrees from the ends of the transverse crack do contain regions where several fine cracks lie approximately parallel to each other. The specimen in Figure 48 was sectioned before the epoxy-resin filling technique had been developed. Therefore, it is impossible to determine the detailed configuration that the macrofracture had before the specimen was sectioned and polished. An examination of more macrofractures that



↑ Axis
↓

Figure 46. Macrofracture Filled with Resin in Unnotched Specimen, Axial Macrocrack Lying in Grain Boundary, 750X.

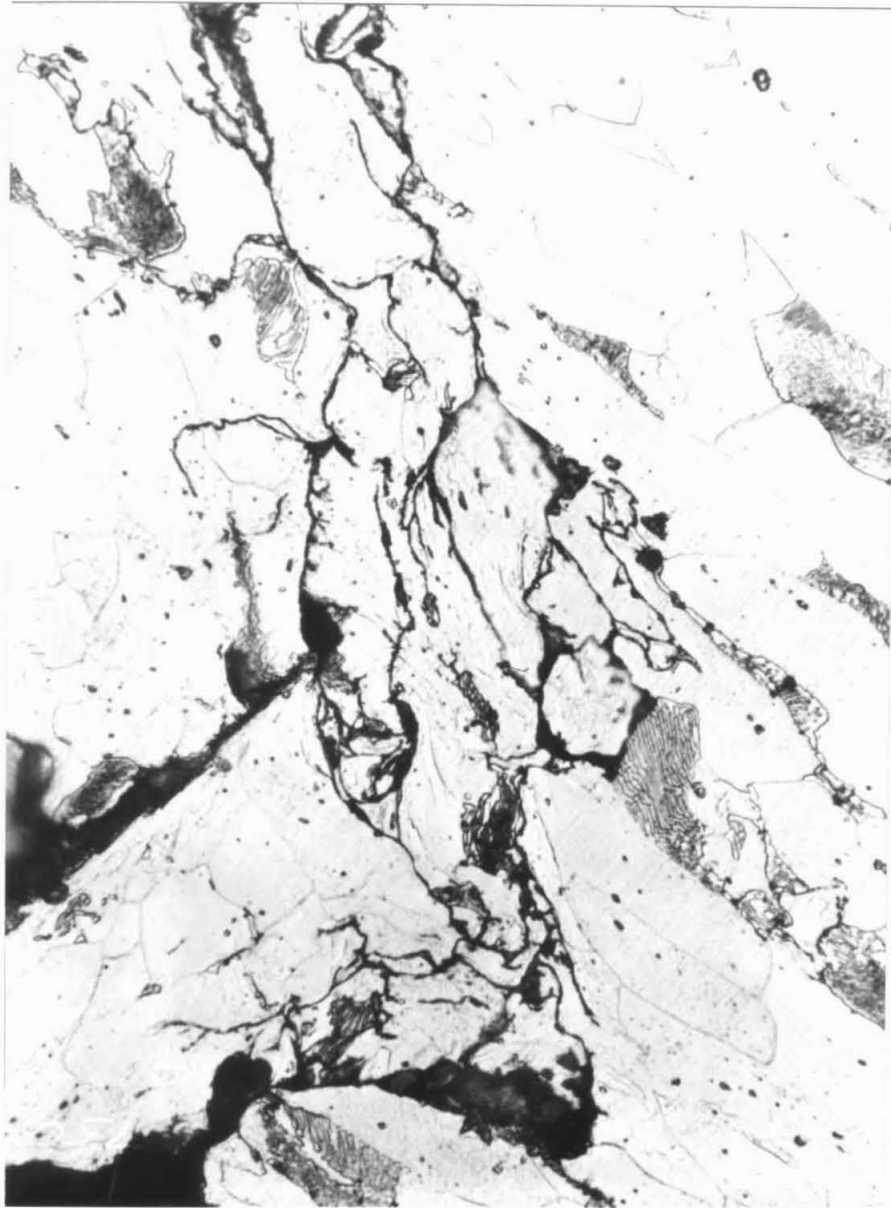


Figure 47. Fine Cracks in Macrofracture of Notched Specimen (Same as Figure 23), 750X.

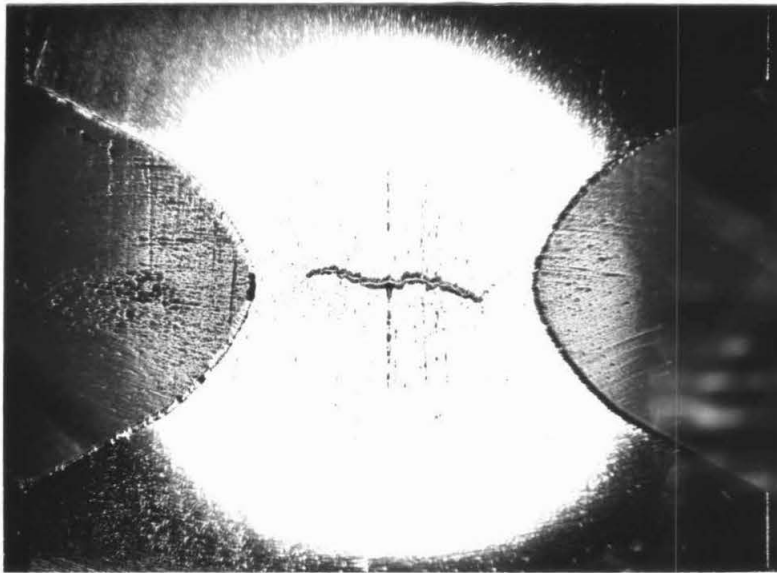


Figure 48. Macrofracture in Notched Specimen,
6.3X.

have been filled with epoxy resin will be required before any characteristic differences in the appearance of the macrofracture in notched and unnotched specimens can be verified.

Figures 32-45 provide some clues to the mechanism of macrofracture development. The axial crack shown in Figures 43 and 44 probably developed when the microcrack associated with the inclusion stringer was able to propagate beyond the inclusions. The two long axial macrocracks that appear in Figures 42, 43, and 44 lie at the edge of the transverse macrocrack, but extend both above and below the transverse macrocrack. This geometry suggests that the axial cracks were present first, and either stopped the transverse crack or served as a source for the transverse crack. The mechanism by which an axial crack could lead to the initiation of the transverse crack is suggested by the lower right hand corner of Figure 40. The segment of macrocrack extending at a 45-degree angle from the axial crack is very similar in appearance to the region at the lower center of the photograph where the transverse crack joins the axial crack. In the region at the lower right of Figure 40, two or more microcracks that are associated with pearlite colonies appear to have joined to form the segment extending from the axial crack. This geometry suggests the following mechanism for the initiation of the transverse crack. First, an axial macrocrack is formed. Then a microcrack associated with a nearby pearlite colony is able to propagate through the narrow band of proeutectoid ferrite which separates the pearlite colony from the axial macrocrack. Because of the increased stress concentration, this crack is then able to propagate through the proeutectoid ferrite to

join with a microcrack in a neighboring pearlite colony. The crack continues to propagate in this step-by-step manner to form the transverse macrocrack. The microcracks that are associated with the pearlite colonies may open up before propagating. The resulting strain concentration then causes the crack to propagate through the proeutectoid ferrite. Microcracks that have opened, but which are not yet joined together on the polished surface, are shown at the tip of the macrocrack at the left side of Figure 49. Although the two fractures that are associated with the pearlite colonies are not joined in the polishing plane, the presence of the epoxy resin proves that they are joined somewhere out of the polishing plane.

A possible alternative mechanism for the initiation of macrofracture is the cooperative growth of axial and transverse macrocracks. The cooperative formation of axial and transverse cracks is suggested by the crack that is shown slightly below the center of Figure 50. The mechanism could be the one that is shown in Figure 51.

C. Stresses and Strains at Fracture

The values of the maximum tensile stress and strain at fracture are plotted in Figure 52. The data plotted are from specimens pulled to final fracture in the tensile testing machine at temperatures ranging from room temperature to liquid nitrogen temperature. The data for unnotched specimens are from Group 1 (Figure 12) specimens only. The dashed curve represents the path followed in reaching the two data points which terminate the curve. The solid curves, which are drawn through the data, are tensile fracture loci. The initiation of the macrofracture is very quickly followed by final frac-

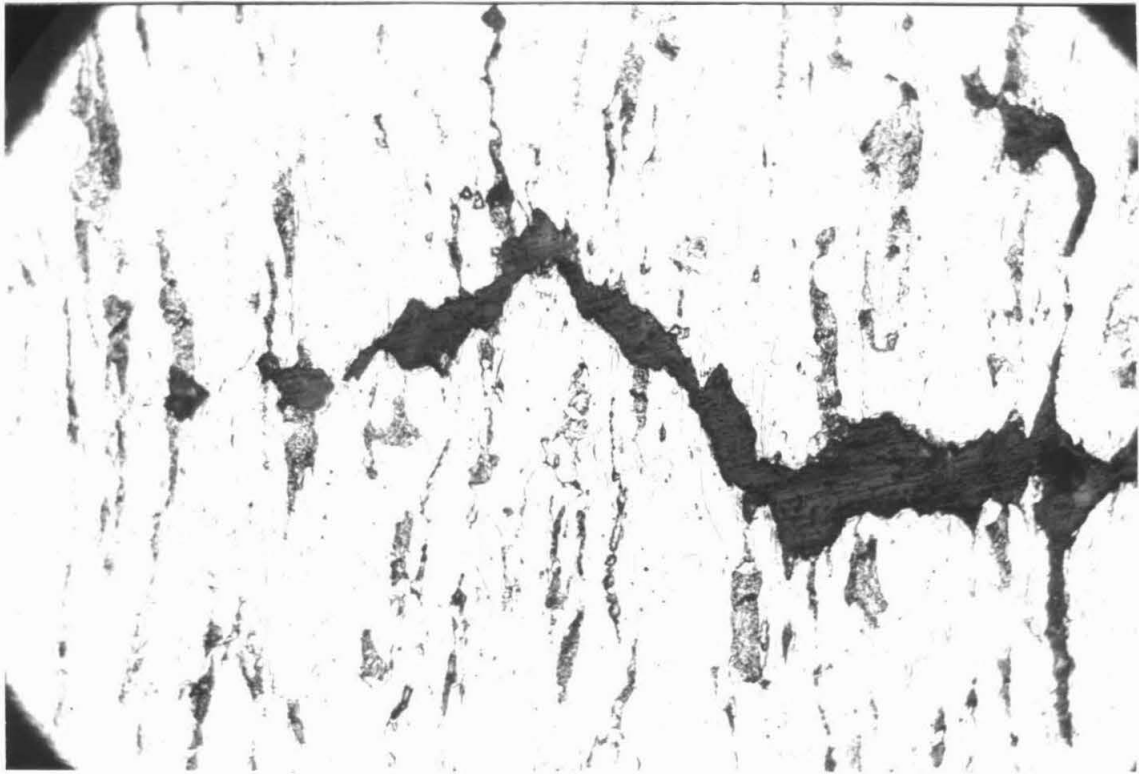
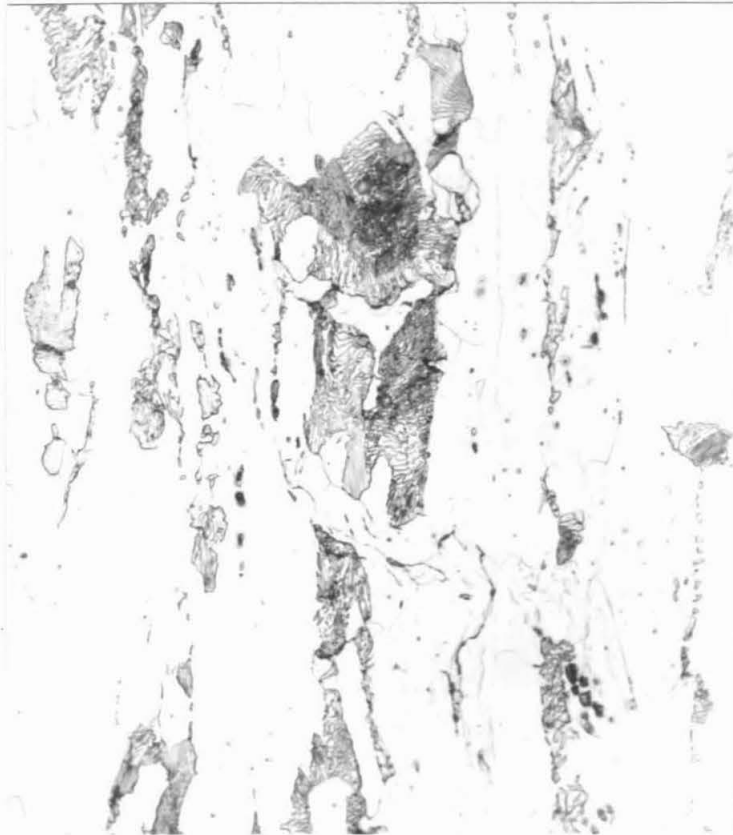


Figure 49. Intermittent Macrofracture, Macrofracture Filled with Resin in Unnotched Specimen, 250X.



↑ Axis

Figure 50. Microcrack Starting to Spread, Unnotched Specimen Containing Macrocrack, 500X.

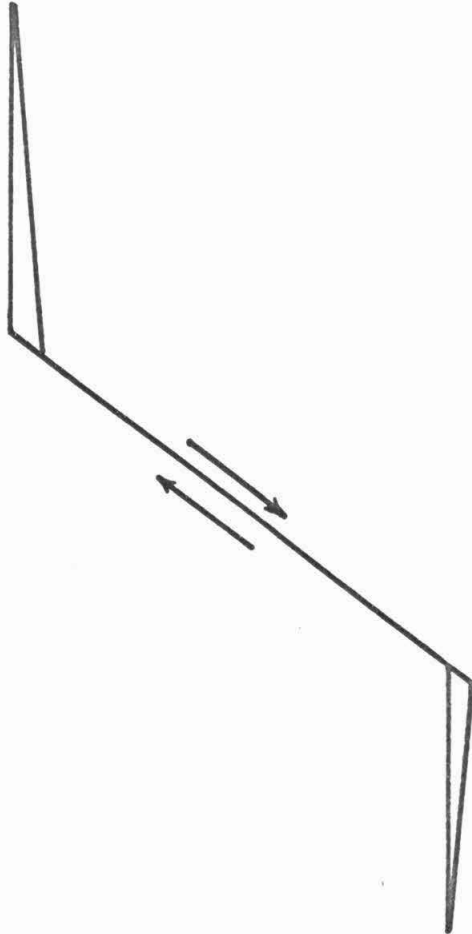


Figure 51. Possible Mechanism of Macrofracture Initiation.

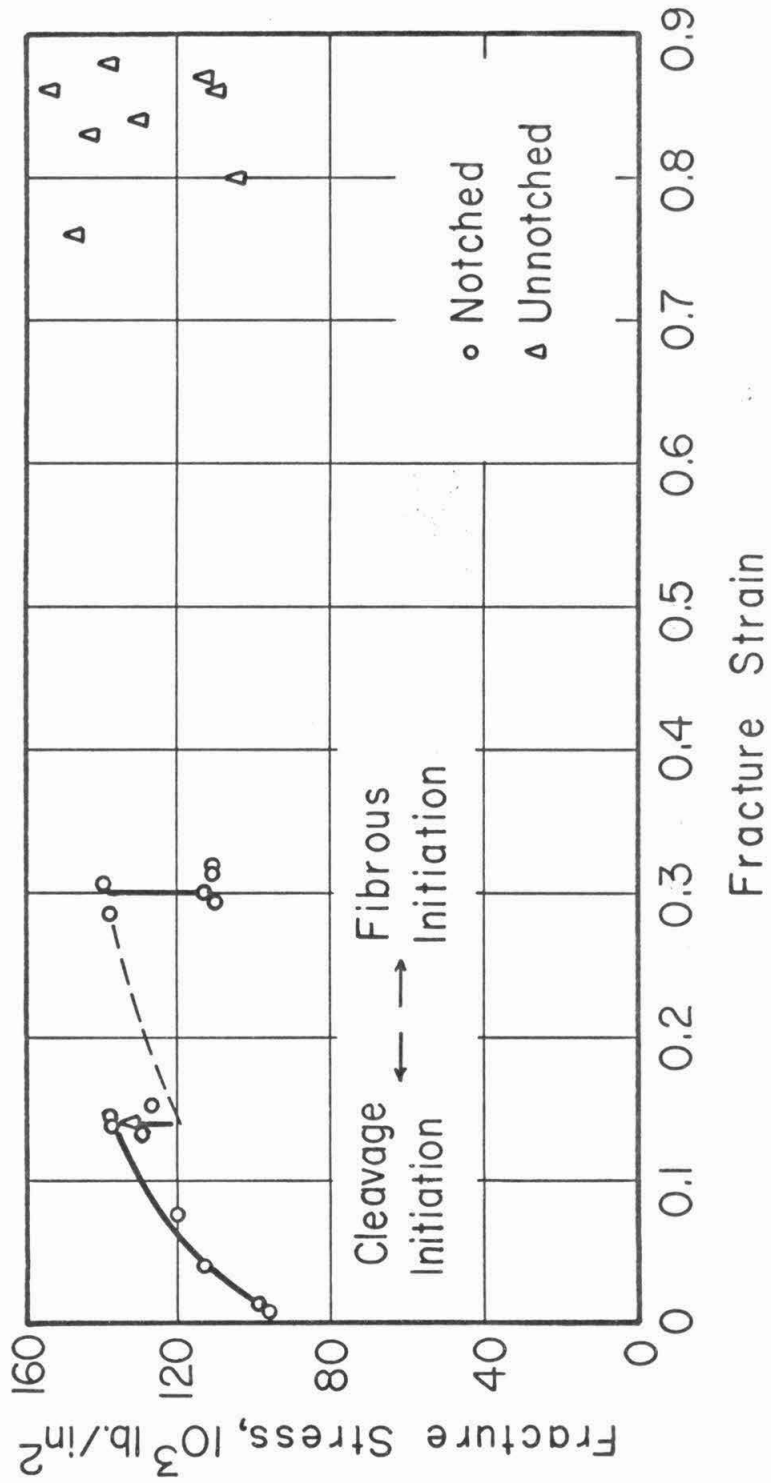


Figure 52. Stress and Strain at Fracture.

ture in tests that are conducted in the tensile testing machine. Therefore, the data plotted in Figure 52 are the maximum tensile stresses and strains at which the macrofracture is initiated.

Figure 52 shows that the stresses for the initiation of cleavage and fibrous macrofractures are approximately the same. The smallest stress for the initiation of both cleavage and fibrous macrofractures is approximately 100,000 lb./in.². The smallest strain shown in Figure 52 is several times the elastic strains in the specimen, and the plastic zone extended completely across the specimen, i. e., general yielding had occurred. Hendrickson, Wood, and Clark (21) found that in the same steel the cleavage fracture stress was 210,000 lb./in.² when the plastic strains were comparable to the elastic strains, and the plastic zone was restricted to an enclave near the notch root, i. e., when general yielding had not occurred. Thus, the occurrence of general yielding causes the cleavage fracture stress to decrease by a factor of approximately two. In the following two sections the stresses and strains at which cleavage and fibrous macrofractures are initiated are discussed in greater detail.

1. Cleavage Fracture

Each of the six points on the solid curve at the left of Figure 52 represents the stress-strain values at the center of a notched specimen at the time of cleavage fracture. The solid curve is the cleavage fracture locus for strains less than 0.13. Each of the six points is the terminus of a stress-strain path that was followed in reaching that point. The stress-strain path represents the values of stress and strain at the center of the specimen during the progress

of the tensile test. An isothermal stress-strain path is a path that results when the entire tensile test is conducted at one temperature.

The stress-strain path may approach its terminus in one of two different ways, as is shown in Figure 53. The approach path b results when the specimen is flowing plastically at the time of fracture. The approach path c results when the specimen is behaving elastically at the time of fracture. The author believes that the two different approach paths will result in two different fracture loci, as is shown in Figure 54. For simplicity, the loci are called the plastic cleavage fracture locus or the elastic cleavage fracture locus, depending upon the type of stress-strain path followed in approaching the locus. Cleavage fracture can occur at any point, such as c in Figure 54, within the region between the two fracture loci. A specimen in which the stress-strain path is b will not fracture while behaving elastically because the stress is below the elastic cleavage fracture locus. Cleavage fracture will occur when plastic flow begins, because the stress is above the plastic cleavage fracture locus.

The solid curve at the left of Figure 52 is the plastic cleavage fracture locus. The stress on the elastic cleavage fracture locus is 210,000 lb./in.² at zero strain, as determined by Hendrickson, Wood, and Clark (21). The author is unaware of any determination of an elastic cleavage fracture locus at strains larger than zero.

The determination of the plastic cleavage fracture locus involved two problems. (1) Points such as c in Figure 54 must not be mistaken for a point on the plastic cleavage fracture locus. The stress on the plastic cleavage fracture locus is the minimum stress

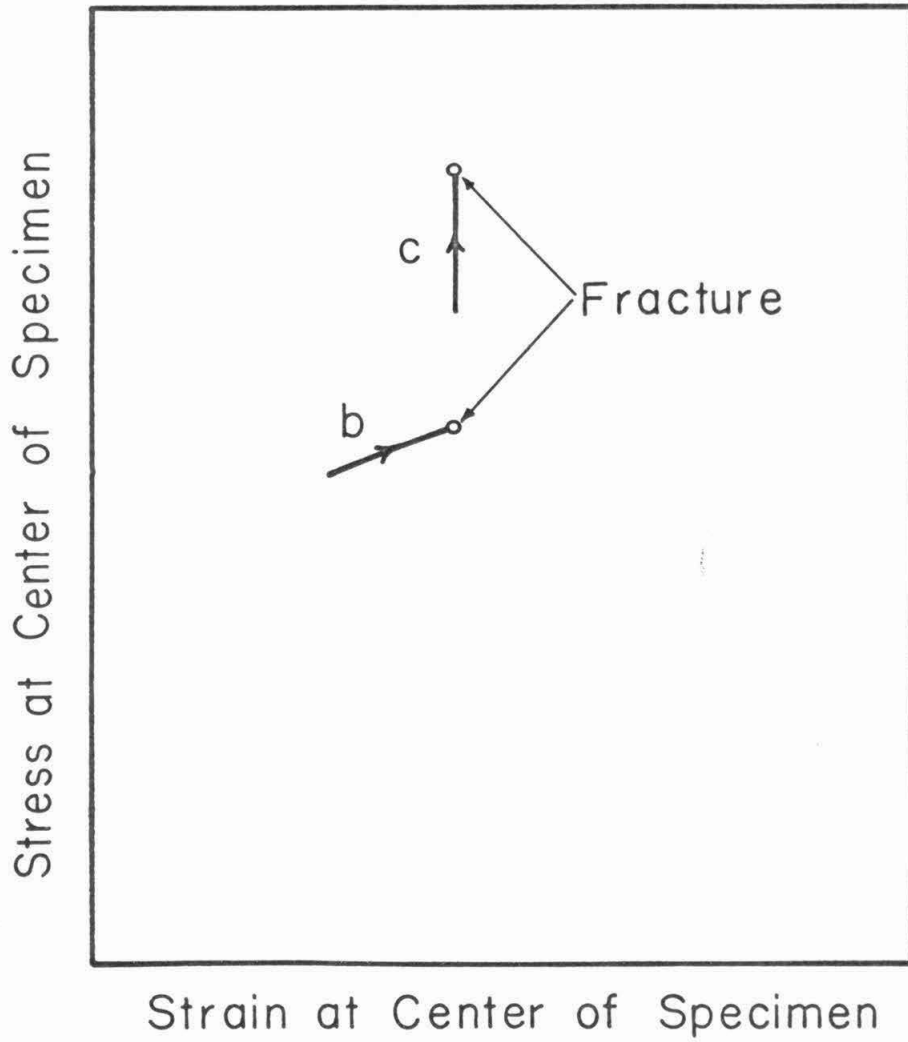


Figure 53. Two Types of Paths for Approaching the Stress-Strain Value at Which Cleavage Fracture Occurs.

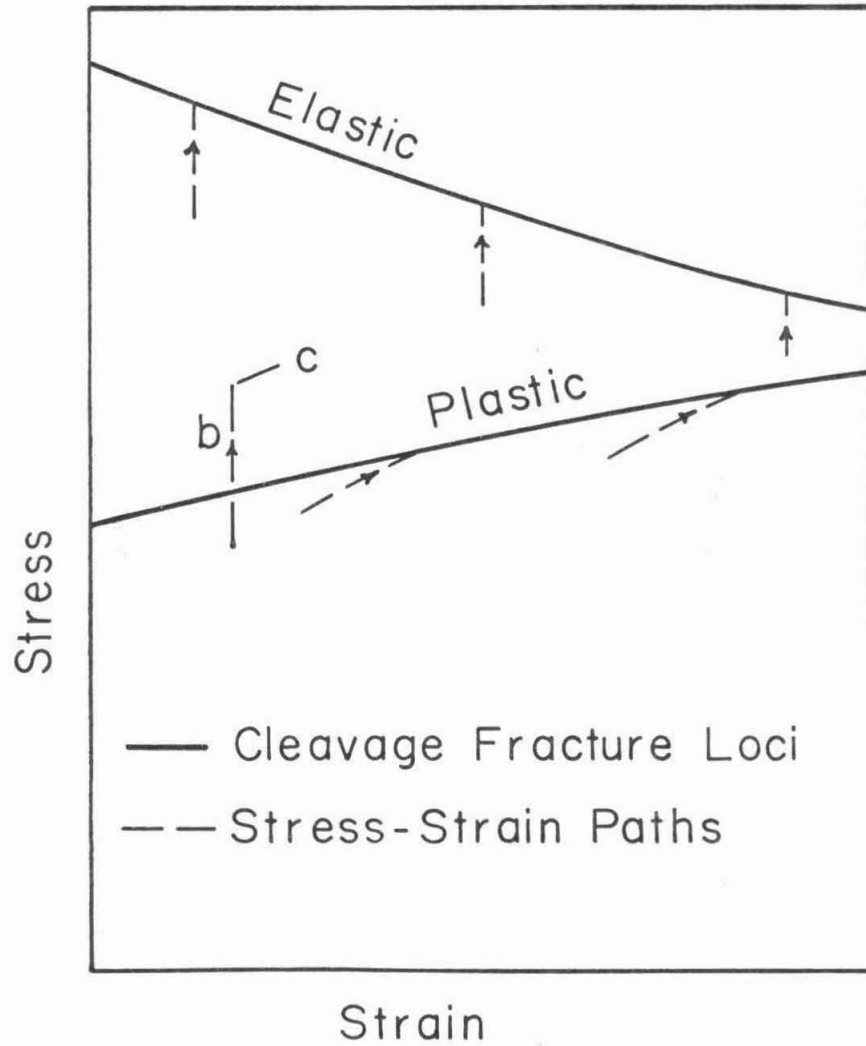


Figure 54. Hypothetical Stress-Strain Loci for Cleavage Fracture.

for fracture at the same strain. Fracture must be proven not to occur during plastic straining in the stress-strain region immediately below the plastic cleavage fracture locus. (2) The stress-strain paths followed should have larger slope than the plastic cleavage fracture locus. Otherwise, plastic cleavage fracture will occur only at zero strain. The plastic cleavage fracture locus that is drawn through the six points at the left of Figure 52 nearly coincides with an isothermal stress-strain path. Therefore, isothermal tests are not satisfactory for determining the plastic cleavage fracture locus.

Nonisothermal tensile tests are the solution to both of the above problems. Figure 55 shows the nonisothermal stress-strain paths that were followed to obtain three of the data points that are shown in Figure 52. Each step increase in the stress corresponds to a step decrease in the temperature. The nonisothermal stress-strain paths serve three purposes: (1) cleavage fracture occurs at different strains; (2) fractures are proven not to occur during plastic straining in the stress-strain region immediately below the plastic cleavage fracture locus; (3) the stress-strain values at fracture are shown to lie on a unique locus, independent of the stress-strain path followed. Thus, by following nonisothermal stress-strain paths, the plastic cleavage fracture locus was determined.

The two data points which terminate the dashed curve in Figure 52 were obtained from specimens which appeared to the naked eye to have cleavage fractures. However, microscopic examination revealed small patches of fibrous fracture near the axes. The macrofracture, which was initiated in the fibrous patches, quickly converted

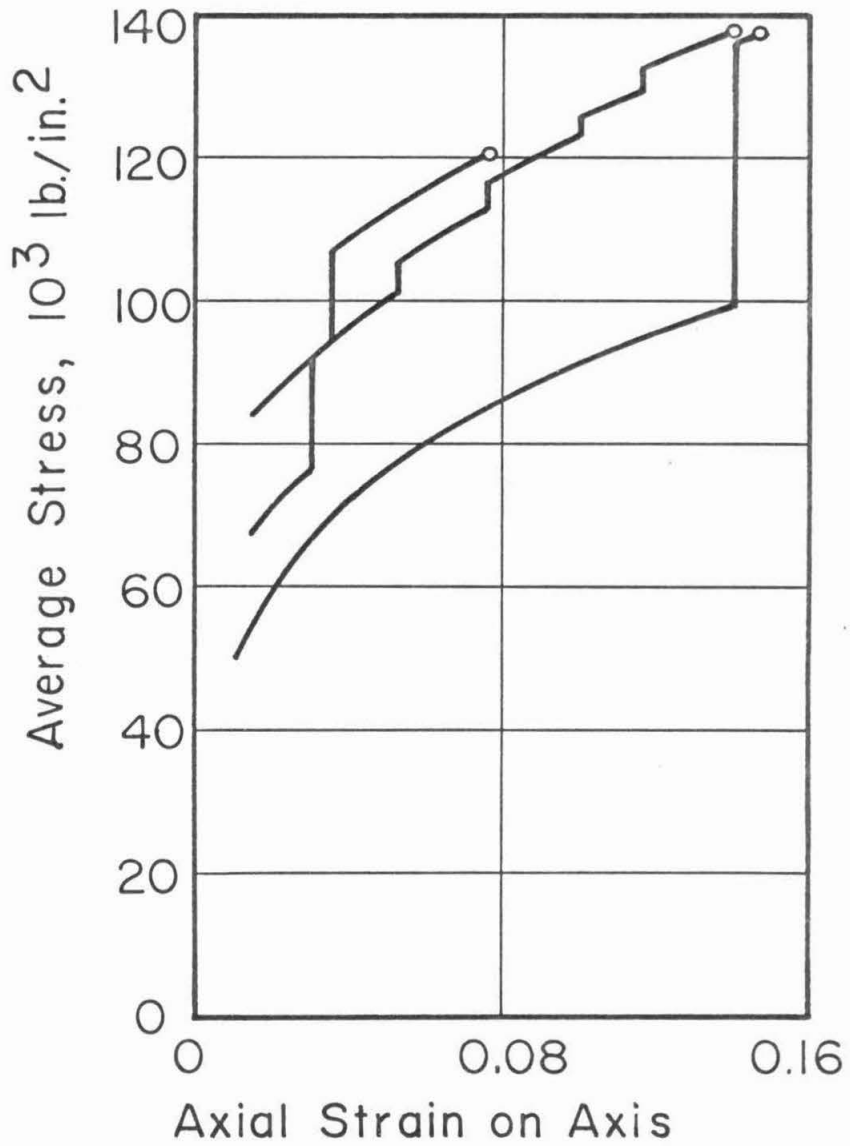


Figure 55. Three of the Nonisothermal Stress-Strain Paths that Resulted in Cleavage Fracture.

to cleavage fracture because the stress was nearly equal to that required for cleavage initiation. Also, the specimens with stress-strain paths just above the dashed curve fractured with cleavage fracture at a strain of 0.13. Thus, the stresses for cleavage fracture at strains of both 0.13 and 0.30 are slightly larger than the stresses on the dashed curve. Therefore, a curve just above the dashed curve must be the continuation of the cleavage fracture locus. Thus, the cleavage fracture locus is determined for strains less than 0.3.

A peculiar feature of the cleavage fracture locus is the decrease in cleavage fracture stress at the strain of 0.13. In specimens that were pulled at room temperature, microcracks were first observed at a strain of 0.13. Thus, the decrease in cleavage fracture stress at the strain of 0.13 may be the difference between the stress required to initiate microcracks and the stress required to propagate microcracks.

The decrease of the cleavage fracture stress by a factor of two at the onset of general yielding is probably due to the increased number of mobile dislocations. The increased number of mobile dislocations results in longer dislocation pileups. The longer dislocation pileups cause a greater stress concentration, thus reducing the applied stress required to initiate cleavage fracture at the tip of the pileup.

Figure 52 shows that with the exception of the discontinuity at the strain of 0.13, the cleavage fracture stress increases with increasing strain. Either one or a combination of both of two mechan-

isms may account for this result. (1) Increasing the strain increases the density of forest dislocations. The increased density of forest dislocations increases the applied stress which is necessary to push additional dislocations into pileups, thus increasing the applied stress necessary to initiate cleavage fracture at the tip of a pileup. (2) The increased density of forest dislocations increases the number and magnitude of cleavage steps upon the cleavage surface. The increased number and magnitude of cleavage steps increases the energy necessary to propagate the cleavage crack, thus increasing the cleavage fracture stress.

2. Fibrous Fracture

All specimens with the same geometry fractured in a fibrous manner at approximately the same strain, independent of the stress, as is shown in Figure 52. (At the same strain, the stress increased as the temperature was decreased.) This result does not agree with Ludwik's hypothesis, as there is clearly not an unique maximum tensile stress-strain curve for fibrous fracture. Apparently fibrous fractures are propagated by plastic flow. As the temperature is decreased, the plastic strain velocities necessary to create the fibrous fracture remain the same, but the stress required to obtain these velocities is increased. Since temperature has such a simple effect, the remainder of this discussion is restricted to fibrous fracture at room temperature.

At room temperature, both the notched and unnotched specimens fibrously fractured when the maximum tensile stress was approximately 110,000 lb./in.². Since their plastic constraint is much

greater, the notched specimens achieve the stress of 110,000 lb./in.² at a much smaller value of strain. Thus, the proper criterion for fibrous fracture may be that fibrous fracture occurs when the maximum tensile stress reaches a critical value that is independent of strain. An alternative fibrous fracture criterion is suggested by the mechanism of fibrous macrofracture formation. If the macrofracture is initiated by an axial crack, the greater radial tensile stress may be the cause of the fracture of the notched specimens at a smaller value of strain than in the unnotched specimens. The radial stress at fibrous fracture is 30,000 lb./in.² in the notched specimens, and 20,000 lb./in.² in the unnotched specimens. In rolled plates the true stress at tensile fracture in the rolling direction can be more than 1.5 times that in the transverse direction (26). Presumably the anisotropy developed during a tensile test will further reduce the transverse stress required for fracture. Thus, the fibrous fracture criterion may be

$$\sigma_r \epsilon_z^n = \text{constant} \quad [8]$$

where

σ_r is the radial stress at the point of macrofracture initiation,

ϵ_z is the axial strain at the point of macrofracture initiation.

The data obtained in this investigation agree with Equation 8 when n equals 0.4, and the constant is 19,000 lb./in.². However, since fibrous fracture occurred at only two different strains, these data are insufficient to prove the validity of Equation 8. Alpaugh (27) tested specimens made from similar steel and with the same notch flank

angle that was employed in this investigation. He found that as a/R is increased from 1.5 to 4 the average strain at fracture decreases, but the average stress at fracture continues to increase. This result is incompatible with the fracture criterion that is based on a critical maximum tensile stress, but it is qualitatively compatible with the fracture criterion stated in Equation 8. Since the stress and strain distributions in the specimens with sharper notches, a/R greater than 1.5, are unknown, the validity of Equation 8 at strains smaller than 0.3 cannot now be determined. The author is of the opinion that the fibrous macrofractures which occurred in this investigation were initiated by axial cracks, and the proper fibrous fracture criterion is one that involves the radial stress, such as Equation 8.

IV. CONCLUSIONS

This investigation has led to the conclusions presented below, which pertain to the particular mild steel that was used in this study.

A. Maximum Tensile Stress and Strain at Fracture

While it was one of the purposes of this investigation to determine the local maximum tensile stress and strain at which fracture is initiated, a single determination applicable to the full range of conditions is not possible. However, this study has led to some specific new conclusions which are significant to an understanding of fracture conditions. These conclusions are stated below:

(1) The stress distribution that was calculated by Bridgman is not valid in notched tensile specimens, because the radial displacement is not a linear function of the radius as is assumed in Bridgman's calculation. In notched specimens, the strain is a maximum near the notch root and a minimum on the axis. In a specimen with an initial radius ratio, a/R , of 1.5, the axial stress is nearly constant independent of radius.

(2) General yielding decreases the maximum tensile stress at cleavage fracture from 210,000 lb./in.² to 100,000 lb./in.².

(3) When the maximum tensile stress that is necessary for cleavage fracture is plotted against the corresponding maximum tensile strain, the result is a unique locus. Cleavage fracture will occur, provided the specimen is flowing plastically, when the maximum tensile stress-strain in the specimen reaches a value that is represented by a point on the locus, regardless of the stress-strain path that was followed. The range of maximum tensile stress values on

the locus is 100,000 - 140,000 lb. /in. ².

(4) Ludwik's hypothesis is not valid for fibrous fractures. Specimens with a given geometry fibrously fracture at a given strain regardless of the stress. The range of maximum tensile stress values for fibrous fracture is 110,000 - 150,000 lb. /in. ².

(5) Notched tensile specimens fibrously fracture at smaller strains than unnotched tensile specimens. The greater radial tensile stress in notched specimens causes the strain at which axial macrocracks can be initiated to be smaller in notched specimens than in unnotched specimens. This suggests that the fibrous fracture criterion has the form

$$\sigma_r \epsilon_z^n = \text{constant.}$$

B. Mechanism of Fibrous Tensile Fracture

Another purpose of this investigation was to study the mechanism of fibrous tensile fracture. The experimental observations have led to a new description of the mechanism of fibrous tensile fracture in mild steel. The pertinent conclusions are presented below:

(1) In mild steel, fibrous fractures do not develop by the gradual growth and coalescence of voids that are large enough to be visible in the optical microscope. Many fine microcracks which are associated with pearlite colonies and inclusions develop in the tensile specimen prior to the initiation of the macrofracture. The microcracks are found to occur at a strain as small as 15 per cent of the final fracture strain. During the ensuing straining, the number of microcracks increases greatly. However, prior to the initiation of the macrofracture, none of the microcracks have opened up or spread

beyond the microstructural feature with which they are associated. The critical event in the initiation of the macrofracture is the spreading of a microcrack beyond the microstructural feature with which it is associated.

(2) Voids are not observed prior to the initiation of the macrofracture. All of the voids which form are created during the development of the macrofracture. All of the voids are interconnected. Voids that are isolated from the macrofracture are not observed. Additional studies will be necessary to determine if this mechanism is valid for the fracture of notched specimens.

(3) Axial cracks are a prominent feature of fibrous macrofractures in a tensile specimen of banded steel. The axial macrocracks probably have an essential role in the initiation of the macrofracture. The long axial macrocracks are associated with inclusion stringers, but very short axial macrocracks lie in grain boundaries.

APPENDIX I

The Dependence of the Grain Boundary Angles upon Strain

At a grain boundary intersection the acute angle, θ , between a grain boundary and the specimen axis will decrease in magnitude as a point that is an infinitesimal distance from the intersection is strained from its initial position, P_0 , to position P , as is shown in Figure 56. From Figure 56:

$$\theta_0 = \tan^{-1} \frac{dr_0}{dz_0} \quad (I-1)$$

$$\theta = \tan^{-1} \frac{dr}{dz} \quad (I-2)$$

The strain components are:

$$\epsilon_r = \ln \frac{dr}{dr_0} \quad (I-3)$$

$$\epsilon_z = \ln \frac{dz}{dz_0} \quad (I-4)$$

Then

$$\theta_0 = \tan^{-1} [e^{(\epsilon_z - \epsilon_r)} \tan \theta] \quad (I-5)$$

Let

$$a = e^{\epsilon_r - \epsilon_z} \quad (I-6)$$

Then

$$\theta_0 = \tan^{-1} \left(\frac{1}{a} \tan \theta \right) \quad (I-7)$$

Assume that the probability density function for θ_0 is a constant:

$$f(\theta_0) = \frac{2}{\pi} \quad (I-8)$$

The probability distributions are

$$P(\theta_0) = \frac{2}{\pi} \theta_0 \quad (I-9)$$

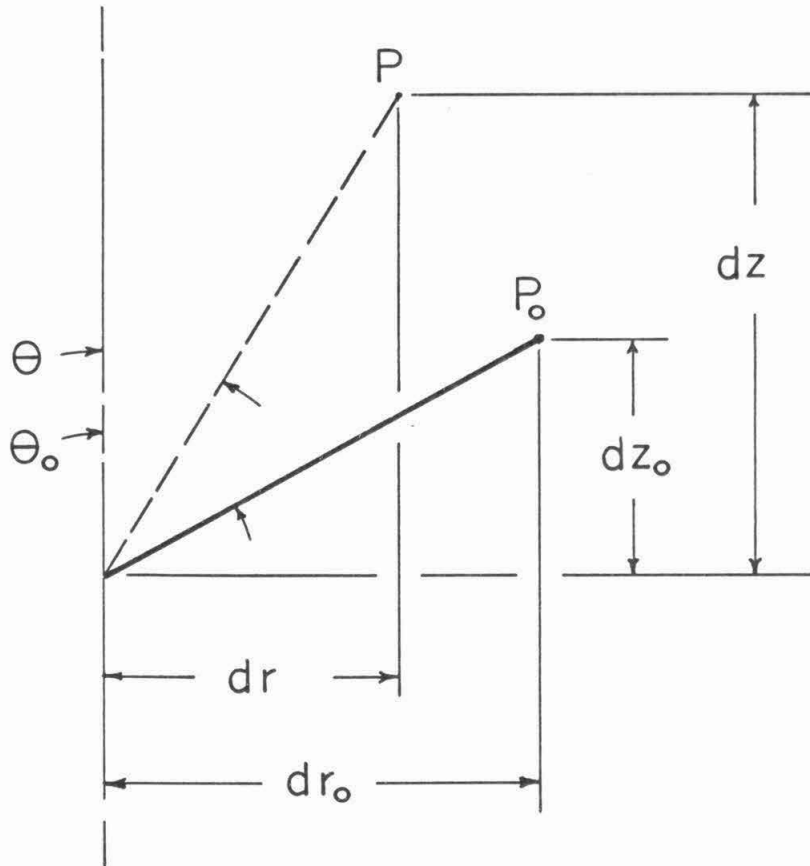


Figure 56. Grain Boundary Coordinates.

$$P(\theta) = \frac{2}{\pi} \tan^{-1} \left(\frac{1}{a} \tan \theta \right) \quad (\text{I-10})$$

Then the probability density function for θ is

$$f(\theta) = \frac{dP(\theta)}{d\theta} = \frac{2}{\pi} \frac{1}{a} \left(\frac{\sec^2 \theta}{1 + \frac{1}{a^2} \tan^2 \theta} \right) \quad (\text{I-11})$$

The mean value of θ is

$$\bar{\theta} = \int_0^{\pi/2} \theta f(\theta) d\theta = \frac{2}{\pi} \frac{1}{a} \int_0^{\pi/2} \frac{\theta \sec^2 \theta}{1 + \frac{1}{a^2} \tan^2 \theta} d\theta .$$

Let

$$x = \frac{1}{a} \tan \theta$$

$$dx = \frac{1}{a} \sec^2 \theta d\theta$$

Then

$$\bar{\theta} = \frac{2}{\pi} \int_0^{\infty} \frac{\tan^{-1} ax}{1+x^2} dx \quad (\text{I-12})$$

The author was unable to analytically integrate Equation I-12. If Equation I-12 were to be numerically integrated, the numerical integration would have to be repeated for several values of the parameter a . The analysis outlined below reduced the number of numerical integrations to one.

$$g(a) = \frac{\pi}{2} \frac{d\bar{\theta}}{da} = \int_0^{\infty} \frac{x dx}{(1+x^2)[1+(ax)^2]} \quad (\text{I-13})$$

The integral in Equation I-13 can be found in tables of integrals, and after inserting the limits the result is

$$\frac{\pi}{2} \frac{d\bar{\theta}}{da} = \frac{1}{(a^2-1)} \ln a \quad (\text{I-14})$$

Thus,

$$\bar{\theta} = \frac{\pi}{4} + \frac{2}{\pi} \int_1^a \frac{\ln y}{y^2-1} dy \quad (\text{I-15})$$

Equation I-15 was numerically integrated to give

$$\bar{\theta} = \bar{\theta}(a) \quad (\text{I-16})$$

If the strain is uniform,

$$\epsilon_z = -2\epsilon_r = \epsilon$$

Equation I-6 gives

$$a = e^{-3/2\epsilon} \quad (\text{I-17})$$

Combining Equations I-16 and I-17 gives

$$\bar{\theta} = \bar{\theta}(\epsilon) \quad (\text{I-18})$$

Equation I-18 is plotted as the solid curve in Figure 17.

APPENDIX II

A round tensile specimen has both axial symmetry with respect to the specimen axis and reflection symmetry with respect to the plane of the minimum cross section. The symmetry imposes the conditions that are given below.

A. Axial Symmetry

1. $u_{\theta} = \tau_{r\theta} = \tau_{z\theta} = 0$
2. $u_r = 0$ at $r = 0$
3. $\partial u_z / \partial r_0 = 0$ at $r = 0$

B. Reflection Symmetry

1. u_z and τ_{rz} are odd functions of z ,
2. u_r , σ_r , σ_{θ} , and σ_z are even functions of z .

The symbols that are employed in this appendix are defined as follows:

- r_0 is the radial coordinate of an element of material in the undeformed state
- z_0 is the axial coordinate of an element of material in the undeformed state
- r is the radial coordinate of an element of material in the deformed state
- z is the axial coordinate of an element of material in the deformed state
- θ is the coordinate that is perpendicular to the r, z plane
- u_r is the radial displacement of an element of material

u_z is the axial displacement of an element of material

u_θ is the displacement in the θ direction

$\tau_{r\theta}$, $\tau_{z\theta}$, and τ_{rz} are the three shear stresses in cylindrical coordinates

σ_r , σ_θ , and σ_z are the three normal stresses in cylindrical coordinates

a_0 is the outside radius of the minimum cross section in the undeformed state

a is the outside radius of the minimum cross section in the deformed state

The assumption is made that the displacements can be expanded in Taylor's series about the origin.

$$u_r = \sum_{m=0}^{\infty} \sum_{n=0}^{\infty} b_{mn} r_0^m z_0^n \quad (\text{II-1})$$

$$u_z = \sum_{m=0}^{\infty} \sum_{n=0}^{\infty} c_{mn} r_0^m z_0^n \quad (\text{II-2})$$

The coefficients b_{mn} and c_{mn} are functions of ξ , where

$$\xi = a/a_0 \quad (\text{II-3})$$

is a convenient parameter that represents the progress of straining.

The following restrictions are placed on the coefficients by the symmetry conditions:

$$\begin{aligned} b_{0n} &= 0 && (u_r = 0 \text{ at } r = 0) \\ c_{1n} &= 0 && (\partial u_z / \partial r_0 = 0 \text{ at } r = 0) \\ c_{mn} &= 0 && \text{for even } n \text{ (} u_z \text{ odd in } z) \end{aligned}$$

$$b_{mn} = 0 \quad \text{for odd } n \quad (u_r \text{ even in } z)$$

As a result of these restrictions, Equations II-1 and II-2 can be re-written:

$$u_r = \sum_{m=1}^{\infty} \sum_{n=0}^{\infty} b_{mn} r_o^m z_o^{2n} \quad (\text{II-4})$$

$$u_z = \sum_{n=1}^{\infty} c_{on} z_o^{2n-1} + \sum_{m=2}^{\infty} \sum_{n=1}^{\infty} c_{mn} r_o^m z_o^{2n-1} \quad (\text{II-5})$$

If the plastic strains are large compared to the elastic strains, the material can be assumed to be incompressible, which gives

$$d\epsilon_r + d\epsilon_{\theta} + d\epsilon_z = 0 \quad (\text{II-6})$$

The strain increments are defined as

$$d\epsilon_r = \frac{\partial(\frac{du_r}{d\xi})}{\partial r} d\xi \quad (\text{II-7})$$

$$d\epsilon_{\theta} = \frac{\frac{du_r}{d\xi}}{r} d\xi \quad (\text{II-8})$$

$$d\epsilon_z = \frac{\partial(\frac{du_z}{d\xi})}{\partial z} d\xi \quad (\text{II-9})$$

Combining Equations II-6, II-7, II-8, and II-9 gives

$$\frac{\partial(\frac{du_r}{d\xi})}{\partial r} + \frac{\frac{du_r}{d\xi}}{r} + \frac{\partial(\frac{du_z}{d\xi})}{\partial z} = 0 \quad (\text{II-10})$$

From Equations II-4 and II-5

$$\frac{du_r}{d\xi} = \sum_{m=1}^{\infty} \sum_{n=0}^{\infty} b'_{mn} r_o^m z_o^{2n} \quad (\text{II-11})$$

$$\frac{du_z}{d\xi} = \sum_{n=1}^{\infty} c'_{on} z_o^{2n-1} + \sum_{m=2}^{\infty} \sum_{n=1}^{\infty} c'_{mn} r_o^m z_o^{2n-1} \quad (\text{II-12})$$

where

$$b'_{mn} = \frac{db_{mn}}{d\xi} ,$$

$$c'_{mn} = \frac{dc_{mn}}{d\xi} .$$

Equation II-10 can be rewritten as

$$\frac{\partial(\frac{du_r}{d\xi})}{\partial r_o} \frac{\partial r_o}{\partial r} + \frac{\partial(\frac{du_r}{d\xi})}{\partial z_o} \frac{\partial z_o}{\partial r} + \frac{1}{r} \frac{du_r}{d\xi} + \frac{\partial(\frac{du_z}{d\xi})}{\partial r_o} \frac{\partial r_o}{\partial z} + \frac{\partial(\frac{du_z}{d\xi})}{\partial z_o} \frac{\partial z_o}{\partial z} = 0 \quad (\text{II-13})$$

A standard transformation of calculus gives

$$\frac{\partial r_o}{\partial r} = \frac{1}{j} \frac{\partial z}{\partial z_o} \quad (\text{II-14})$$

$$\frac{\partial r_o}{\partial z} = -\frac{1}{j} \frac{\partial r}{\partial z_o} \quad (\text{II-15})$$

$$\frac{\partial z_o}{\partial r} = -\frac{1}{j} \frac{\partial z}{\partial r_o} \quad (\text{II-16})$$

$$\frac{\partial z_o}{\partial z} = \frac{1}{j} \frac{\partial r}{\partial r_o} \quad (\text{II-17})$$

where

$$j = \frac{\partial r}{\partial r_o} \frac{\partial z}{\partial z_o} - \frac{\partial r}{\partial z_o} \frac{\partial z}{\partial r_o} \quad (\text{II-18})$$

Substituting Equations II-14 through II-18 into Equation II-13 gives

$$r \frac{\partial(\frac{du_r}{d\xi})}{\partial r_o} \frac{\partial z}{\partial z_o} - r \frac{\partial(\frac{du_r}{d\xi})}{\partial z_o} \frac{\partial z}{\partial r_o} + j \frac{du_r}{d\xi} - r \frac{\partial(\frac{du_z}{d\xi})}{\partial r_o} \frac{\partial r}{\partial z_o} + r \frac{\partial(\frac{du_z}{d\xi})}{\partial z_o} \frac{\partial r}{\partial r_o} = 0 \quad (\text{II-19})$$

By definition,

$$r = r_o + u_r \quad (\text{II-20})$$

$$z = z_o + u_z \quad (\text{II-21})$$

Substituting Equations II-4 and II-5 into Equations II-20 and II-21 gives

$$r = r_o + \sum_{m=1}^{\infty} \sum_{n=0}^{\infty} b_{mn} r_o^m z_o^{2n} \quad (\text{II-22})$$

$$z = z_o + \sum_{n=1}^{\infty} c_{on} z_o^{2n-1} + \sum_{m=2}^{\infty} \sum_{n=1}^{\infty} c_{mn} r_o^m z_o^{2n-1} \quad (\text{II-23})$$

Performing the proper partial differentiation on Equations II-11, II-12, II-22, and II-23, and substituting the results into Equation II-19 gives Equation II-24, which is on page 121.

Collecting the terms in r_o in Equation II-24 gives

$$2b'_{10} (1+c_{01})(1+b_{10}) + (1+b_{10})^2 c'_{01} = 0 \quad (\text{II-25})$$

The solution is

$$(1+b_{10})^2 = \frac{1}{1+c_{01}} \quad (\text{II-26})$$

Collecting terms in r_o^2 in Equation II-24, and substituting from Equation II-25 gives

$$\frac{b'_{20}}{b_{20}} = \frac{b'_{10}}{1+b_{10}} \quad (\text{II-27})$$

Initially, both b_{20} and b_{10} are zero. The solution to Equation II-27 with these initial conditions is

$$b_{20} = 0 \quad (\text{II-28})$$

This is the restriction that is stated in Part III. Collecting terms in r_o^3 in Equation II-24 gives

$$\begin{aligned}
 & \left[\sum_{m=1}^{\infty} \sum_{n=0}^{\infty} mb'_{mn} r_o^{m-1} z_o^{2n} \right] \left[r_o + \sum_{m=1}^{\infty} \sum_{n=0}^{\infty} b_{mn} r_o^m z_o^{2n} \right] \\
 & \left[1 + \sum_{n=1}^{\infty} (2n-1)c_{on} z_o^{2n-2} + \sum_{m=2}^{\infty} \sum_{n=1}^{\infty} (2n-1)c_{mn} r_o^m z_o^{2n-2} \right] \\
 - & \left[\sum_{m=1}^{\infty} \sum_{n=1}^{\infty} 2nb'_{mn} r_o^m z_o^{2n-1} \right] \left[\sum_{m=2}^{\infty} \sum_{n=1}^{\infty} mc_{mn} r_o^{m-1} z_o^{2n-1} \right] \\
 & \left[r_o + \sum_{m=1}^{\infty} \sum_{n=0}^{\infty} b_{mn} r_o^m z_o^{2n} \right] \\
 + & \left[\sum_{m=1}^{\infty} \sum_{n=0}^{\infty} b'_{mn} r_o^m z_o^{2n} \right] \left[1 + \sum_{m=1}^{\infty} \sum_{n=0}^{\infty} mb_{mn} r_o^{m-1} z_o^{2n} \right] \\
 & \left[1 + \sum_{n=1}^{\infty} (2n-1)c_{on} z_o^{2n-2} + \sum_{m=2}^{\infty} \sum_{n=1}^{\infty} (2n-1)c_{mn} r_o^m z_o^{2n-2} \right] \\
 - & \left[\sum_{m=1}^{\infty} \sum_{n=0}^{\infty} b'_{mn} r_o^m z_o^{2n} \right] \left[\sum_{m=1}^{\infty} \sum_{n=1}^{\infty} 2nb_{mn} r_o^m z_o^{2n-1} \right] \\
 & \left[\sum_{m=2}^{\infty} \sum_{n=1}^{\infty} mc_{mn} r_o^{m-1} z_o^{2n-1} \right] \\
 - & \left[\sum_{m=2}^{\infty} \sum_{n=1}^{\infty} mc'_{mn} r_o^{m-1} z_o^{2n-1} \right] \left[\sum_{m=1}^{\infty} \sum_{n=1}^{\infty} 2nb_{mn} r_o^m z_o^{2n-1} \right] \\
 & \left[r_o + \sum_{m=1}^{\infty} \sum_{n=0}^{\infty} b_{mn} r_o^m z_o^{2n} \right] \\
 + & \left[\sum_{n=1}^{\infty} (2n-1)c'_{on} z_o^{2n-2} + \sum_{m=2}^{\infty} \sum_{n=1}^{\infty} (2n-1)c'_{mn} r_o^m z_o^{2n-2} \right] \\
 & \left[1 + \sum_{m=1}^{\infty} \sum_{n=0}^{\infty} mb_{mn} r_o^{m-1} z_o^{2n} \right] \left[r_o + \sum_{m=1}^{\infty} \sum_{n=0}^{\infty} b_{mn} r_o^m z_o^{2n} \right] = 0 \quad (\text{II-24})
 \end{aligned}$$

$$4b'_{30}(1+c'_{01}) + 2b'_{30}c'_{01} + 2b'_{10}c'_{21} + (1+b'_{10})c'_{21} = 0 . \quad (\text{II-29})$$

Equation II-29 does not in general require b'_{30} to be zero.

APPENDIX III

Stress Distribution in a Notched Specimen

This appendix contains an analysis of the stress distribution on the minimum cross section of a notched specimen. This analysis follows after Bridgman (13), but the radial displacement is assumed to be nonlinear instead of linear.

On the minimum cross section at a particular instant the stresses, strains, and displacements depend only upon the radius. The radial displacement is assumed to be given by a function of the form

$$u_r = (\xi - 1) a_o f(\rho) \quad (\text{III-1})$$

where

$$\xi = a/a_o$$

$$\rho = r_o/a_o$$

a_o is the outside radius of the minimum cross section in the undeformed state

a is the outside radius of the minimum cross section in the deformed state

r_o is the distance, in the undeformed state, from an element of material on the minimum cross section to the specimen axis

The radial strain increment is

$$\begin{aligned} d\epsilon_r &= \frac{\partial}{\partial r} [f(\rho)] a_o d\xi \\ d\epsilon_r &= f'(\rho) \frac{\partial r_o}{\partial r} d\xi \end{aligned} \quad (\text{III-2})$$

where r is the distance, in the deformed state, from an element of

material on the minimum cross section to the specimen axis.

$$r = r_o + u_r = r_o + (\xi - 1) a_o f(\rho)$$

$$\frac{\partial r}{\partial r_o} = 1 + (\xi - 1) f'(\rho) \quad (\text{III-3})$$

Since z is a constant on the minimum cross section,

$$\frac{\partial r_o}{\partial r} = \frac{1}{\partial r / \partial r_o} \quad (\text{III-4})$$

Combining Equations III-2, III-3, and III-4 gives

$$d\epsilon_r = \frac{f'(\rho)}{1 + (\xi - 1) f'(\rho)} d\xi \quad (\text{III-5})$$

The circumferential strain increment is

$$d\epsilon_\theta = du_r / r$$

$$d\epsilon_\theta = \frac{a_o f(\rho)}{r_o + (\xi - 1) a_o f(\rho)} d\xi$$

$$d\epsilon_\theta = \frac{f(\rho)}{\rho + (\xi - 1) f(\rho)} d\xi \quad (\text{III-6})$$

Due to incompressibility,

$$d\epsilon_z = - (d\epsilon_r + d\epsilon_\theta) \quad (\text{III-7})$$

From the Levy-Mises plastic flow law, the generalized strain increment is

$$d\bar{\epsilon} = \sqrt{\frac{2}{3}} \sqrt{(d\epsilon_r)^2 + (d\epsilon_\theta)^2 + (d\epsilon_z)^2} \quad (\text{III-8})$$

Substituting Equations III-5, III-6, and III-7 into III-8 gives

$$\frac{d\bar{\epsilon}}{d\xi} = \frac{2}{\sqrt{3}} \sqrt{\left[\frac{f'(\rho)}{1 + (\xi - 1) f'(\rho)} \right]^2 + \left[\frac{f(\rho)}{\rho + (\xi - 1) f(\rho)} \right]^2 + \left[\frac{f'(\rho)}{1 + (\xi - 1) f'(\rho)} \right] \left[\frac{f(\rho)}{\rho + (\xi - 1) f(\rho)} \right]} \quad (\text{III-9})$$

One would like to integrate Equation III-9 to obtain $\bar{\epsilon}$ as a function of ξ and ρ , but unless $f(\rho)$ is linear the integration appears to be impossible. However, an approximation can be made that will allow $\bar{\epsilon}$ to be determined as a function of ξ and ρ . Let

$$K = d\epsilon_{\theta}/d\epsilon_r \quad (III-10)$$

Then

$$d\epsilon_z = -(1+K)d\epsilon_r \quad (III-11)$$

$$d\bar{\epsilon} = \sqrt{\frac{2}{3}} \sqrt{\left(\frac{d\epsilon_z}{1+K}\right)^2 + \left(\frac{Kd\epsilon_z}{1+K}\right)^2 + d\epsilon_z^2}$$

$$\frac{d\bar{\epsilon}}{d\epsilon_z} = \frac{2}{\sqrt{3}} \left(\frac{1}{1+K}\right) \sqrt{1 + K + K^2} \quad (III-12)$$

The values of the right side of Equation III-12 are tabulated in Table IV. For values of K between 0.4 and one, $d\bar{\epsilon}$ differs from $d\epsilon_z$ by less than three per cent. In the problem under consideration, K is always between 0.4 and one. Therefore, the assumption is made that

$$d\bar{\epsilon} = d\epsilon_z \quad (III-13)$$

Combining Equations III-5, III-6, and III-7 gives

$$d\bar{\epsilon} = d\epsilon_z = - \left[\frac{f'(\rho)}{1+(\xi-1)f'(\rho)} + \frac{f(\rho)}{\rho+(\xi-1)f(\rho)} \right] d\xi \quad (III-14)$$

Integrating gives

$$\bar{\epsilon} = \epsilon_z = - \ln \{ [1+(\xi-1)f'(\rho)] [1 + \frac{1}{\rho} (\xi-1)f(\rho)] \} \quad (III-15)$$

Equation III-15 gives the generalized strain on the minimum cross section as a function of radial position and ξ , which is a measure of the average strain. The generalized flow stress can be obtained from the uniaxial flow function

TABLE IV

Ratio of Generalized Strain Increment to
Increment of Maximum Principal Strain

$K = \frac{d\epsilon_{\theta}}{d\epsilon_r}$	$\frac{d\bar{\epsilon}}{d\epsilon_z} = \frac{2}{\sqrt{3}} \left(\frac{1}{1+K} \right) \sqrt{1+K+K^2}$
1	1
0.9	1.000
0.8	1.000
0.7	1.000
0.6	1.010
0.5	1.020
0.4	1.029
0.3	1.052
0.2	1.071
0.1	1.109
0	1.154

$$\bar{\sigma} = g(\bar{\epsilon}) \quad \text{(III-16)}$$

which in this analysis is taken to be the function represented by the flow curve in Figure 11. From the Lévy-Mises flow law,

$$\sigma'_r = \frac{2}{3} \frac{d\epsilon_r}{d\bar{\epsilon}} g(\bar{\epsilon}) \quad \text{(III-17)}$$

$$\sigma'_\theta = \frac{2}{3} \frac{d\epsilon_\theta}{d\bar{\epsilon}} g(\bar{\epsilon}) \quad \text{(III-18)}$$

$$\sigma'_z = \frac{2}{3} \frac{d\epsilon_z}{d\bar{\epsilon}} g(\bar{\epsilon}) \quad \text{(III-19)}$$

where the primes indicate deviatoric stresses. Substituting Equations III-10 and III-11 into III-17, III-18, and III-19 gives

$$\sigma'_r = \frac{2}{3} \left(\frac{-1}{1+K} \right) g(\bar{\epsilon}) \quad (\text{III-20})$$

$$\sigma'_\theta = \frac{2}{3} \left(\frac{-K}{1+K} \right) g(\bar{\epsilon}) \quad (\text{III-21})$$

$$\sigma'_z = \frac{2}{3} g(\bar{\epsilon}) \quad (\text{III-22})$$

Substituting Equations III-5 and III-6 into III-10 gives

$$K = \frac{f(\rho)[1+(\xi-1)f'(\rho)]}{f'(\rho)[\rho+(\xi-1)f(\rho)]} . \quad (\text{III-23})$$

From Equation 4,

$$f(\rho) = 0.6\rho + 0.4\rho^3 . \quad (\text{III-24})$$

Equations III-15, III-20, III-21, III-22, III-23, and III-24 plus the flow curve of Figure 11 were used to compute the deviatoric stresses on the minimum cross section. These calculations were made for combinations of

$$\xi = 0.98, 0.92, 0.86, \text{ and } 0.76 ;$$

$$\rho = 0, 0.2, 0.4, 0.6, 0.8, \text{ and } 1.0 .$$

The only quantity needed in addition to the deviatoric stresses is the hydrostatic tension

$$P = P(r) .$$

Bridgman's approximate method was used to find P . Equation 1-8 from Bridgman's book (13) is

$$\sigma'_z \frac{r^2}{a} = \sigma'_r \left(\frac{3}{2} \frac{r^2}{a} - \frac{a}{2} - R \right) - r \frac{d\sigma}{dr} \left(R + \frac{a^2 - r^2}{2a} \right) + \sigma'_\theta \left(R + \frac{a^2 - r^2}{2a} \right)$$

where R is the profile radius. Rewriting and simplifying gives

$$\frac{dP}{d(r/a)} = \frac{\sigma'_\theta - \sigma'_r}{r/a} - \frac{d\sigma'_r}{d(r/a)} + \frac{2(r/a)}{2(R/a)+1-(r/a)^2} (\sigma'_r - \sigma'_z) . \quad (\text{III-25})$$

For a given average strain (given ξ), the right side of Equation III-25 is a completely known function of r/a . The boundary condition is

$$\sigma_r = 0 \quad \text{at} \quad r/a = 1 .$$

Equation III-25 was numerically integrated to obtain the values of the hydrostatic tension. These values were added to the deviatoric stress to obtain the total radial, circumferential, and axial stresses as a function of radius.

Since the above numerical calculation is based on the flow stress-strain curve that was obtained at room temperature, the resulting stress distribution is valid only at room temperature. However, if the effect of temperature upon the flow stress is independent of strain, the stress distribution at a low temperature can be obtained by multiplying the room temperature stresses by a constant. The effect of temperature on the flow stress was independent of strain except at small strains, as shown in Figure 13. The assumption was made that the low temperature stresses were equal to the room temperature stresses multiplied by a constant, regardless of the strain.

REFERENCES

1. Shank, M. E., "Brittle Failure of Steel Structures," Metal Progress, Vol. 66, 1954, No. 3, p. 83; No. 4, p. 120; Vol. 67, 1955, No. 6, p. 111.
2. Averbach, B. L., et al. (ed.) Fracture. Cambridge, Mass.: Technology Press of Massachusetts Institute of Technology, 1959.
3. Crack Propagation Symposium, Proceedings. Cranfield, England: The College of Aeronautics, 1962.
4. Drucker, D. C., and Gilman, J. J. (ed.) Fracture of Solids. New York: Interscience Publishers, 1963.
5. Kawasaki, T., Swedlow, J. L., and Yokobori, T. (ed.) Proceedings of the International Conference on Fracture. (Conference in Sendai, Japan, September, 1965), to be printed.
6. Biggs, W. D., The Brittle Fracture of Steel. New York: Pitman, 1960.
7. Yokobori, T., The Strength, Fracture, and Fatigue of Materials. Groningen, The Netherlands: P. Noordhoff, 1965.
8. Parker, E. R., Davis, H. E., and Flanigan, A. E., "A Study of the Tension Test," American Society for Testing Materials, Proceedings, Vol. 46, 1946, pp. 1159-1174.
9. Ludwik, P., "Die Bedeutung des Gleit- und Reisswiderstandes für die Werkstoffprüfung," Zeitschrift VDI, Vol. 71, 1927, p. 1532.
10. Lubahn, J. D., "Notch Tensile Testing," Fracturing of Metals, (ed.) Jonassen, F., Roop, W. P., and Bayless, R. T. (Cleveland: American Society for Metals, 1948), pp. 90-132.
11. Siebel, E., Berichte der Fachausschüsse des Vereins deutscher Eisenhüttenleute. Werkstoffausschuss, Ber. 71, 1925.
12. Davidenkov, N. N., and Spiridonova, N. I., "Analysis of the State of Stress in the Neck of a Tension Test Specimen," American Society for Testing Materials, Proceedings, Vol. 46, 1946, pp. 1147-1158.
13. Bridgman, P. W., Studies in Large Plastic Flow and Fracture. Cambridge, Mass.: Harvard University Press, 1964.

14. Trozera, T. A., "On the Use of the Bridgman Technique for Correcting Stresses Beyond Necking," Transactions of the American Society for Metals, Vol. 56, 1963, pp. 780-782.
15. Marshall, E. R., and Shaw, M. C., "The Determination of Flow Stress from a Tensile Specimen," Transactions of the American Society for Metals, Vol. 44, 1952, pp. 705-725.
16. Low, J. R., Jr., "The Fracture of Metals," Progress in Materials Science, Vol. 12, 1963, No. 1.
17. Rogers, H. C., "The Tensile Fracture of Ductile Metals," Transactions AIME, Vol. 218, 1960, pp. 498-506.
18. Puttick, K. E., "Ductile Fracture in Metals," Philosophical Magazine, Series 8, Vol. 4, 1959, pp. 964-969.
19. Hahn, G. T., et al., "The Yield and Fracture Behaviour of Mild Steel, With Special Reference to Manganese," Journal of the Iron and Steel Institute, Vol. 200, 1962, pp. 634-644.
20. Phillips, A., Kerlins, V., and Whiteson, B. V., Electron Fractography Handbook. Technical Report ML-TDR-64-416, Air Force Materials Lab., Research and Technology Div., Air Force Systems Command, Wright-Patterson Air Force Base, Ohio, 1965.
21. Hendrickson, J. A., Wood, D. S., and Clark, D. S., "The Initiation of Brittle Fracture in Mild Steel," Transactions of the American Society for Metals, Vol. 50, 1958, pp. 656-681.
22. Wood, D. S., and Clark, D. S., "The Influence of Temperature Upon the Time Delay for Yielding in Annealed Mild Steel," Transactions of the American Society for Metals, Vol. 43, 1951, pp. 571-586.
23. Krause, D. J., An Influence of Grain Size on the Initiation of Brittle Fracture in Mild Steel. Eighth Interim Technical Report under U. S. Army Research Office (Durham), Project No. 1235, Contract No. DA-04-495-ORD-1631, California Institute of Technology, Pasadena, California, December 1961.
24. Gensamer, M., et al., "The Tensile Properties of Pearlite, Bainite, and Spheroidite," Transactions of the American Society for Metals, Vol. 30, 1942, pp. 983-1020.

25. Hahn, G. T., "Dislocation Etch-Pitting of Iron and Mild Steel," Transactions AIME, Vol. 224, 1962, pp. 395-397.
26. Backofen, W. A., "Metallurgical Aspects of Ductile Fracture," Fracture of Engineering Materials (Metals Park, Ohio: American Society for Metals, 1964), pp. 107-126.
27. Alpaugh, H. E., Jr., "Investigation of the Mechanisms of Failure in the Ductile Fracture of Mild Steel," Unpublished Bachelor's Thesis, Department of Mechanical Engineering, Massachusetts Institute of Technology, 1965.